

Microwave Engineering in Superconducting Nanowires for Single-Photon Detection

by

Di Zhu

Submitted to the Department of Electrical Engineering and Computer
Science

in partial fulfillment of the requirements for the degree of

Doctor of Philosophy in Electrical Engineering

at the

MASSACHUSETTS INSTITUTE OF TECHNOLOGY

September 2019

© Massachusetts Institute of Technology 2019. All rights reserved.

Author
Department of Electrical Engineering and Computer Science
August 30, 2019

Certified by.....
Karl K. Berggren
Professor of Electrical Engineering
Thesis Supervisor

Accepted by.....
Leslie A. Kolodziejski
Professor of Electrical Engineering and Computer Science
Chair, Department Committee on Graduate Students

Microwave Engineering in Superconducting Nanowires for Single-Photon Detection

by

Di Zhu

Submitted to the Department of Electrical Engineering and Computer Science
on August 30, 2019, in partial fulfillment of the
requirements for the degree of
Doctor of Philosophy in Electrical Engineering

Abstract

Detecting light at the single-photon level plays a crucial role in photonic quantum information processing, deep-space optical communication, astronomical observation, and biological and chemical sensing. With their exceptional performance, superconducting nanowire single-photon detectors (SNSPDs) have emerged as the leading single-photon counting technology at infrared wavelengths. Conventionally, the superconducting nanowires are treated as lumped circuit elements, and their microwave properties were largely neglected. In this thesis, we engineer the nanowires into kinetic-inductive transmission lines and use them to devise new single-photon detector architectures. Through impedance engineering, we developed a superconducting tapered nanowire detector that has increased output voltage, reduced timing jitter, and most importantly, the ability to resolve photon numbers. Utilizing the slow propagation speed of electrical signals in the nanowire transmission lines, we developed a delay-line-multiplexed detector array. This two-terminal array can perform coincidence counting over a large number of spatial modes and can be scalably integrated on photonic waveguides.

Thesis Supervisor: Karl K. Berggren
Title: Professor of Electrical Engineering

To Luying and Nora.

Acknowledgments

This thesis and other works during my graduate school would not have been possible without the help of my professors, colleagues, friends, and families. In particular, I would like to thank:

My advisor, Professor Karl K. Berggren, for his guidance and support in the past five years. His philosophies about science and education will continue to influence me in my future career.

Professors Dirk Englund, Kevin O'Brien, and Marko Lončar for kindly agreeing to be on my thesis committee and for providing opportunities for collaboration. It was an honor to work with them.

Qing-Yuan Zhao, for teaching me measurement and fabrication skills. He pioneered the superconducting nanowire single-photon imager, which is the foundation of my thesis work.

Marco Colangelo, for his great help in my final years. His passion, energy, and gifts impressed and motivated me. Many devices reported in this thesis were fabricated by him.

Andrew Dane, for developing the NbN deposition processes used in this thesis and many other works. He is the unsung hero.

Adam McCaughan, for developing phidl and contributing to the infrastructures in the group. He has made my and many others' lives easier.

Faraz Najafi, Francesco Bellei, Emily Toomey, Brenden Butters, Ashley Qu, Niccolò Calandri, Ignacio Estay Forno, Eugenio Maggiolini, Reza Baghdadi, Ilya Charaev, and Owen Medeiros for their help, discussion, and collaboration on superconducting nanowire devices.

Akshay Agarwal, Navid Abedzadeh, Chung-Soo Kim, Marco Turchetti, Richard Hobbs, Mengjie Zheng, John William Simonaitis, Yujia Yang, and Donnie Keathley for help, discussion, and collaboration on nanofabrication, electron microscopy, and nano-photonics.

All past and present members in the Quantum Nanostructures and Nanofabrica-

tion group. They have made the group a pleasant and lovely place to stay.

Jim Daley and Mark Mondol for help in fabrications and anything related to NSL.

Professor Daniel Santavicca and Dr. Joshua Bienfang for their advice and collaboration on nanowire-based microwave devices.

Boris Korzh, Matthew Shaw, Simone Frasca, Sae-Woo Nam, Richard Mirin, and all collaborators from JPL and NIST for collaborations on differential readout, tapered detectors, and low-jitter detectors.

Changchen Chen and Dr. Franco N. C. Wong for sharing photon sources and collaboration on the photon-number-resolving detector.

Hyeonrak Choi (Chuck), Tsung-Ju Jeff Lu, and Eric Bersin from the Englund group for collaborations on aluminum nitride, quantum walk, and single-photon sources.

Yi Yang, Professor Chao Peng, and Professor Marin Soljačić for collaborations on nonlocal plasmonics and gauge fields.

Nanxi Li, Jin Xue, and Yi Yang for their help in my study, research, and life.

Xia Yu, Joel Yang, Perry Shum, Yanyan Zhou, Houkun Liang, and Zhaogang Dong for their mentoring. They are the ones who led me to this research career.

My parents, for their love and support. They made who I am.

My wife, Luying, for her sacrifice, love, and support. And her parents and family for their trust and help.

My daughter, Nora, for bringing me joy and peace. She reminds me that even if I fail my research and career, I will not fail my life because I am a father.

My PhD fellowship from A*STAR, Singapore, and research funding support from AFOSR, DARPA, NSF, and NASA.

Contents

1	Introduction	21
1.1	Superconducting nanowire single-photon detector (SNSPD)	22
1.2	Microwave dynamics in superconducting nanowires	24
1.3	This thesis	25
2	Kinetic-inductive superconducting nanowire transmission lines	27
2.1	Kinetic inductance in superconducting thin films	27
2.2	Superconducting microwave waveguides	32
2.3	Superconducting coplanar waveguides (SCPW)	35
2.4	Superconducting nanowire microstrip and “tunnel” transmission lines	45
2.5	Coupled nanowire transmission lines	47
2.6	Impedance-matching taper	55
2.7	Conclusion	59
3	SNSPD with integrated impedance-matching taper	61
3.1	Introduction	61
3.2	Concept of tapered readout	63
3.3	Design and fabrication	65
3.4	Device measurement	66
3.5	Increasing output voltage	67
3.6	Increasing slew rate and reducing timing jitter	70
3.7	Microwave characterization of impedance-matching taper	72
3.8	Conclusions	75

4	Resolving photon numbers in tapered SNSPD	77
4.1	Introduction	78
4.2	Architecture and operating principle	79
4.3	SPICE simulation	80
4.4	Device design and fabrication	81
4.5	Measurement setup	82
4.6	Photon number resolution	85
4.6.1	Pulse shapes and timing jitter	85
4.6.2	Pulse height distribution	85
4.6.3	Rise time and rising-edge slope	86
4.6.4	Photon statistics	88
4.6.5	Effects of photon inter-arrival time	91
4.7	Direct observation of photon bunching in Hong-Ou-Mandel interference	92
4.8	Other basic detector metrics	95
4.8.1	Efficiency and dark count rate	96
4.8.2	Reset time	96
4.8.3	Reducing taper size with grounded CPW design	97
4.9	Derivation of photon counting statistics	99
4.9.1	Counting statistics and estimation of effective mean photon per pulse	99
4.9.2	STaND array vs. SNSPD array	101
4.10	Conclusion	102
5	A scalable coincidence detector based on superconducting nanowire transmission line	103
5.1	Introduction	104
5.2	Architecture and operating principle	105
5.3	Detector fabrication	107
5.4	Measurement setup	109
5.5	Demonstration of a 16-element detector	111

5.5.1	Multi-photon timing distribution	111
5.5.2	Single-photon difference and sum time distribution	112
5.5.3	Detector efficiency and dark count rate	113
5.5.4	Maximum counting rate	114
5.6	Timing and photon statistics analysis in a 4-element detector	114
5.6.1	Pulse shapes of single-photon events	115
5.6.2	Photon counting statistics	117
5.6.3	Timing resolutions	117
5.6.4	Derivation for photon counting statistics	119
5.7	Beyond two-photon detection	120
5.7.1	Fingerprints	120
5.7.2	Full list of pulse shapes and identified fingerprints	121
5.7.3	Reconstructing photon statistics from pulse shape analysis	122
5.8	Discussions on optical coupling and scalability	123
5.9	Conclusions	127
6	Progress on waveguide-integrated 65-channel detector array	129
6.1	Introduction	129
6.2	Device architecture	130
6.2.1	Device overview	130
6.2.2	Simulation of continuous-time quantum walk	133
6.3	Fabrication	134
6.4	Preliminary measurement results	140
6.5	Conclusion	143
7	Summary and outlook	145

List of Figures

2-1	Examining superconducting waveguides.	32
2-2	Thin-film superconducting coplanar waveguide	36
2-3	Line capacitance of a CPW in Fig. 2-2 with different gap sizes.. . . .	38
2-4	Characteristic impedance and phase velocity of normal metal CPW.	39
2-5	Current distribution along the width of the center conductor.	41
2-6	s-factor vs. center conductor width at different sheet inductance	42
2-7	Current distribution in the semi-infinite SCPW ground plane.	43
2-8	Inductance contributions in SCPW	44
2-9	Z_0 and v_{ph} of SCPW as a function of center conductor width.	45
2-10	Characteristic impedance and phase velocity of thin-film superconducting microstrip	46
2-11	“Tunnel” transmission line	47
2-12	Coupled nanowire transmission line.	48
2-13	Calculated S-parameters for nanowire coupler	54
2-14	Modulating nanowire coupler with DC bias current.	54
2-15	Klopfenstein taper profile.	57
2-16	Reflection from a 500 MHz Klopfenstein taper	58
2-17	Comparing 2N-degree polynomial taper and Klopfenstein taper with the same length.	59
3-1	Circuit diagram and micrographs of the tapered SNSPD readout.	64
3-2	Characteristic impedance (Z_0) and effective index (n_{eff}) of the superconducting NbN coplanar waveguide simulated using Sonnet.	66

3-3	SPICE simulated S-parameter of the impedance taper.	67
3-4	Measured detector pulses and comparison with SPICE simulation. . .	68
3-5	Power spectral density of the output pulses from tapered and reference detectors.	69
3-6	System gain characterization.	69
3-7	Simulated gain factor (the ratio between the maximum voltages of tapered and non-tapered detector) and taper inductance as a function of the starting input impedance (Z_H) under different nominal cut-off frequencies.	71
3-8	Measured noise floor from the tapered and non-tapered device.	72
3-9	Experimental observation on the reduction of timing jitter as a result of faster slew rate.	73
3-10	Normalized photon count rate (PCR, left axis) and dark count rate (DCR, right axis) as a function of bias current.	73
3-11	Instrument response function (IRF) under 1064 nm illumination. T .	74
3-12	S21 of two cascaded 116 MHz tapers used in Fig. 3-1.	75
3-13	S21 of cascaded 580 MHz taper at different temperatures.	75
4-1	Architecture and working mechanism for superconducting tapered nanowire detector (STaND).	80
4-2	Schematics of the SPICE simulation for multi-photon events in the STaND.	81
4-3	SPICE simulated pulse shapes, current distributions, and hotspot resistances in the STaND.	82
4-4	Micrographs of the STaND.	83
4-5	Measurement setup for characterizing the STaND with classical light source.	83
4-6	Optical alignment setup in the cryostat.	84
4-7	Pulse shape and timing jitter.	86
4-8	Histograms of the STaND's pulse heights under pulsed laser illumination.	87

4-9	Geometry and current density near the bends.	87
4-10	Comparing pulse height distributions under different illumination conditions.	88
4-11	Correlation among pulse height, rising slope (a), and rise time (b). . .	89
4-12	Counting statistics under coherent state illumination.	90
4-13	System electrical noise.	91
4-14	Estimating laser pulse width using the STaND.	92
4-15	Counting statistics when the modulated laser diode was driven to have a wider pulse width.	93
4-16	Measuring Hong-Ou-Mandel interference (HOM) interference using a single STaND.	94
4-17	Normalized Photon count rate (<i>PCR</i>) and dark count rate (<i>DCR</i>) as functions of bias current.	96
4-18	Estimating reset time from pulse decay.	98
4-19	Reducing taper inductance and footprint by using CPW with a top ground.	98
4-20	Estimation effective mean photon per pulse $\tilde{\mu}$	101
4-21	Comparison of resolving fidelity of large photon numbers using arrays of SNSPDs and STaNDs.	102
5-1	Device architecture and operating mechanism.	106
5-2	Fabrication process for the detector with microstrip delay lines. . . .	108
5-3	Micrographs of fabricated device.	110
5-4	Packaging of the detector chip for back illumination.	111
5-5	Measured timing distribution from the 16-element array that resolved all 136 distinguishable groups.	112
5-6	1-D histogram of the difference time ($t_{\text{diff}} = (t_1 - t_2)/2$) and sum time ($t_{\text{sum}} = (t_1 + t_2)/2 - t_0$) when the detector was operating in the single-photon regime.	113
5-7	Detector efficiency and dark count in the 16-element detector	114

5-8	Maximum count rate of the 16-element detector	115
5-9	Timing logic based two-photon detection in a 4-element detector chain.	116
5-10	Counting rate distribution in the 4-element detector	119
5-11	Traces of 100 pairs of detector pulses, corresponding to detection events where D_2 and D_4 fired, or D_2 , D_3 , and D_4 fired	121
5-12	Averaged pulse shapes for all detection cases.	122
5-13	Detector pulses for all single-photon cases	123
5-14	Detector pulses for unambiguous two-photon events	124
5-15	Detector pulses for ambiguous two-photon events	125
5-16	Detector pulses for ambiguous two, three, and four-photon events . .	125
5-17	Resolving up to four photons based on pulse shape processing.	126
5-18	Calculation of the optical absorption in the superconducting nanowire when integrated on waveguide	126
6-1	Notional schematics of the delay-line-multiplexed SNSPD array on SOI PIC.	131
6-2	Overview of the waveguide-integrated, delay-line-multiplexed SNSPD array.	132
6-3	Simulated coincidence probability over the 65 channels with 2 indistin- guishable input photons.	134
6-4	Fabrication flow.	135
6-5	Examples of inter-field stitching in EBL.	137
6-6	Proximity effect correction for the positive-tone waveguide pattern. .	138
6-7	Cross-sectional SEMs of etched Si waveguides.	139
6-8	Output pulses from the 65-element detector array (flood illumination).	140
6-9	t_{diff} histogram under different bias current.	141
6-10	Heights, widths, and peak positions of the 65 Gaussians in the t_{diff} histogram in Fig. 6-9 ($I_b = 16.5 \mu\text{A}$).. . . .	142
6-11	Normalized photon count rate (PCR) and dark count rate (DCR) of the 65-element array.	143

6-12 t_{diff} histogram for a 65-element array multiplexed through grounded-CPW without waveguide patterning. 144

List of Tables

2.1	Mode indices, impedances, and distributed circuit parameters of a symmetric nanowire microstrip coupler.	53
-----	------------------------------------------------------------------------------------------------------------------	----

Chapter 1

Introduction

Single-photon detectors allow humans to perceive light with unprecedented sensitivity. This ability has been harnessed for many applications, such as photonic quantum information processing, deep-space optical communication, astronomical observation, and biological and chemical sensing.

Superconducting nanowire single-photon detectors (SNSPDs) are currently the leading single-photon detection technology at infrared wavelengths [1, 2]. Their rapid advance in recent years has enabled impressive demonstrations both in technology development and testing of fundamental physics, such as record-distance quantum key distribution [3], Lunar Laser Communication Demonstration (LLCD) [4], and loophole-free test of local realism [5].

Though SNSPDs have been studied for almost two decades now [1], their microwave properties were largely neglected. Conventional device-level understanding of SNSPDs treats the nanowire as a lumped circuit element [6], with the justification that the physical size of the detector (100s of μm) is much smaller than the microwave wavelength of interest (cm-scale for GHz signals).

In this thesis, we explore the exotic microwave properties of superconducting nanowires to devise new detector architectures. We engineer the nanowires into kinetic-inductive microwave transmission lines. They have three prominent features: (1) high impedance ($\text{k}\Omega$ scale), (2) slow phase velocity (~ 2 orders of magnitude slower than the speed of light in free space), and (3) large nonlinearity. Using the high

impedance, we developed an impedance-matched readout for SNSPDs that amplifies the detector signal and enables photon number resolution. Using the slow phase/group velocity, we developed a scalable multiplexing scheme for SNSPD arrays.

1.1 Superconducting nanowire single-photon detector (SNSPD)

First invented by Gol'tsman et al. in 2001 [1], SNSPDs have now emerged as the leading single-photon detection technology at infrared wavelengths [2]. They have demonstrated $> 90\%$ detection efficiency [7], sub-3-ps timing jitter [8], sub-1-cps dark count rate [9], few-ns reset time [10], and spectral sensitivity from UV to mid-infrared [11, 12]. These exceptional detector metrics have enabled many unique applications, such as deep-space communication [4], quantum key distribution [13], fast photoluminescence detection [14, 15], and laser ranging [16]. Nowadays, commercial systems have become available and are used in many research laboratories.

A typical SNSPD consists of a thin (~ 5 nm thick) and narrow (< 100 nm wide) superconducting nanowire that is meandered into an area about 10 to 100 μm^2 . It is cooled well below the critical temperature ($T_c \approx 10$ K) and DC biased close to the switching current ($I_{\text{sw}} \approx 10 \mu\text{A}$). An absorbed photon suppresses local superconductivity and creates a resistive hotspot. The hotspot then expands rapidly (to $\text{k}\Omega$ within 100 ps) under electrothermal feedback and diverts the bias current to the load, creating a detectable voltage pulse. As the current leaves the nanowire, the hotspot cools down, and the detector will reset (within 10s of ns).

More details on SNSPDs can be found in the following review articles: General comparisons of various single-photon detectors are made in Hadfield [2] and Eisaman [17]. Basic physics and applications of SNSPDs are summarized in Nataraajan, Tanner, and Hadfield [18]. A more recent review on progress and challenges in detector metrics and materials can be found in Holzman and Ivry [19]. Architectures of photon-number-resolving SNSPDs are summarized in Mattioli et al. [20]. Waveguide-

integrated SNSPDs are reviewed in Ferrari, Schuck, and Pernice [19]. Packaging and system-level designs can be found in Dauler et al. [21]. A very brief summary of SNSPD readout architectures can be found in McCaughan [22].

Here, we briefly mention a few metrics and challenges that are relevant to and may be addressed by the methods developed in this thesis.

Arrays. Many practical applications, such as single-photon imaging, single-photon spectroscopy, and large-scale photonic quantum information processing, demand large arrays of single-photon detectors. Parallel readout of individual detectors is impractical because of the formidable readout resources and thermal loads. A simple, effective multiplexing scheme is therefore needed [22]. Existing methods include row-column multiplexing (64 pixels) [23], frequency domain multiplexing (16 pixels) [24], time-domain multiplexing (2 pixels) [25], and readout through single-flux quantum (SFQ) circuits (64 pixels) [26, 27]. We recently developed a single-photon imager with ≈ 590 effective pixels (continuous) based on delay-line multiplexing using nanowire coplanar waveguides. In Chapter 5 of this thesis, we demonstrate a 16-pixel discrete array using microstrip delay lines; in Chapter 6, we demonstrate a 65-pixel array on silicon-on-insulator waveguides.

Photon number resolution (PNR). Unlike transition-edge sensors (TESs) [28, 29] or microwave kinetic inductance detectors (MKIDs) [30], SNSPDs work in a highly nonlinear regime and do not have intrinsic photon-number-resolving capability. The common practice to circumvent this limitation is through spatial-multiplexing, where photons are dispersed into an array of detectors packed in a sub-diffraction-limited area [31, 32, 33]. These nanowires may be multiplexed using architectures such as parallel or series nanowire detectors (PND and SND) [32, 34, 20]. More recently, Cahall et al. [35] demonstrated that the rising edge slope from a regular SNSPD depends on photon number and can be used for PNR. In Chapter 4 of this thesis, we use an impedance-matching taper to make the SNSPD photon-number-resolving. In Chapter 5, we demonstrate PNR in a delay-line-multiplexed detector array through

pulse shape analysis.

Timing jitter. The timing jitter determines the temporal resolution of a detector and has a direct impact on communication data rate, spatial resolution in laser ranging, and resolution in fluorescence lifetime or correlation measurement. It has seen significant progress recently [36, 8]. Sub-3-ps jitter was demonstrated in short (5 μm long) NbN nanowires [8] and sub-5-ps jitter was demonstrated in short WSi nanowires [37]. Jitters from electrical noise and detector geometry were largely suppressed in these measurements, and the intrinsic jitter, for the first time, started to make a significant contribution. However, when scaling the detectors to realistic sizes (e.g., 10 μm \times 10 μm or even larger), geometric jitter and electrical jitter (due to decreased slew rate and suppressed switching current) will again limit the overall jitter. In Chapter 3 of this thesis, we propose an impedance-matched readout for SNSPDs to increase output voltage and reduces electrical jitters.

1.2 Microwave dynamics in superconducting nanowires

Because of their small size, superconducting nanowires are usually treated as lumped inductors. Their distributed nature and microwave dynamics were conventionally neglected.

The first systematic experimental study of the microwave dynamics in SNSPDs was performed by Santavicca et al. in 2016 [38]. Self-resonance at 12.5 GHz was observed in a 100 nm-wide, \sim 0.5 mm-long meandered SNSPD. The appearance of self-resonance marks the breakdown of the lumped-inductor limit of SNSPDs. More importantly, the low self-resonance frequency is rather surprising, because it suggests that the microwave signals propagate about more than 20 times slower than that in free space.

The slow speed of light in SNSPDs has a direct impact on the detectors' timing jitter. Previously, it was generally accepted in the community that electrical signals took negligible time to travel across the nanowire, and the photon arrival location and

detector geometry should have little effect on timing jitter. However, if the electrical signals propagate much slower than expected, this assumption may not be true. In the same year, Calandri et al. developed a differential readout method for SNSPDs and directly observed the effect of geometric jitter [39]. By tagging the signal arrival times on both ends of the nanowire, we were able to observe increasing spreading in the time difference between the two channels for detectors with larger areas. By taking the average of the time tags on the two channels, the geometric jitter can be partially canceled out.

Utilizing the effect of geometric jitter, Zhao et al. developed a superconducting nanowire single-photon imager (SNSPI) [40]. In the SNSPI, the nanowire is engineered into a slow-wave coplanar waveguide. It guides the electrical signals at $\approx 2\%c$ (c is the speed of light in free space) and prevents them from hopping across the meander. When a single photon hits the nanowire, it generates a pair of counter-propagating electrical pulses. The arrival times of the electrical pulses on both ends of the nanowire are recorded. The difference between the two gives the photon arrival position, and the average tells the photon arrival time.

1.3 This thesis

This thesis aims to exploit the microwave properties of superconducting nanowires to develop advanced single-photon detector architectures. Two new detector architectures are developed: tapered SNSPD and delay-line-multiplexed SNSPD array.

In tapered SNSPD, we engineer the impedance of the superconducting nanowire. Using impedance-matching taper, we increase the detector output voltage, reduce timing jitter, and enable photon number resolution.

In delay-line-multiplexed SNSPD arrays, we engineer the propagation speed of electrical signals in the nanowire. By using slow-wave microstrips, we demonstrate coincidence detection through timing analysis and photon number resolution through pulse shape analysis.

The thesis is organized as follows:

Chapter 2 summarizes the key theories of kinetic-inductive superconducting nanowire transmission lines. We analyze various forms of transmission lines, propose a nanowire-based tunable forward coupler, and discuss the details of impedance-matching taper.

Chapter 3 introduces the concept of tapered readout. We explain in detail the working mechanism and demonstrate its ability to increase detector output voltage and reduce timing jitters.

Chapter 4 shows that the tapered SNSPD can resolve photon numbers. In this chapter, we present the taper and SNSPD as a single, integrated device, and reported its performance as a whole. For convenience, we give it an acronym, STaND (Superconducting Tapered Nanowire Detector), suggesting that (1) the SNSPD and taper are integrated (from the same material in a single fabrication step), and (2) it is beyond a click/no-click detector.

Chapter 5 presents a scalable coincidence detector array based on delay-line multiplexing. We show coincidence detection in a 16-element array and photon number resolution in a 4-element array.

Chapter 6 reports the progress on a 65-element detector array on silicon-on-insulator photonic waveguides. We present detailed fabrication processes and show some preliminary results.

In Chapter 7, we summarize the major results and give concluding remarks and perspectives on future directions.

Chapter 2

Kinetic-inductive superconducting nanowire transmission lines

Nanowires made from few-nm-thick, dirty, type-II superconducting films have a typical kinetic inductance per unit length of more than 500 times higher than the free-space permeability (μ_0). When incorporated into transmission lines, they have high characteristic impedance (k Ω), slow phase velocity (a few percent of the speed of light in vacuum), and large nonlinearity. These unique properties of kinetic-inductive transmission lines can enable advanced single-photon detector architectures as well as a wide range of compact linear/non-linear microwave components.

In this chapter, we explore some basic theories of kinetic-inductive transmission lines made from thin-film superconductors. We give examples based on thin-film NbN, but the methods can be extended to other similar materials, such as NbTiN, TiN, and WSi.

2.1 Kinetic inductance in superconducting thin films

Kinetic inductance plays a central role in microwave kinetic inductance detectors (MKIDs) [30, 41], kinetic-inductance traveling-wave parametric amplifiers [42], as well as superconducting nanowire single-photon detectors (SNSPDs). Here we give a brief introduction.

Drude description. Superconductors have zero DC resistance because the paired electrons (Cooper pairs) can move freely without scattering. However, since Cooper pairs have inertia, they create inductive reactance in an AC electric field¹. The simple Drude model of conduction in metal captures the basic concept:

$$J = \sigma(\omega)E = \frac{nq^2/m^*}{1/\tau - i\omega}E, \quad (2.1)$$

where $\sigma(\omega)$ is the frequency-dependent complex conductivity; n , q , m^* are the charge carrier density, charge, and mass, respectively; $1/\tau$ is the scattering rate, which approaches 0 when $T \ll T_c$. Writing the conductance into impedance form yields

$$\rho(\omega) = 1/\sigma(\omega) = \frac{1}{\tau} \frac{m^*}{n_s q^2} - i\omega \frac{m^*}{n_s q^2} = R' - i\omega L'_K, \quad (2.2)$$

where the kinetic inductivity [H-m] term becomes explicit:

$$L'_K = m^*/n_s q^2. \quad (2.3)$$

Note that kinetic inductance is also present in normal metals. In normal metals, the electron scattering rate $1/\tau$ is in the THz, so the effect of kinetic inductance only becomes appreciable at THz or optical frequencies. In fact, kinetic inductance plays an essential role in plasmonics at optical frequencies, and the dominance of kinetic inductance over the structure's Faraday inductance marks the signature of the plasmonic regime [44].

London description. In superconductors, it is more appropriate to relate the kinetic inductance to the (London) penetration depth λ_L . From the First London equation, $\mathbf{E} = \frac{\partial}{\partial t}(\mu_0 \lambda_L^2 \mathbf{J}_s)$, we have $J_s = \frac{1}{-i\omega \mu_0 \lambda_L^2} E$ (taking time derivative as $-i\omega$ for an oscillatory field), which is equivalent to the Drude description when setting $\tau = \infty$

¹There is also AC resistive loss due to the presence of normal electrons at finite temperature. From the two-fluid model, normal electrons and super-electrons (Cooper pairs) co-exist, and they are in parallel when viewing the system from a lumped circuit model. At DC, current bypasses the resistive branch and flows through the inductive (Cooper pairs) branch [43].

and $\mu_0\lambda_L^2 = m^*/n_sq$. The kinetic inductivity is simply

$$L'_k = \mu_0\lambda_L^2. \quad (2.4)$$

Note that λ_L (also superconducting gap Δ and superfluid density n_s) depends on temperature T , and in thin films, it varies with film thickness [45].

In actual experiment and device design, we normally use the term “sheet inductance” with the unit of pH per square (pH/sq). The sheet inductance is

$$L_{ks} = L'_k/d = \mu_0\lambda_L^2/d, \quad (2.5)$$

where d is the thickness. It is a convenient parameter when designing microwave devices in the thin film limit ($d \ll \lambda_L$), and it is proportional to the Pearl length $\Lambda_P = 2\lambda^2/d$.

Mattis-Bardeen theory. A more microscopic description of the complex impedance $\sigma(\omega) = \sigma_1(\omega) - i\sigma_2(\omega)$ requires the Mattis-Bardeen theory. At frequencies much less than the superconducting gap energy $2\Delta(0)/h \approx 1.76k_B T_C/h \approx 73 \text{ GHz} \times T_C$, $\sigma(\omega)$ of the superconductor is related to its normal-state conductivity σ_n by [41, 46]

$$\frac{\sigma_1(\omega)}{\sigma_n} = \frac{2}{\hbar\omega} \int_{\Delta}^{\infty} \frac{E^2 + \Delta^2 + \hbar\omega E}{\sqrt{E^2 - \Delta^2} \sqrt{(E + \hbar\omega)^2 - \Delta^2}} [f(E) - f(E + \hbar\omega)] dE \quad (2.6a)$$

$$\frac{\sigma_2(\omega)}{\sigma_n} = \frac{1}{\hbar\omega} \int_{\Delta}^{\Delta+\omega} \frac{E^2 + \Delta^2 - \hbar\omega E}{\sqrt{E^2 - \Delta^2} \sqrt{\Delta^2 - (E - \hbar\omega)^2}} [1 - 2f(E)] dE \quad (2.6b)$$

where $f(E)$ is the distribution function of the quasiparticles (unpaired electrons). In the case of thermal equilibrium, it is given by the Fermi-Dirac distribution $f(E) = 1/(e^{E/k_B T} + 1)$. The quasiparticle density, which contributes to the real conductivity (loss), follows $n_{qp} = 4N_0 \int_{\Delta}^{\infty} dE \frac{E}{\sqrt{E^2 - \Delta^2}} f(E)$.

When $T \ll T_C$ and $\hbar\omega \ll \Delta$, $f(E) \approx e^{-\Delta/k_B T}$, and therefore n_{qp} , σ_1 , and gap suppression ($\Delta - \Delta_0$, caused by the quasiparticles) all vanishes exponentially. In this limit, though σ_1 is diminishingly small, σ_2 remains large and is approximately $\frac{\sigma_n \pi \Delta}{\hbar\omega}$.

The kinetic inductivity is therefore

$$L'_k \approx \frac{\hbar}{\pi\Delta}\rho \quad (2.7)$$

where $\rho = 1/\sigma_n$ is the normal-state resistivity.

Following the BCS relation $\Delta = 1.76k_B T_C$, we can relate the kinetic inductivity to the easily measurable critical temperature and normal state resistivity of the superconducting thin film by $L'_k \approx 1.38\rho/T_C$ [pH-m]; or if we take experimental values reported in the literature, $\Delta = 2.15k_B T_C$ [47], $L'_k \approx 1.78\rho/T_C$ [pH-m]. It is clear here that large normal state resistance gives larger kinetic inductance. The NbN films used in SNSPDs typically have $\rho \approx 250 \mu\Omega \cdot \text{cm}$, and $T_c \approx 8$ K.

The Mattis-Bardeen theory is compatible with the two-fluid model. The two-fluid model assumes the co-existence of normal electron (quasiparticles) and super-electron (Cooper pairs). The normal electron follows theories of normal metal (such as Drude model), while the super-electrons follow London equations.

Nonlinearity and tunability. The kinetic inductance of superconducting thin films strongly depends on film thickness, temperature, and magnetic field. In nanowires, it can be conveniently controlled by bias current [48]. The depairing current and kinetic inductance in current-carrying nanowires have been studied theoretically by Clem and Kogan [48].

In the small-signal limit, which is often used in kinetic-inductance parametric amplifier [42], the kinetic inductance has an approximated quadratic nonlinear form

$$L'_k(I) \approx L'_k(0)[1 + (I/I^*)^2], \quad (2.8)$$

where I is the current in the wire, I^* is comparable to I_c of the wire (10s of μA), and $I \ll I^*$.

For large DC bias current, in the fast relaxation/slow experiment) regime, which is what we experimentally observed in nanowire transmission lines [49] (relaxation time is a few ps, while experiment time constant is about 100s ps for GHz measurement),

the kinetic inductance follows

$$L'_k(0, T)/L'_k(I, T) \approx \left(1 - \left(\frac{|I_b|}{I_d(T)}\right)^n\right)^{1/n}, \quad (2.9)$$

where $I_d(T)$ is the temperature dependent depairing current, n is a fixed value for each $t = T/T_c$ estimated in [48], and its value is 2.21 for $t = 0$ and 2.11 for $t \rightarrow 1$. In principle, if I_b can reach the depairing current I_d , the kinetic inductance will diverge. However, the actual switching current of fabricated nanowires can only reach a fraction ($\approx 70\%$) of I_d due to constrictions [49], which correspond to a $\approx 30\%$ increase of kinetic inductance near switching.

“SNSPD grade” NbN thin film. In the next few sections, we will discuss microwave waveguide/transmission lines made from superconducting NbN thin films used in SNSPDs. Here we list their basic properties and some assumptions that we will use implicitly later.

1. The film thickness $d \approx 5$ nm is much smaller than the London penetration depth $\lambda_L \approx 500$ nm. Current is therefore uniform across the thickness but varies laterally on the order the Pearl length $\Lambda_P = 2\lambda^2/d \approx 100$ μm . When simulating thin-film transmission lines numerically, we may treat them as a zero-thickness layer (e.g., transition boundary layer in COMSOL).
2. The mean free path ($l_{\text{mfp}} \approx 0.5$ nm) is smaller than the film thickness (as well as coherence length $\zeta \approx 5$ nm and λ_L), so local limit applies.
3. The critical temperature $T_c \approx 8\text{--}11$ K is well above our normal operating temperature $T \approx 1\text{--}2$ K, so the quasi-particle population is low and real part of the complex conductivity is near 0. This assumption is marginally valid; however, since we are not dealing with high-Q resonators, qubits, or quantum-limited parametric amplifiers, loss is not a concern in applications discussed in this thesis.

2.2 Superconducting microwave waveguides

When analyzing superconducting microwave waveguides, it is tempting to draw analogies to optical plasmonic waveguides, since both systems are solid-state forms of plasma (charged particle gases). Plasmonics mainly deal with the regime $\omega\tau \gg 1$, where the imaginary part of the conductivity (kinetic inductance) becomes prominent, while superconducting microwave waveguides naturally work in this regime even at low frequency. Here, we examine a few basic plasmonic waveguides and look for their microwave counterparts with superconductors. From these analyses, we can see the similarities and differences between the two systems.

Surface waves. Drude metals can support surface plasmon polariton (SPP) at optical frequencies. It is caused by the collective motion of free electrons at the metal-dielectric interface (shown in Fig 2-1). But can superconductors support microwave SPP?

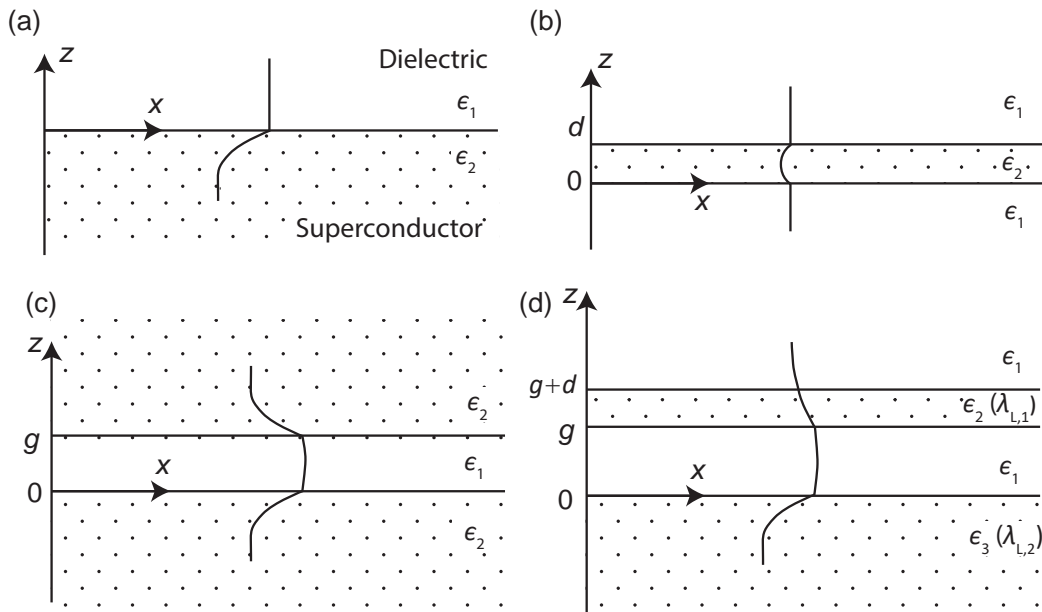


Figure 2-1: Examining superconducting waveguides. (a) Semi-infinite superconductor (surface-wave waveguide); (b) isolated slab/film (insulator-metal-insulator waveguide); (c) parallel plate waveguide (metal-insulator-metal waveguide); (d) thin-film waveguide. (a) and (b) could guide SPP in noble metals at optical frequencies, but could not properly guide microwaves even though London superconductor share many similarities with plasmonic materials.

SPP only supports transverse magnetic (TM) mode, and it has the dispersion relation:

$$\beta = k_0 \sqrt{\frac{\epsilon_1 \epsilon_2}{\epsilon_1 + \epsilon_2}}, \quad (2.10)$$

and the field decays evanescently into the dielectric and metal with $e^{-k_i z}$, where

$$k_i^2 = \beta^2 - k_0^2 \epsilon_i, \quad (2.11)$$

where $k_0 = \omega^2/c^2$ is the wavevector in free space, and ϵ_i ($i = 1, 2$) is the relative permittivity of the corresponding material.

For superconductors at microwave frequencies (GHz), the “metal” permittivity is too small compared to the dielectric $\epsilon_2 \approx -\omega_p^2/\omega^2 = -c/\lambda_L \ll \epsilon_1$ (λ_L is on the order of 100 nm), and the field decay rate is too fast compared to the wave-vector $-k_0^2 \epsilon_2 = \frac{\omega^2 \omega_p^2}{c^2 \omega^2} = 1/\lambda_L^2 \gg \beta^2$. In this condition, we will have $\beta \approx k_0 \sqrt{\epsilon_1}$, $k_2 \approx 1/\lambda_L$, and $k_1 \approx 0$.

Unfortunately, though the field penetrates the superconductor on the order of λ_L , it barely decays in the dielectric. Therefore, superconductor does not guide microwave SPP as metals do at optical frequencies.

To obtain a properly guided SPP, ω should not be too far away from the plasma frequency ω_p (PHz). There have been proposals of using YBCO as low-loss THz plasmonic materials [50]. However, further approaching the gap energy may suffer from quasi-particle losses. One way to support surface waves is to add a dielectric slab on top of the metal [51], which creates an index step to force the field to decay. Alternatively, one may use “spoof plasmon” to support surface waves, where an array of grooves are cut on the metal to produce a layer of effective medium [52].

Similarly, we can prove that an isolated slab or a thin film shown in Fig. 2-1(b) could not properly guide surface waves, and dielectric slabs are needed to force the field to decay.

Metal-insulator-metal waveguide. Metal-insulator-metal (MIM) is another basic plasmonic waveguide configuration (Fig. 2-1(c)). It will not be surprising that superconductors support this mode at microwave frequencies, because even perfect metals do, which is simply a parallel plate waveguide. However, different from parallel plate metallic waveguides, superconductor allows microwaves to penetrate (at all frequencies without dispersion) and enables slow-wave propagation.

The MIM waveguide has the generic dispersion relation (fundamental TM mode) [53]

$$\tanh(k_1 g/2) = -\frac{k_2 \epsilon_1}{k_1 \epsilon_2}, \quad (2.12)$$

where d is the gap spacing and $k_{1,2}$ follows Eq. (2.11).

Here, we are interested in the case of a deep sub-wavelength gap ($g \ll \lambda$). At microwave frequency, $k_1 g/2$ is on the order of $\frac{2\pi/\lambda}{g/2} \ll 1$, we can therefore approximate $\tanh(k_1 g/2)$ as $k_1 g/2$ to the first order. Using this approximations, and substituting $k_1^2 = \beta^2 - \epsilon_1 k_0^2$ and $k_2 \approx 1/\lambda_L$ into Eq. (2.12), we get a simplified dispersion relation:

$$\beta/k_0 = \sqrt{\epsilon_1} \sqrt{1 + 2\lambda_L/g}. \quad (2.13)$$

We can see that reducing g and increasing λ_L will slow down the phase velocity (k_0/β). This phase velocity reduction is quite different from a parallel plate waveguide made from perfect electrical conductors (PEC), where the phase velocity of the fundamental TM mode is independent of the gap size (which is equivalent to setting $\lambda_L = 0$).

Though the superconducting MIM waveguide reduces the phase velocity, it requires very small dielectric gaps. For example, for bulk NbN, λ_L is ≈ 200 nm [43], even if we make $g = 10$ nm, the phase velocity can only be slowed down by 4.6 times (assuming $\epsilon_1 = 1$). Moreover, at this gap size, apart from fabrication challenges, dielectric losses will be dominating.

Next, we show that if we reduce the thickness of the superconductor and contain the charge carrier motion to a very thin layer, the phase velocity will be greatly reduced.

Superconducting thin-film waveguide. As argued previously, a superconducting thin film by itself will not support surface waves, and we need a ground plane to make it a proper waveguide. Figure 2-1(d) shows a generic superconducting thin-film waveguide, where a superconducting thin film (with penetration depth $\lambda_{L,1}$) sits on top of a semi-infinite superconductor ($\lambda_{L,2}$) and filled with dielectric with a relative permittivity of ϵ_1 . The full-field solution of this structure has been worked out by Swihart back in 1960 [54].

With similar assumptions made previously ($\beta^2 \ll 1/\lambda_L^2$), we have a dispersion relation [54]:

$$\begin{aligned} \beta/k_0 &= \sqrt{\epsilon_1} \sqrt{1 + \lambda_{L,2}/g + (\lambda_{L,1}/g) \coth(d/\lambda_{L,1})} \\ &\approx \sqrt{\epsilon_1} \sqrt{1 + \lambda_{L,2}/g + \lambda_{L,1}^2/(dg)}, \end{aligned} \quad (2.14)$$

where the approximation in the second line is valid when $d \ll \lambda_{L,1}$. Also, we can set $\lambda_{L,2} = 0$ to replace the bottom superconducting ground to a PEC.

Now, the phase velocity not only reduces with gap size but also reduces with film thickness. One additional benefit of using thin-film superconductor (dirty type-II films) is that $\lambda_{L,1}$ usually increases with reducing film thickness d [45]. For a 5 nm thick NbN film, which can be routinely produced in our group, $\lambda_L \approx 500$ nm. With $g = 100$ nm, $d = 5$ nm, we can easily have 20 times reduction in phase velocity.

Thin-film slow-wave transmission lines have been demonstrated back in the '90s by Mason and Gould using indium and tantalum [55], and their dependencies on film thickness and temperature were studied. They also recognized that these slow-wave modes were analogous to the space charge waves in a plasma tube.

2.3 Superconducting coplanar waveguides (SCPW)

Superconducting coplanar waveguides (SCPWs) only require single-layer fabrication that is compatible with SNSPD processes. They were recently used to demonstrate a single-photon imager [40] and to form resonators to probe the depairing current of superconducting nanowires [49].

Here we provide some semi-analytical analysis on thin-film SCPWs using transmission line theory. These analyses may help us gain some physical insight and learn how to engineer their properties effectively.²

Figure 2-2 shows the cross-section of a SCPW. The SCPWs discussed here have dimensions (w from 100 nm to 100 μm) much smaller than the wavelength (10s of mm) and can be analyzed in the quasi-static limit. Despite the presence of appreciable longitudinal field components due to the kinetic inductance and index contrast from the substrate, the transverse fields still dominate, and the guided mode is quasi-TEM. In this limit, the geometric capacitance (\mathcal{C}) and Faraday inductance (\mathcal{L}_m) (per unit length) can be solved as 2D static problems using conformal mapping. We then discuss the kinetic inductance contribution from the center conductor (\mathcal{L}_{kc}) and ground (\mathcal{L}_{kg}) at different width limits. These distributed circuit parameters determine the basic properties of SCPW.

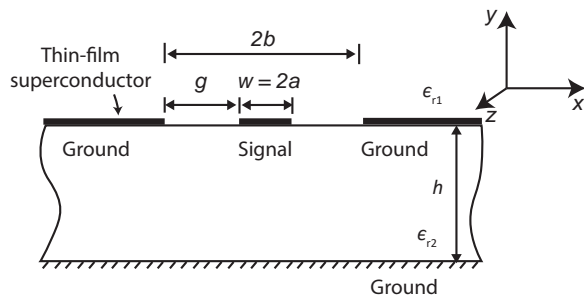


Figure 2-2: Thin-film superconducting coplanar waveguide (SCPW). In examples that follow, we take $\epsilon_{r1} = 1$ (air) and $\epsilon_{r2} = 11.9$ (Si substrate).

Geometric capacitance (\mathcal{C}) and Faraday inductance (\mathcal{L}_m). There is a very rich literature in calculating geometric capacitance and inductance in CPWs using conformal mapping techniques [57, 58]. Since the CPW is symmetric, the E-field lines are parallel to the dielectric interfaces, so we can replace the interfaces with magnetic walls. Doing so allows us to calculate the capacitances of the top and bottom half-planes using conformal mapping independently, and the total capacitance is simply

²After writing this section, we realized that Professor John R. Clem has done very similar analysis for thin-film SCPWs in Ref. [56]. Our analysis is consistent with Ref. [56] but more specific and relevant to the materials and dimensions used in our actual experiments.

the sum of the two.

The top half-plane of the CPW can be transformed into a parallel plate capacitor using the Schwarz-Christoffel transformation, $w = \int_{z_0}^z \frac{dz}{\sqrt{(z-a)(z-b)}}$, and the total line capacitance (i.e., capacitance per unit length) of the top half-plane \mathcal{C}_0 is

$$\mathcal{C}_1 = 2\epsilon_{r1}\epsilon_0 \frac{K(k_1)}{K(k'_1)}. \quad (2.15)$$

where $k_1 = a/b$, $k'_1 = \sqrt{1 - k_1^2}$, and K is the complete elliptic integral of the first kind

$$K(k) = \int_0^1 \frac{1}{\sqrt{(1-x^2)(1-k^2x^2)}} dx. \quad (2.16)$$

Similarly, the magnetic inductance per unit length (from the inductance of parallel plates) is

$$\mathcal{L}_1 = \mu_0 \frac{K(k'_1)}{2K(k_1)}. \quad (2.17)$$

Most of the time, we mount our substrate on a metal plate (grounded) to thermalize it to the cryostat's base temperature. Two cascaded conformal mappings are needed to transform the conductor-backed half-plane to a parallel plate [58], and its capacitance is

$$C_2 = 2\epsilon_0\epsilon_{r2} \frac{K(k_2)}{K(k'_2)}, \quad (2.18)$$

where $k_2 = \tanh(\pi a/2h)/\tanh(\pi b/2h)$, and $k'_2 = \sqrt{1 - k_2^2}$. Note that when $h \gg b$, which is the case for superconducting nanowire CPW on standard silicon substrate ($\approx 500 \mu\text{m}$), $k_2 \approx k_1 = a/b$, meaning that the ground is too far from the center conductor and can be ignored.

Similarly, the inductance of the bottom half-plane is

$$\mathcal{L}_2 = \mu_0 \frac{K(k'_2)}{2K(k_2)}. \quad (2.19)$$

The total capacitance (per unit length) of the CPW is therefore

$$\mathcal{C} = \mathcal{C}_1 + \mathcal{C}_2 = 2\epsilon_0\epsilon_{r1}\frac{K(k_1)}{K(k'_1)} + 2\epsilon_0\epsilon_{r2}\frac{K(k_2)}{K(k'_2)}, \quad (2.20)$$

and the total Faraday inductance (per unit length) is

$$\mathcal{L}_m = (\mathcal{L}_1^{-1} + \mathcal{L}_2^{-1})^{-1} = \mu_0/[2\frac{K(k_1)}{K(k'_1)} + 2\frac{K(k_2)}{K(k'_2)}]. \quad (2.21)$$

Figure 2-3 shows the calculated line capacitance as a function of center conductor width w at different gap sizes g . We take the substrate as Si ($\epsilon_r = 11.9$) and top as air. In general, smaller g and/or larger w give larger \mathcal{C} . Figure 2-4 shows the corresponding characteristic impedance and phase velocity without considering the kinetic inductances, i.e., a normal metal CPW.

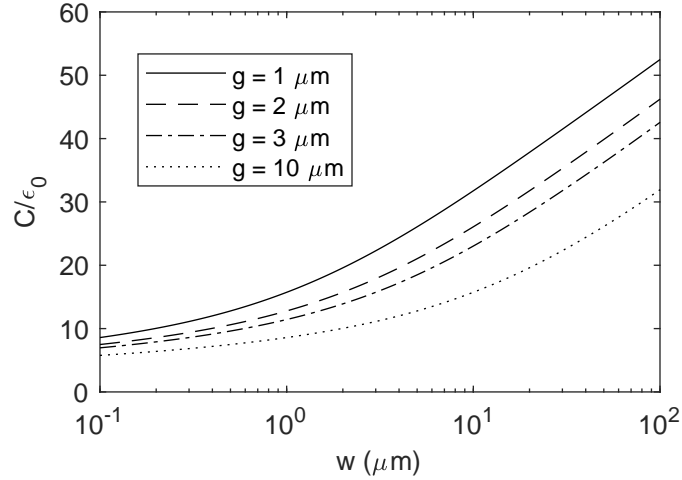


Figure 2-3: Line capacitance (\mathcal{C}) of the CPW (see Fig. 2-2) as a function of center conductor width (w) at different gap sizes (g). We take the substrate as Si ($\epsilon_r = 11.9$) and top as air.

In addition to single-material substrates (e.g., Si, sapphire), we often fabricate SCPWs on multi-layered substrates (e.g., Si with thermal oxide top layer). In principle, the line capacitance can be calculated using the partial capacitance (PC) approach[57, 58]. In the PC approach, the total capacitance is the sum of the air capacitance (assuming no dielectrics exist) and the added capacitance from each dielectric layer by assuming a relative permittivity of $\epsilon_r - 1$. However, we found that

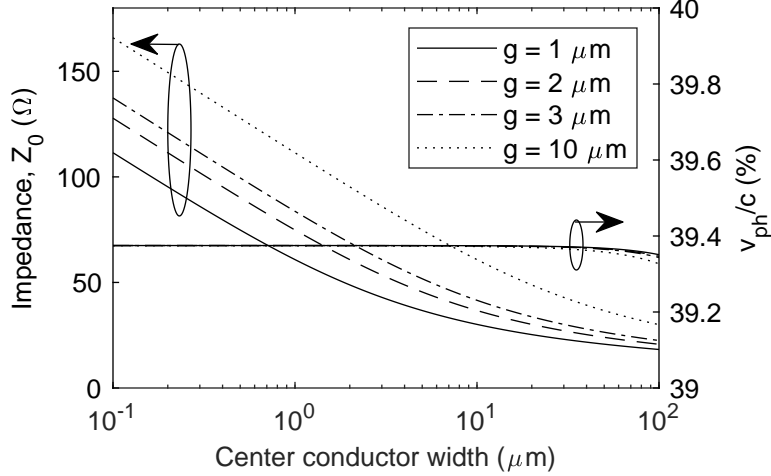


Figure 2-4: Characteristic impedance (Z_0) and phase velocity (v_{ph}) of normal metal CPW. The characteristic impedance decreases with increasing center conductor width or decreasing gap size due to larger line capacitance. The phase velocity is relatively insensitive to geometry change and is mainly affected by the dielectric constant of the substrate material.

this approach yielded large errors when calculating CPW capacitances on SiO_2 -on-Si substrate (a commonly used substrate in our fabrication). We later realized that double-layer substrates, whose second layer (e.g., $\epsilon_{\text{Si}} = 11.9$) has higher index than the first layer (e.g., $\epsilon_{\text{SiO}_2} = 3.9$), is a known issue with conventional (parallel) partial capacitance (PPC) approaches [59, 60]. In this case, a modified series partial capacitance (SPC) approach may be used [61].

Kinetic inductance of the center conductor (\mathcal{L}_{kc}) When the center conductor width (w) is much smaller than the Pearl length ($\Lambda_{\text{P}} = 2\lambda_{\text{L}}^2/d$, $\approx 100 \mu\text{m}$ in a typical 5 nm NbN film), the current in the wire is uniform, and the kinetic inductance per unit length of the wire is simply $L'_{\text{k}}/(wd) = L_{\text{ks}}/w$, where w and d is the width and thickness of the center conductor.

However, when w become comparable to Λ_{P} , currents squeeze towards the edge, reducing the effective cross-section and increasing the kinetic inductance. This regime is relevant because we often need to taper the SCPW impedance from $\text{k}\Omega$ to 50Ω , and 50Ω SCPW usually has w around $100 \mu\text{m}$. Here we calculate the current distribution in wide wires and estimate their kinetic inductances.

We start with Ampere's law:

$$\nabla \times \mathbf{B} = \mathbf{J}_n + \mathbf{J}_s + \mu_0 \frac{\partial}{\partial t} \mathbf{D} \quad (2.22)$$

where \mathbf{J}_s and \mathbf{J}_n are the super and normal currents. First, since the physical size of the wire (100s of μm) is much smaller than the wavelength (10s of mm), we assume quasi-magnetostatic limit and drop $\frac{\partial}{\partial t} \mathbf{D}$. Second, we assume $T \ll T_c$ and $\mathbf{J}_n \rightarrow 0$. Third, since the supercurrent flows along the wire without forming vortices, it is convenient to use the London gauge $-\mu_0 \lambda_L^2 \mathbf{J}_s = \mathbf{A}$, where \mathbf{A} is the vector potential and $\nabla \times \mathbf{A} = \mathbf{B}$. Applying these three simplifications, we reach the Maxwell-London equation:

$$\nabla^2 \mathbf{A} = \begin{cases} \mathbf{A}/\lambda_L^2, & \text{in superconductor} \\ 0, & \text{outside superconductor} \end{cases} \quad (2.23)$$

Due to symmetry, \mathbf{A} only has $A_z(x, y)$ component (refer to Fig. 2-2 for coordinate definition), and we can solve it numerically in 2D with a Helmholtz equation inside the superconductor and a Laplace equation outside.

Once the $A_z(x, y)$ is solved, we can get the current distribution as $J_s(x, y) = -\frac{A_z(x, y)}{\mu_0 \lambda_L^2}$ (J_s is along the z direction only).

Figure 2-5 shows the calculated the current distribution along the width of the center conductor. $\mu_0 \lambda_L^2/d = 80$ pH, $d = 5$ nm, and w varies from 100 nm to 100 μm . When solving the Helmholtz equation, we set the boundary conditions on the two edges ($x = 0$ and $x = w$) to be 1.

Since the kinetic inductance carries the kinetic energy of the charge carriers, we can relate \mathcal{L}_k (per unit length) to the drift motion of Cooper pairs: $\frac{1}{2} \mathcal{L}_k I^2 = \int \frac{1}{2} m^* v^2 n_s da$, where $I = \int J_s da$ and the integration is over the cross-section of the wire. Microscopically (in a classical sense), we know that $J_s = n_s q v_d$, where n_s , q , and v_s are the density, charge, and drift velocity of the Cooper pairs. From Eq. (2.3) and (2.4), we have $\mu_0 \lambda_L^2 = m^*/(n_s q^2)$. For a 5 nm thick NbN film with $\mu_0 \lambda_L^2/d = 80$ pH, using $q = 2e$ and $m^* \approx 2m_e$ [62], we have the superfluid density $n_s \approx m_e/(2\mu_0 \lambda_L^2 e^2) \approx 4.4 \times 10^{19}$

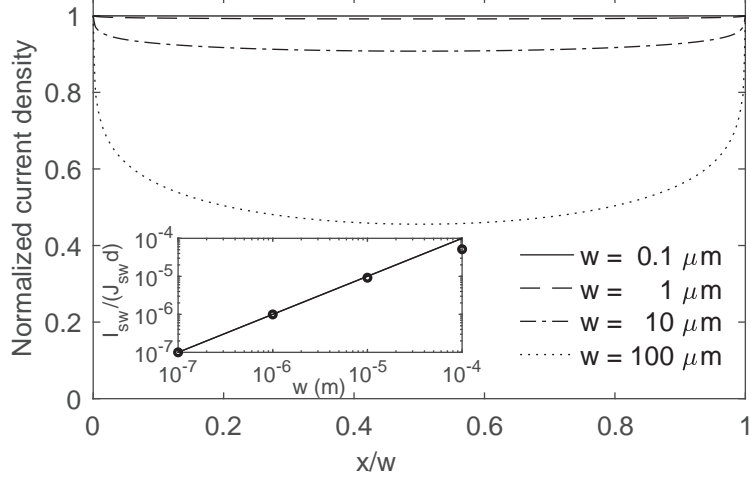


Figure 2-5: Current distribution along the width of the center conductor. When the center conductor width (w) becomes comparable to the Pearl length, current is no longer uniformly distributed in the wire. Here, the current densities at the edges are normalized to 1 for all w . This allows us to calculate the wires' switching currents (I_{sw}). Inset: $I_{\text{sw}}/(J_{\text{sw}}d)$ as a function of w , where J_{sw} is the critical current density, and d is the film thickness. Due to the non-uniform current density distribution, the actual switching current deviates from the linear scaling (solid line, $I_{\text{max}}/(J_{\text{sw}}d) = w$). In this calculation, the sheet inductance is $\mu_0\lambda_L^2/d = 80$ pH, corresponding to $\Lambda_P = 127$ μm .

$\text{cm}^{-3} = 0.04 \text{ nm}^{-3}$, which is about 3 orders of magnitude lower than gold and copper. Note that n_s here is the density that participates to the current response (superfluid density), not the condensate density [63]. If we run 10 μA current down a 100 nm wire (made from the same 5 nm NbN film), $v_d = 1.4 \times 10^3$ m/s, which is incredibly fast and carries large kinetic energy. Note that the Fermi velocity of gold is only 1.6×10^6 m/s. From the 3 equations listed above, we can get \mathcal{L}_k in terms of current density in the center conductor:

$$\mathcal{L}_{\text{kc}} = \mu_0\lambda_L^2 \frac{\int J_s^2 da}{I^2} = \mu_0\lambda_L^2 \frac{\int J_s^2 da}{(\int J_s da)^2} \quad (2.24)$$

Note that the kinetic inductance can also be rigorously derived from the Poynting theorem with an expression that works for generic plasmonic structures: $L_k = -(1/\omega)\text{Im}[1/\sigma] \int_{V_{\text{metal}}} |\mathbf{J}|^2 dv / |\mathbf{I}|^2$ [64].

For convenience, we define a screening factor s that relates the actual center conductor kinetic inductance \mathcal{L}_{kc} to the kinetic inductance assuming uniform current

distribution:

$$s = \frac{\mathcal{L}_{kc}}{L'_k/(wd)} = \frac{\mathcal{L}_{kc}w}{\mu_0\lambda_L^2/d} = wd \frac{\int J_s^2 da}{(\int J_s da)^2} \quad (2.25)$$

Figure 2-6 shows s -factor as a function of w with $\mu_0\lambda_L^2/d = 80, 100,$ and 120 pH. When wire width increases, current crowds towards the edge and makes the effective cross-section smaller, which in turn makes s larger.

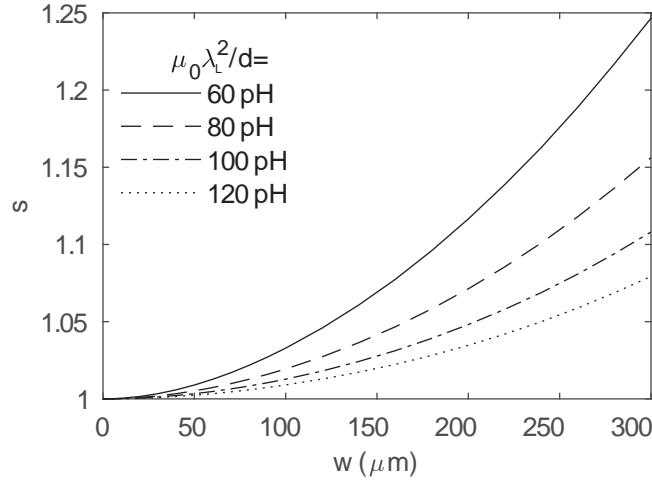


Figure 2-6: s -factor vs. center conductor width at different sheet inductance ($\mu_0\lambda_L^2/d$). When the sheet inductance increases, current is able to penetrate deeper to the wire and the actual inductance is more close to that with uniform current distribution.

Kinetic inductance of the ground plane (\mathcal{L}_{kg}). SCPW ground planes carry the return current and are also made from thin-film superconductors, so they contribute kinetic inductance as well.

Current distribution in the ground plane can be similarly calculated using Eq. (2.23). Instead of a wire, the ground plane is a semi-infinite sheet. Current is maximum at the edge and exponentially decays towards the side.

Figure 2-7 shows the calculated current distribution in the ground plane, with sheet inductances $L_{ks} = \mu_0\lambda_L^2/d$ from 60 to 120 pH/sq. The inductance can be calculated using Eq. (2.24), but with a $1/2$ in front since there are two grounds, each carrying half of the return current:

$$\mathcal{L}_{\text{kg}} = \frac{1}{2} \mu_0 \lambda_L^2 \frac{\int J_s^2 da}{(\int J_s da)^2}, \quad (2.26)$$

where J_s is current distribution in a semi-infinite film with maximum current on the edge.

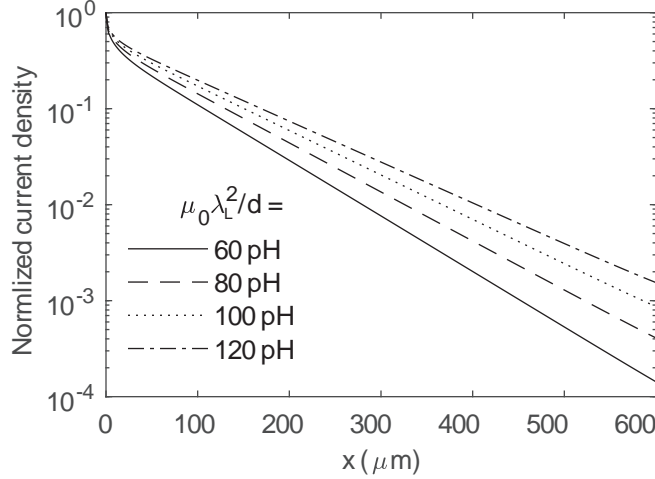


Figure 2-7: Current distribution in the semi-infinite SCPW ground plane. Current density decays exponentially from the edge ($x = 0$). On each ground, the total current is half of that in the center conductor (and with opposite directions). From $\mu_0 \lambda_L^2 / d = 60$ to 120 pH, the kinetic inductance contributions of the ground ($2\mathcal{L}_{\text{kg}}$) are 477, 538, 593, and 644 nH/m.

Putting everything together. The total inductance per unit length is the sum of Faraday inductance and kinetic inductance from both center conductor and side grounds:

$$\mathcal{L} = \mathcal{L}_m + \mathcal{L}_{\text{kc}} + \mathcal{L}_{\text{kg}} \quad (2.27)$$

Figure 2-8 compares the 3 inductance contributions in the thin-film SCPW. When the center conductor is $< 1 \mu\text{m}$, we can safely ignore the Faraday and ground inductance.

Using transmission line theory, we can calculate the characteristic impedance as

$$Z_0 = \sqrt{\frac{\mathcal{L}}{C}}, \quad (2.28)$$

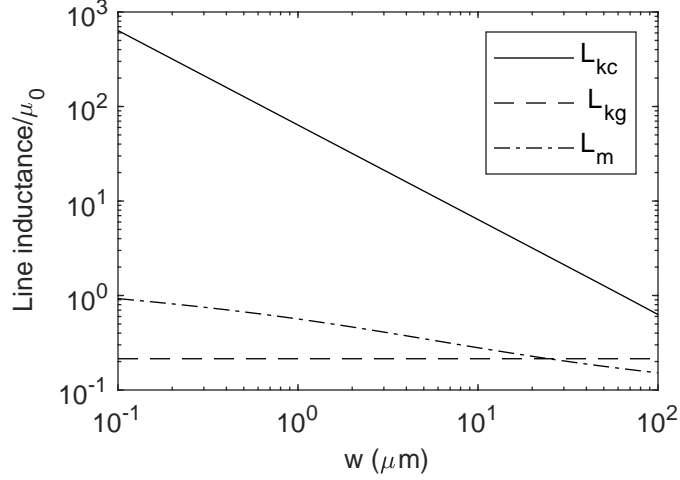


Figure 2-8: Inductance contributions in SCPW. \mathcal{L}_{kc} : kinetic inductance from the center conductor; \mathcal{L}_{kg} : kinetic inductance contribution from the ground; \mathcal{L}_m : Faraday inductance. In nanowire SCPW, L_{kc} dominates.

and phase velocity as

$$v_{\text{ph}} = \frac{1}{\sqrt{\mathcal{L}\mathcal{C}}}. \quad (2.29)$$

Figure 2-9 shows the characteristic impedance (Z_0) and phase velocity (v_{ph}) as a function of center conductor width w ($\mu_0\lambda_L^2/d = 80$ pH, $g = 3$ μm). The lines are from semi-analytical formulas listed above, while symbols are full-wave mode solutions calculated using COMSOL. Figure 2-9(b) includes s -factor and ground inductances, which mainly correct deviation for large w .

The semi-analytical analysis in this section is based on the quasi-TEM mode. We noticed that when the SCPW is too wide ($\gtrsim 500$ μm), this assumption fails and full-wave simulation becomes necessary. However, we rarely go to this limit, since Z_0 reaches $50\ \Omega$ at $w = 140$ μm and further increasing w serves no purpose in our applications.

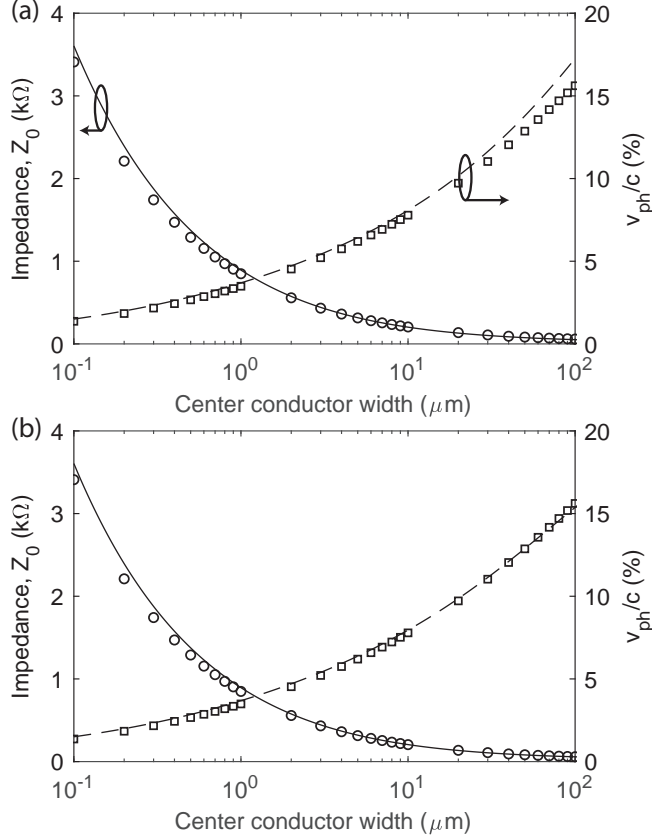


Figure 2-9: Z_0 and v_{ph} of SCPW as a function of center conductor width ($\lambda_L^2/d = 80$ pH and $g = 3 \mu\text{m}$). (a) Without s -factor and \mathcal{L}_{kg} correction. (b) Including s -factor and \mathcal{L}_{kg} correction. Symbols: full-wave finite-element mode solution using COMSOL; lines: semi-analytical solutions based on transmission-line theory. It can be seen that the semi-analytical solutions match well with full-field solutions, and s -factor and \mathcal{L}_{kg} correction is important only when w becomes comparable to Λ_p .

2.4 Superconducting nanowire microstrip and “tunnel” transmission lines

In this section, we briefly discuss two additional implementations of nanowire transmission lines: microstrip and “tunnel” transmission line. Compared to SCPWs, both of them have increased line capacitances and hence smaller characteristic impedances and phase velocities given the same center conductor width.

Microstrip. Figure 2-10 shows the simulated impedance and phase velocity as a function of nanowire width. In chapter 5 and 6, we used it as delay lines to multiplex

detector arrays. When making single-photon imagers [40], compared to SCPW, microstrip allows denser packing, and the dielectric spacer and top (or bottom) ground can form optical cavities to enhance light absorption. It also avoids absorption in the side ground and is more appropriate for photonic waveguide integration.

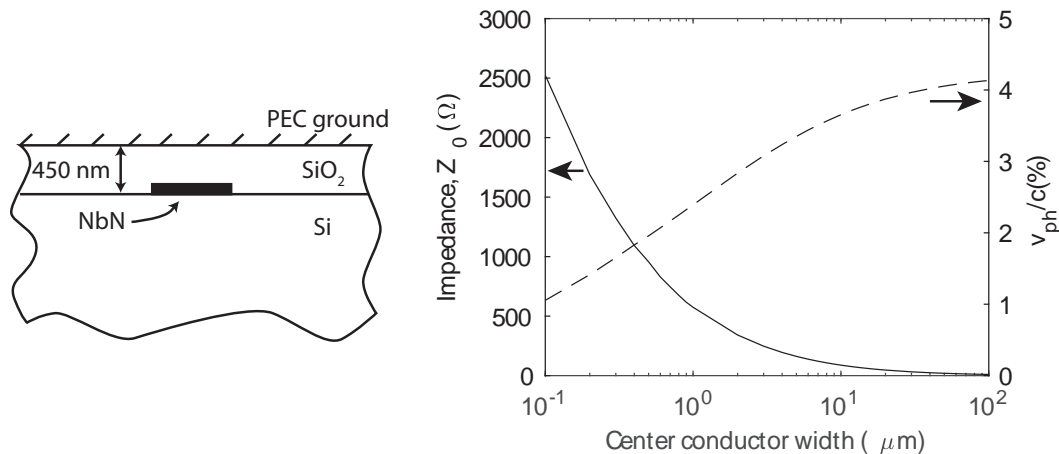


Figure 2-10: Characteristic impedance and phase velocity of thin-film superconducting microstrip. $\mu_0\lambda_L^2/d = 80$ pH.

“Tunnel” transmission line. We call the structure in Fig. 2-11 a “tunnel” transmission line because the microwave travels like in a tunnel formed by the top ground. It is a combination of CPW and microstrip. The top ground connects the two side ground and prevents CPW to slotline mode conversion when bending the transmission line (almost unavoidable when making long devices such as traveling wave amplifier and impedance-matching tapers). We made some by first fabricating the bottom CPW, then exposing hydrogen silsesquioxane using electron-beam lithography along the CPW, and finally cover the top with a metal ground plane after development. Note that since the mode now is tightly confined in the “tunnel”, losses from the dielectrics and top ground start to become significant. Therefore, it is highly desirable to use superconducting material (either with or without large kinetic inductance) for the top ground material.

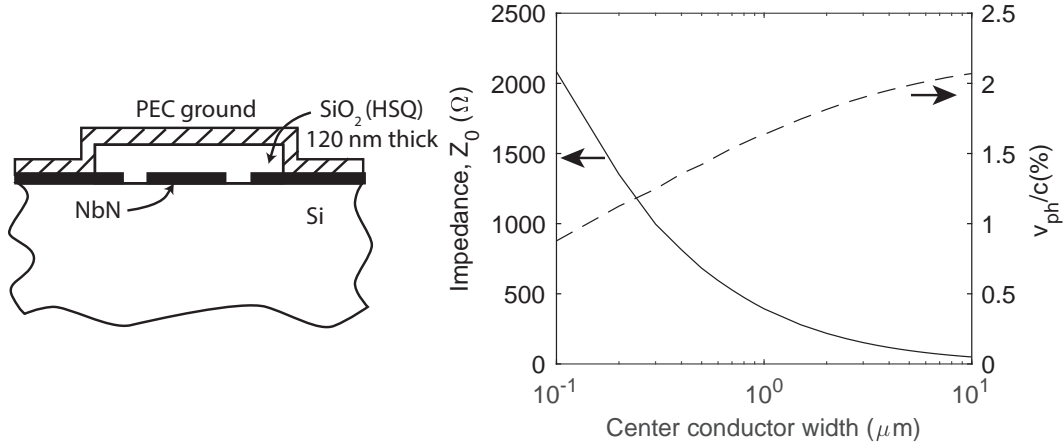


Figure 2-11: “Tunnel” transmission line. gap: 1 μm ; $\mu_0\lambda_L^2/d = 80$ pH/sq; dielectric extends 2 μm on the side ground.

2.5 Coupled nanowire transmission lines

The kinetic-inductive nanowire transmission lines may enable a wide range of ultra-compact linear/non-linear microwave components. Here we show one example—nanowire microwave coupler.

When two transmission lines/waveguides are brought close (Fig. 2-12(a)), the coupling between them causes mode splitting: common mode (c-mode, or even mode) and differential mode (π -mode, or odd mode) (Fig. 2-12(b)). These eigenmodes/supermodes have different effective indices and propagation constants, β_c and β_π . When the input is injected into a single transmission line, for example transmission line a , it is a superposition of the two eigenmodes, and the energy will shuttle between the two transmission lines with a periodicity of $l_\pi = \pi/\Delta\beta = \pi/(\beta_c - \beta_\pi)$.

In optical waveguide/fiber couplers, coupling originates from induced polarization in the secondary waveguide from primary waveguide’s evanescent E -field. It is usually weak and can be treated perturbatively. In this case, coupled-mode theory comes in handy [65]. In microwave transmission line couplers, however, both capacitive and inductive couplings exist (and both can be strong); and extra care needs to be taken on impedance matching, reflection, and bandwidth.

The kinetic-inductive transmission line couplers made from superconducting nanowire lie somewhere in between of these cases. Here, we analyze the nanowire coupler using

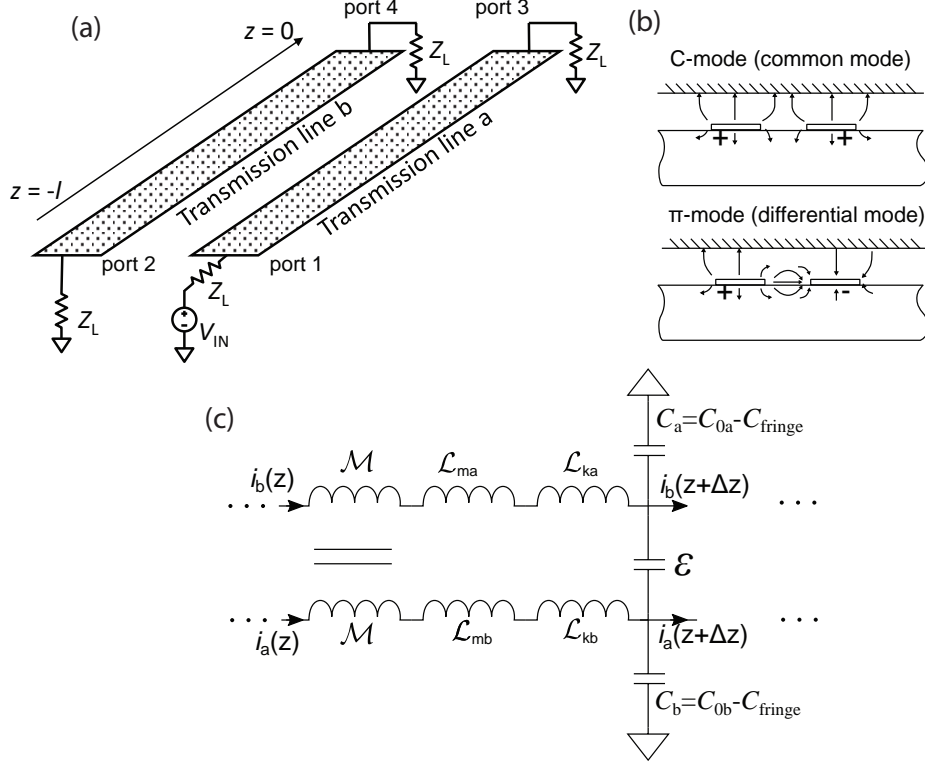


Figure 2-12: Coupled nanowire transmission line. (a) Schematic for two coupled transmission lines. (b) Electric field distribution for the common and differential mode. (c) A unit cell for the distributed circuit model for the coupled lines. All circuit elements are per unit length values multiplied by Δz .

transmission line theories in the quasi-static limit (which is not so accurate for microstrips, but the analysis can give us some insight on how nanowire couplers work), and compare the results to optical waveguide couplers and conventional metallic microwave couplers.

The configuration in Fig. 2-12(a) can be approximately modeled using a coupled LC ladder, whose unit cell is shown in Fig. 2-12(c). $\mathcal{L}_{ma,mb}$ and $\mathcal{L}_{ka,kb}$ are the Faraday and kinetic inductance (per unit length) of each line, \mathcal{M} and \mathcal{E} are the mutual inductance and capacitance between the two lines, and $\mathcal{C}_{a,b}$ are the self-capacitances. $\mathcal{C}_{a,b}$ are slightly different from their uncouple values $\mathcal{C}_{0a,0b}$ because of modified fringe fields ($\mathcal{C}_{\text{fringe}}$). A more accurate circuit decomposition can be found in Ref[66]. This coupled transmission line is governed by the coupled Telegrapher's equations:

$$-\partial_z \begin{bmatrix} i_a \\ i_b \end{bmatrix} = \begin{bmatrix} \mathcal{C}_a + \mathcal{E} & -\mathcal{E} \\ -\mathcal{E} & \mathcal{C}_b + \mathcal{E} \end{bmatrix} \partial_t \begin{bmatrix} v_a \\ v_b \end{bmatrix} \quad (2.30a)$$

$$-\partial_z \begin{bmatrix} v_a \\ v_b \end{bmatrix} = \begin{bmatrix} \mathcal{L}_a + \mathcal{M} & -\mathcal{M} \\ -\mathcal{M} & \mathcal{L}_b + \mathcal{M} \end{bmatrix} \partial_t \begin{bmatrix} i_a \\ i_b \end{bmatrix} \quad (2.30b)$$

where we have we have grouped Faraday and kinetic inductance into a single term $\mathcal{L}_{a/b} = \mathcal{L}_{ka/kb} + \mathcal{L}_{ma/mb}$. Taking partial derivative with respect to z of Eq. (2.30b) and substituting in Eq. (2.30a) we have

$$\begin{aligned} \partial_z^2 \begin{bmatrix} v_a \\ v_b \end{bmatrix} &= \begin{bmatrix} \mathcal{L}_a + \mathcal{M} & -\mathcal{M} \\ -\mathcal{M} & \mathcal{L}_b + \mathcal{M} \end{bmatrix} \begin{bmatrix} \mathcal{C}_a + \mathcal{E} & -\mathcal{E} \\ -\mathcal{E} & \mathcal{C}_b + \mathcal{E} \end{bmatrix} \partial_t^2 \begin{bmatrix} v_a \\ v_b \end{bmatrix} \\ &= \begin{bmatrix} (\mathcal{L}_a + \mathcal{M})(\mathcal{C}_a + \mathcal{E}) + \mathcal{M}\mathcal{E} & -\mathcal{E}(\mathcal{L}_a + \mathcal{M}) - \mathcal{M}(\mathcal{C}_b + \mathcal{E}) \\ -\mathcal{M}(\mathcal{C}_a + \mathcal{E}) - \mathcal{E}(\mathcal{L}_b + \mathcal{M}) & (\mathcal{L}_b + \mathcal{M})(\mathcal{C}_b + \mathcal{E}) + \mathcal{E}\mathcal{M} \end{bmatrix} \partial_t^2 \begin{bmatrix} v_a \\ v_b \end{bmatrix} \\ &= \begin{bmatrix} \alpha_a & \gamma_a \\ \gamma_b & \alpha_b \end{bmatrix} \partial_t^2 \begin{bmatrix} v_a \\ v_b \end{bmatrix} \end{aligned} \quad (2.31)$$

Eigensolutions. Assuming the voltages in the two lines $v_{a,b}(z, t)$ propagate in the form of $v_{a,b} = V_{a,b}e^{j\omega t - j\beta z}$ for the eigenmodes, we can solve the dispersion relation

$$\frac{\beta_{c,\pi}^2}{\omega^2} = \frac{(\alpha_a + \alpha_b) \pm \sqrt{(\alpha_a - \alpha_b)^2 + 4\gamma_a\gamma_b}}{2}, \quad (2.32)$$

where c and π denotes the common and differential modes, respectively. And for the two eigenmodes, the voltage ratio on the two lines are

$$R_{c,\pi} = \frac{v_b}{v_a} = \frac{2\gamma_b}{\alpha_a - \alpha_b \pm \sqrt{(\alpha_a - \alpha_b)^2 + 4\gamma_a\gamma_b}}. \quad (2.33)$$

Substituting the eigenmode solution and voltage ratio on the two lines back to

Eq.(2.30a) or (2.30b), we can get the impedances for the c and π modes

$$Z_{c,\pi} = \frac{v_a}{i_a} = \frac{\omega}{\beta_{c,\pi}}(\mathcal{L} + \mathcal{M} - R_{c,\pi}\mathcal{M}) = \frac{\beta_{c,\pi}}{\omega(\mathcal{C}_a + \mathcal{E} - R_{c,\pi}\mathcal{E})}. \quad (2.34)$$

Eigenmodes for symmetric nanowire coupler. For a symmetric coupler, $\mathcal{L}_a = \mathcal{L}_b = \mathcal{L}$, $\mathcal{C}_a = \mathcal{C}_b = \mathcal{C} = \mathcal{C}_0 - \mathcal{C}_{\text{fringe}}$. The propagation constant for the c-mode reduces to

$$\beta_c = \omega\sqrt{\mathcal{L}\mathcal{C}} = \omega\sqrt{\mathcal{L}(\mathcal{C}_0 - \mathcal{C}_{\text{fringe}})}, \quad (2.35)$$

and the propagation constant for the π -mode reduces to

$$\beta_\pi = \omega\sqrt{\mathcal{L}\mathcal{C}}\sqrt{1 + \frac{2\mathcal{E}}{\mathcal{C}} + \frac{2\mathcal{M}}{\mathcal{L}} + \frac{4\mathcal{M}\mathcal{E}}{\mathcal{L}\mathcal{C}}} \approx \omega\sqrt{\mathcal{L}\mathcal{C}}\sqrt{1 + 2\mathcal{E}/\mathcal{C}}. \quad (2.36)$$

where we assumed $\mathcal{M}/\mathcal{L} \ll 1$.

Note that β_c here is slightly smaller than that of the uncoupled nanowire transmission line ($\beta_0 = \sqrt{\mathcal{L}\mathcal{C}_0}$) because $\mathcal{C} = \mathcal{C}_0 - \mathcal{C}_{\text{fringe}}$ (slightly reduced capacitance to the ground).

Similarly, the impedance for the c-mode is

$$Z_c = \sqrt{\frac{\mathcal{L}}{\mathcal{C}}} = \sqrt{\frac{\mathcal{L}}{\mathcal{C}_0 - \mathcal{C}_{\text{fringe}}}}, \quad (2.37)$$

and the impedance for the π -mode is

$$Z_\pi = \sqrt{\frac{\mathcal{L}}{\mathcal{C}}}\frac{\sqrt{1 + \frac{2\mathcal{E}}{\mathcal{C}} + \frac{2\mathcal{M}}{\mathcal{L}} + \frac{4\mathcal{M}\mathcal{E}}{\mathcal{L}\mathcal{C}}}}{1 + 2\mathcal{E}/\mathcal{C}} \approx \sqrt{\frac{\mathcal{L}}{\mathcal{C}}}\frac{1}{\sqrt{1 + 2\mathcal{E}/\mathcal{C}}}. \quad (2.38)$$

The splitting in propagation constant $\Delta\beta = \beta_\pi - \beta_c = \omega\sqrt{\mathcal{L}\mathcal{C}}(\sqrt{1 + 2\mathcal{E}/\mathcal{C}} - 1)$ is dominated by capacitive coupling (\mathcal{E}). For a 3 dB coupler, we need a coupling length of

$$l_{\pi/2} = \frac{1}{4}\lambda_c/(\sqrt{1 + 2\mathcal{E}/\mathcal{C}} - 1), \quad (2.39)$$

where λ_c is the guided wavelength for the common mode.

It is tempting to increase \mathcal{E} by placing the two wires very close, but this will increase impedance splitting, which causes reflection and backward coupling. Without considering resonances caused by reflections from the far-end load ($z = 0$), the reflection coefficients at the input transmission line a and back-coupling to the neighboring transmission line b are $\Gamma_{a,b} = \frac{1}{2}(\frac{Z_c - Z_L}{Z_c + Z_L} \pm \frac{Z_\pi - Z_L}{Z_\pi + Z_L})$. As a rough estimation, we assume $Z_c = Z_L$ and get $\Gamma_{a,b} \approx \mp \frac{1}{2} \frac{\sqrt{1+2\mathcal{E}/\mathcal{C}} - 1}{\sqrt{1+2\mathcal{E}/\mathcal{C}} + 1} \approx \pm \frac{1}{4}(\sqrt{1+2\mathcal{E}/\mathcal{C}} - 1)$, meaning that if we want to reduce Γ , we have to work in the weak coupling regime and proportionally increase the coupling length.

In optical waveguide/fiber couplers, weak coupling is feasible because the optical wavelength is small and one can pack 1000s of guided wavelengths within a mm footprint.

At microwave frequencies, because of the long wavelength (30 mm at 10 GHz), a single-section forward coupler requires larger footprint (e.g., in [67], a symmetric 10 GHz, 3 dB coupler requires > 100 mm length, which is ≈ 5.2 guided wavelengths). Therefore, it is more common to design hybrids as backward couplers [51]. By considering the reflection at the far-end of the coupler, the effective c - and π -mode impedances at the input are modified by the impedance translation rule $Z_{c,\pi}(z = -l) = Z_{c,\pi} \frac{Z_L + jZ_{c,\pi} \tan \beta_{c,\pi}(-l)}{Z_{c,\pi} + jZ_L \tan \beta_{c,\pi}(-l)}$. In backward couplers, l is properly chosen to make Γ_b the desired coupling ratio.

In nanowire transmission lines, since the guided wavelength is about 2 orders of magnitude smaller than that in conventional transmission lines, a forward coupler can be made compact (100s of μm for 10 GHz coupler).

S-parameters for asymmetric coupler. Here we calculate S-parameters for a finite length coupler. The treatment is valid for both kinetic-inductive and normal transmission line couplers. The voltage ($V_a(z)$ and $V_b(z)$) and current ($I_a(z)$ and $I_b(z)$) in transmission line a and b can be written as the superposition of the forward and backward propagating c and π modes:

$$V_a(z) = A_1 e^{-j\beta_c z} + A_2 e^{j\beta_c z} + A_3 e^{-j\beta_p z} + A_4 e^{j\beta_p z} \quad (2.40a)$$

$$V_b(z) = R_c(A_1 e^{-j\beta_c z} + A_2 e^{j\beta_c z}) + R_\pi(A_3 e^{-j\beta_p z} + A_4 e^{j\beta_p z}) \quad (2.40b)$$

$$I_a(z) = \frac{1}{Z_c}(A_1 e^{-j\beta_c z} - A_2 e^{j\beta_c z}) + \frac{1}{Z_\pi}(A_3 e^{-j\beta_p z} - A_4 e^{j\beta_p z}) \quad (2.40c)$$

$$I_b(z) = \frac{R_c}{Z_c}(A_1 e^{-j\beta_c z} - A_2 e^{j\beta_c z}) + \frac{R_\pi}{Z_\pi}(A_3 e^{-j\beta_p z} - A_4 e^{j\beta_p z}) \quad (2.40d)$$

where $Z_{c/\pi}$ and $\beta_{c/\pi}$ are characteristic impedance and propagation constant for the c and π modes, and A_i are coefficients to be matched later through boundary conditions.

The boundary conditions at the four ports follow

$$[V_{\text{IN}} - V_a(z = -l)]/Z_{La} = I_a(z = -l) \quad (2.41a)$$

$$-V_b(z = -l)/Z_{Lb} = I_b(z = -l) \quad (2.41b)$$

$$V_a(z = 0)/Z_{La} = I_a(z = 0) \quad (2.41c)$$

$$V_b(z = 0)/Z_{Lb} = I_b(z = 0) \quad (2.41d)$$

where V_{IN} is the input voltage at port 1, and Z_{La} and Z_{Lb} are the load impedances on conductor a and b.

Substituting Eq.(2.40) to (2.41), we have a linear equation for A_i

$$\mathbf{D} \begin{bmatrix} A_1 & A_2 & A_3 & A_4 \end{bmatrix}^T = \begin{bmatrix} V_{\text{IN}} & 0 & 0 & 0 \end{bmatrix}^T, \quad (2.42)$$

where

$$\mathbf{D} = \begin{bmatrix} (1 + \frac{Z_{La}}{Z_c})e^{j\beta_c l} & (1 - \frac{Z_{La}}{Z_c})e^{-j\beta_c l} & (1 + \frac{Z_{La}}{Z_\pi})e^{j\beta_\pi l} & (1 - \frac{Z_{La}}{Z_\pi})e^{-j\beta_\pi l} \\ R_c(1 + \frac{Z_{Lb}}{Z_c})e^{j\beta_c l} & R_c(1 - \frac{Z_{Lb}}{Z_c})e^{-j\beta_c l} & R_\pi(1 + \frac{Z_{Lb}}{Z_\pi})e^{j\beta_\pi l} & R_\pi(1 - \frac{Z_{Lb}}{Z_\pi})e^{-j\beta_\pi l} \\ 1 - \frac{Z_{La}}{Z_c} & 1 + \frac{Z_{La}}{Z_c} & 1 - \frac{Z_{La}}{Z_\pi} & 1 + \frac{Z_{La}}{Z_\pi} \\ R_c(1 - \frac{Z_{Lb}}{Z_c}) & R_c(1 + \frac{Z_{Lb}}{Z_c}) & R_\pi(1 - \frac{Z_{Lb}}{Z_\pi}) & R_\pi(1 + \frac{Z_{Lb}}{Z_\pi}) \end{bmatrix} \quad (2.43)$$

Once A_i are solved from this linear equation, the S-parameters can be obtained.

Here, we define S-parameters as the voltage ratios between the reflected/through/forward-coupled/backward-coupled waves to the input voltage. This definition works for the case where the coupler is symmetric, and all load impedances are equal. In the case of asymmetric lines and unequal loads, defining S-parameters in terms of power may be more proper. In practice, all the lines will be later matched to $50\ \Omega$, so confusion can be avoided in actual experiments.

Note that our boundary conditions determine that the input wave only has voltage of $V_{\text{IN}}/2$ (in the case of impedance-matched launching). Therefore, the S-parameters are $S_{11} = (V_a(-l) - V_{\text{IN}}/2)/(V_{\text{IN}}/2)$, $S_{21} = V_b(-l)/(V_{\text{IN}}/2)$, $S_{31} = V_a(0)/(V_{\text{IN}}/2)$, and $S_{41} = V_b(0)/(V_{\text{IN}}/2)$.

Figure 2-13 shows the calculated S-parameters in a $367\ \mu\text{m}$ -long symmetric microstrip coupler (using the structure in Fig. 2-10), designed to be 3 dB forward coupling at 10 GHz. The width of the microstrip is 300 nm, and the gap between them is 500 nm. We assume that each wire is loaded with their uncoupled characteristic impedance. Table 2.1 summarizes the mode indices and impedances (simulated from mode solver in COMSOL) and estimated distributed circuit parameters (calculated from β 's and Z 's). We noticed that \mathcal{M} is small and sensitive to simulation errors, but it is much smaller than \mathcal{L} and thus does not affect the calculated S-parameters.

Table 2.1: Mode indices, impedances, and distributed circuit parameters of a symmetric nanowire microstrip coupler.

β_0	β_c	β_π	Z_0	Z_c	Z_π
$65.5\ k_0$	$56.2\ k_0$	$83.7\ k_0$	$1221\ \Omega$	$1426\ \Omega$	$956\ \Omega$
\mathcal{L}	\mathcal{C}_0	$\mathcal{C}_{\text{fringe}}$	\mathcal{E}	\mathcal{M}	
$212.3\mu_0$	$20.2\epsilon_0$	$5.4\epsilon_0$	$9.1\epsilon_0$	$-0.10\ \mu_0$	

Tuning the coupling with DC bias current. Since \mathcal{L}_k can be tuned by using a bias current (either DC or low frequency AC signals, see Eq. (2.9)), it is possible to tune the coupling of the nanowire coupler using DC bias current like a microwave switch, or modulate the transmission of one transmission line through the neighboring wire.

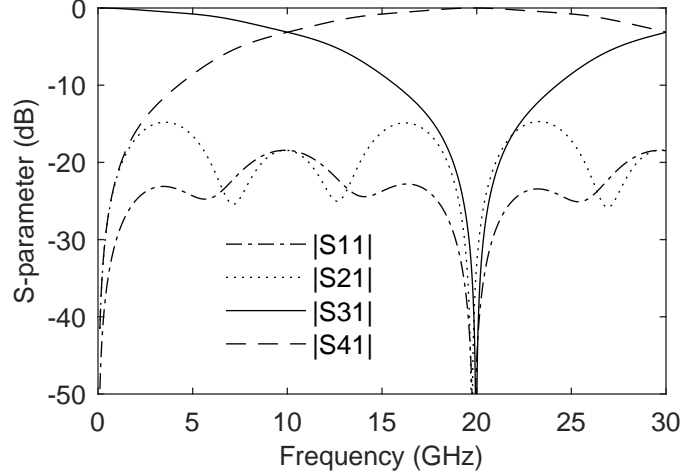


Figure 2-13: Calculated S-parameters for nanowire coupler. $w = 300$ nm, $g = 300$ nm, $l_{\pi/2} = 271\mu\text{m}$.

For example, if we drive a carrier tone at 10 GHz in transmission line a , then add a DC bias current into transmission line b , the transmitted signal in transmission line a will be modulated. Figure 2-14 shows the simulated transmission ($|S_{31}|$) as a function of normalized bias current to depairing current (I_b/I_d) with different coupler lengths (assuming $\mathcal{L}_{\text{kb}}(I_b) = \mathcal{L}_{\text{kb}}(0)[1 - (I_b/I_d)^{2.21}]^{-2.21}$). With increasing coupling length, the modulation will become more and more sensitive, and eventually reach full oscillations.

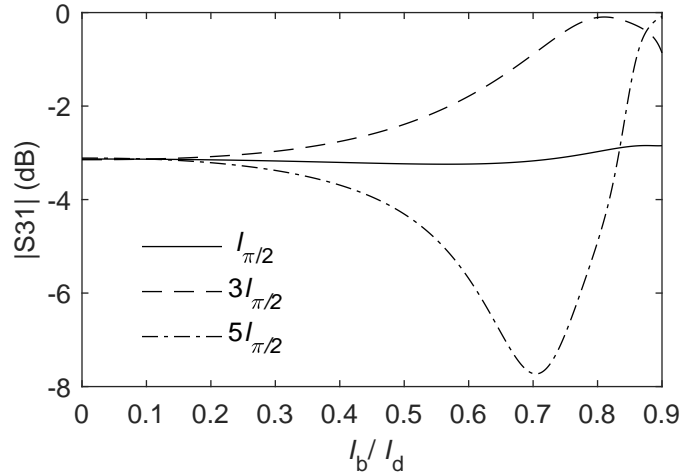


Figure 2-14: Modulating nanowire coupler with DC bias current. Couplers with 3 different lengths are calculated. To increase modulation sensitivity, longer coupling length is needed.

2.6 Impedance-matching taper

Kinetic-inductive nanowire transmission lines have characteristic impedances in the $k\Omega$ range. However, conventional RF components and coaxial cables are all at $50\ \Omega$. Impedance matching is essential to interface the two.

In this thesis, we use Klopfenstein tapers extensively. A Klopfenstein taper is a high-pass impedance transformer. It is often called an “optimal” taper, because, given a required pass-band cutoff and maximum reflection, it requires minimum length. Recently, in Ref. [68], Erickson pointed out that Klopfenstein is not ideal and not optimal, especially for applications that require extremely low reflection, such as traveling-wave parametric amplifier [42], because it has relatively large non-rolling-off reflection ripples in the passband [68]. However, for impedance-matched readout of nanowire detectors, and interfacing delay-line-multiplexed detector arrays, moderate reflection (≈ -20 dB) is acceptable. Instead, we care more about device footprint and prefer to achieve the desired bandwidth with the shortest taper length, because our nanowire transmission line and tapers are all written using electron-beam lithography.

The governing equation of the impedance taper is the Ricatti differential equation from Walker and Wax [69]

$$\frac{d\rho(x)}{dx} - 2\gamma(x)\rho(x) + \frac{1}{2}(1 - \rho(x)^2)\frac{d \ln Z(x)}{dx} = 0, \quad (2.44)$$

and in the literature, the design of impedance transformer centers around looking for proper solutions of its linearized form [70, 68, 51]

$$\frac{d\rho(x)}{dx} - 2\gamma(x)\rho(x) + \frac{1}{2}\frac{d \ln Z(x)}{dx} = 0; \text{ assuming } \rho(x)^2 \ll 1 \quad (2.45)$$

where $\rho(x)$ is the reflection coefficient at any point x along the taper, $\gamma(x) = j\beta(x)$ (for lossless transmission line) and $Z(x)$ are the propagation constant and characteristic impedance of the transmission line along the taper. $\rho(x)^2 \ll 1$ can be satisfied if the taper is smooth (adiabatic).

Usually, the taper profiles are derived assuming the same propagation constant

($\gamma(x) = j\beta$) for all $Z(x)$. This assumption is valid for pure TEM transmission lines (such as that in Fig. 2-4), but not in the kinetic-inductive transmission lines, where the change of Z always comes with a change of β . One trick is to divide the “constant”- β taper into many sections and scale their length according to the actual effective indices at each characteristic impedance.

Klopfenstein taper. Klopfenstein taper has the impedance profile [70, 51]

$$Z(x) = \sqrt{Z_1 Z_2} \exp \left[\Gamma_m A \int_0^{2x/l-1} \frac{I_1(A\sqrt{1-y^2})}{\sqrt{1-y^2}} dy \right], \quad (2.46)$$

where l is the length of the taper, Z_1 and Z_2 are the impedances to be matched (Z_1 at $x = 0$ and Z_2 at $x = l$), I_1 is the modified Bessel function of the first kind, Γ_m is the maximum reflection ripple in the passband, and A is a design parameter that links Γ_m to the unmatched reflection $\Gamma_0 = \frac{1}{2} \ln Z_2/Z_1$ with $\cosh A = \Gamma_0/\Gamma_m$.

The design frequency (lower cutoff, $f_{co} = c/\lambda_{co}$) and band-ripple parameter A determine the electrical length of the taper as $l = \frac{A}{2\pi} \lambda_{co}$. The physical length l_{physical} has to be scaled by the phase velocity of each taper section.

Figure 2-15 shows an example of a Klopfenstein taper profile. The taper is designed to have a cut-off frequency of 500 MHz, and a maximum passband reflection ripple of ≈ -20 dB. In Fig. 2-15(a), the main panel shows $Z(x)$ as a function of electrical length, while the inset shows $Z(x)$ as a function of the physical length when the taper is implemented using a SCPW studied in Fig. 2-9. Each taper section is shrunk according to their actual effective index, and the total physical length is 2.8% of the electrical length ($\approx 4.8\%$ of the cut-off wavelength in free space λ_0). Figure 2-9 shows the center conductor width of the SCPW for the taper.

In principle, the unmatched reflection coefficient should be $\Gamma_0 = \frac{Z_2 - Z_1}{Z_2 + Z_1}$, but using this expression will generate large discontinuities (as much as 900 Ω at the high impedance end with a 50 Ω to 1.5 k Ω taper) at the two ends of the taper. Instead, it is taken as $\Gamma_0 = \frac{1}{2} \ln(Z_2/Z_1)$ in [70]. This approximation is good when Z_1 and Z_2 are close (e.g., when $Z_1 = 50 \Omega$ and $Z_2 = 100 \Omega$, $\frac{Z_2 - Z_1}{Z_2 + Z_1} = 0.33$ and $\frac{1}{2} \ln(Z_2/Z_1) = 0.34$), but not when they are significantly different (e.g., when $Z_1 = 50 \Omega$ and $Z_2 = 1500 \Omega$,

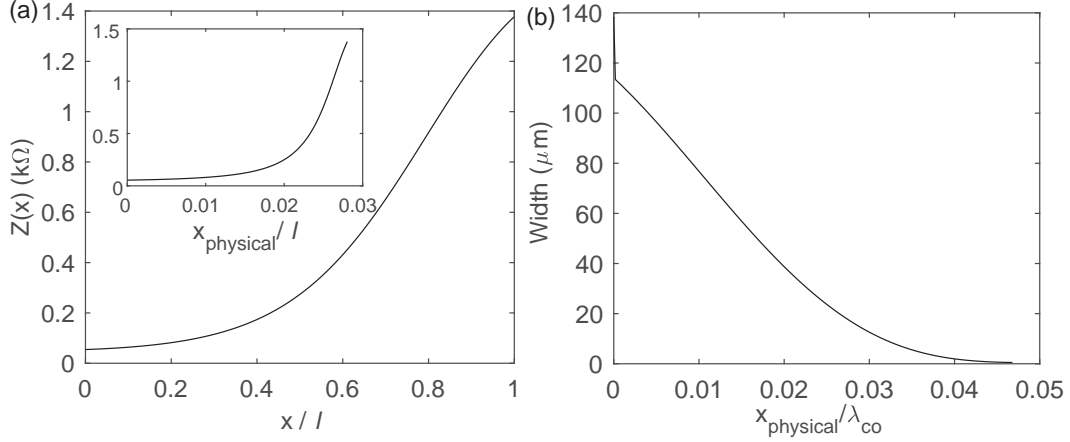


Figure 2-15: Klopfenstein taper profile. (a) Main panel shows the calculated impedance profile using Eq. (2.46), which assumes a constant propagation constant $\beta = k_0$ for all impedances ($l = \lambda_{\text{co}} \frac{A}{2\pi}$, $A = \cosh^{-1} 20 = 3.688$, $Z_1 = 50 \Omega$, $Z_2 = 1.5 \text{ k}\Omega$). Inset shows the impedance profile of an actual taper (implemented using a 3- μm -gap CPW in Fig. 2-9), where each section is shrunk according to their actual effective index. (b) Profile of SCPW center conductor width. The actual length of the taper is $< 5\%$ of the cut-off wavelength in free space λ_0 .

$\frac{Z_2 - Z_1}{Z_2 + Z_1} = 0.94$ but $\frac{1}{2} \ln(Z_2/Z_1) = 1.70$). In the actual design, we still use $\Gamma_0 = \frac{1}{2} \ln(Z_2/Z_1)$ to avoid the large discontinuities at the ends, but approximating the input reflection coefficient as $\Gamma_m e^{-j\beta l} \cos \sqrt{(\beta l)^2 - A^2}$ from Klopfenstein[70] or Pozar[51] will become inaccurate; instead, it should be rigorously calculated by integrating the original nonlinear Riccati differential equation in Eq. (2.44) [69]. The difference can be seen in Fig. 2-16, where reflections calculated from nonlinear Riccati, linear Riccati, and Klopfenstein's formula (derived from linear Riccati) are compared.

$2N$ -degree polynomial taper derived from variational theory. Recently, Erickson presented a variational theory of optimal tapered impedance transformer with proper boundary conditions [68]. A $2N$ -degree polynomial taper is derived under this theory as an alternative to the Klopfenstein taper. Its impedance profile follows

$$Z_{\text{poly}}(x, N) = Z_2 \exp[\ln(Z_1/Z_2)I(1 - x/l; N + 1, N + 1)], \quad (2.47)$$

where $I(z; N + 1, N + 1) = \frac{(2N+1)!}{(N!)^2} \int_0^z (u - u^2)^N du$ is a regularized incomplete beta function.

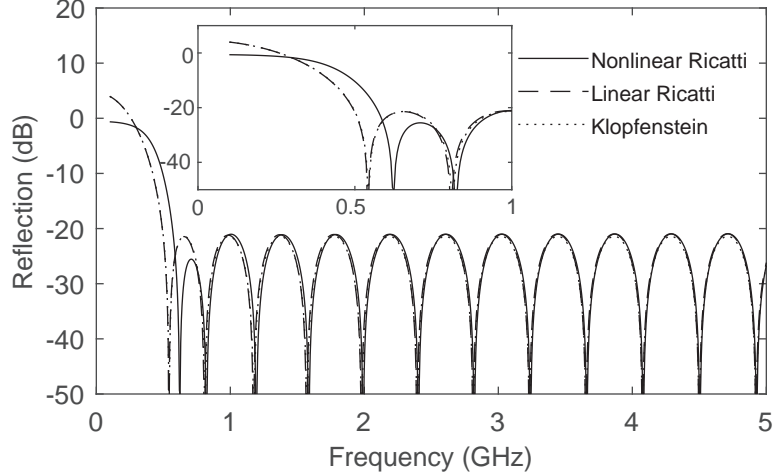


Figure 2-16: Reflection from Klopfenstein taper in Fig. 2-15. Note that the line reflections calculated from Klopfenstein's original expression and linear Ricatti equation perfectly overlap, but they deviate from non-linear Ricatti equation, because $\rho^2 \ll 1$ is not valid in the low-frequency stop band for largely mismatched load.

Figure 2-17(a) compares the impedance profile of polynomial and Klopfenstein tapers with the same electrical length ($l = \lambda_{\text{co}} \frac{A}{2\pi} = \frac{c}{500 \text{ MHz}} \frac{3.688}{2\pi} = 350 \text{ mm}$, $Z_1 = 50 \Omega$, $Z_2 = 1.5 \text{ k}\Omega$). The inset shows the impedance profile in terms of physical length (implemented using a SCPW in Fig. 2-9), where each taper section is shrunk according to their actual effective index. Figure 2-17(b) shows the input reflection of each taper calculated from the nonlinear Ricatti equation (Eq. 2.44).

The polynomial tapers eliminate some undesirable features of the Klopfenstein taper, including the discontinuity at the ends and non-rolling-off reflection ripple in the passband. However, the fast reflection roll-off of the polynomial taper comes with increased passband cut-off. So the choice depends on the specific applications. For SNSPD readout, where high-frequency reflection does not matter, Klopfenstein taper may be more suitable because of its shorter length (i.e., shorter writing time and smaller inductance) given a particular cut-off frequency. For other microwave devices that require extremely low reflections, such as traveling-wave parametric amplifiers, microwave couplers, superconducting qubit readout lines, the polynomial taper is more desirable.

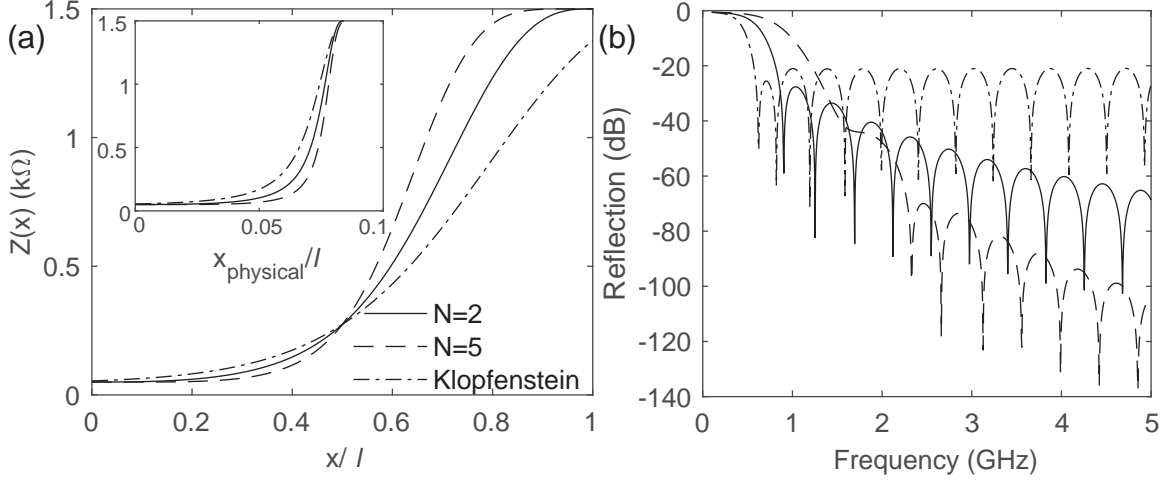


Figure 2-17: Comparing $2N$ -degree polynomial taper and Klopfenstein taper with the same length. (a) Impedance profile of Erickson’s polynomial tapers and Klopfenstein taper. Inset: Physical impedance profile when the taper is shrunk according to the actual effective index at each $Z(x)$ (implemented with CPW in Fig. 2-9). The polynomial tapers do not have discontinuity at the ends. (b) Input reflections for each taper. The band ripples roll down faster for polynomial tapers, but their cut-off frequencies are larger than the Klopfenstein taper. $l = \lambda_{\text{co}} \frac{A}{2\pi} = \frac{c}{500 \text{ MHz}} \frac{3.688}{2\pi} = 350 \text{ mm}$. $N = 2$ and $N = 5$ polynomial tapers are generated using Eq. (2.47), and Klopfenstein taper is generated using Eq. (2.46). Reflections for both are calculated the original nonlinear Ricatti equation.

2.7 Conclusion

In summary, kinetic inductance plays a central role in waveguides and transmission lines made from thin-film type-II superconductors. Superconducting nanowire transmission lines geometrically push the kinetic inductance contribution to an extreme level ($\text{nH}/\mu\text{m}$), resulting in $k\Omega$ characteristic impedance and phase velocity of two orders of magnitude slower than the speed of light in free space. We showed an example of a nanowire-based microwave coupler and illustrated its tunability by using the nonlinear kinetic inductance. We briefly reviewed the basics of impedance-matching taper and discussed the specifics on how to implement them using kinetic inductive transmission lines.

Chapter 3

SNSPD with integrated impedance-matching taper

Conventional readout of SNSPD connects the nanowire directly to a $50\ \Omega$ load. However, SNSPDs are intrinsically high-impedance—both the hotspot resistance and characteristic impedance are at the $\text{k}\Omega$ range. Using a high-impedance source to drive a low impedance load is inefficient. In this chapter, we present an impedance-matched readout method by integrating the SNSPD with an integrated transmission line taper. This readout method increases the amplitude of detector pulses without sacrificing their fast rising edge, which in turn reduces the electrical timing jitter.

Part of the material presented in this chapter has been published and is reproduced from *Appl. Phys. Lett.* **114**, 042601 (2019) [71].

3.1 Introduction

A common problem with SNSPDs is their low output voltage and signal-to-noise ratio (SNR), which has been a limiting factor in detector's timing jitter [8]. A simple lumped-circuit model dictates that the output voltage from the nanowire cannot exceed $I_B \times Z_{\text{load}}$, where I_B is the bias current and Z_{load} is the load impedance [72]. I_B is limited by the nanowire's switching current at the μA range. Z_{load} is set by the input impedance of the coaxial cable and RF electronics, which is conventionally

50 Ω . To improve readout SNR, significant progress has been made on developing cryogenic amplifiers with low noise, dissipation and cost, e.g. using silicon germanium and gallium arsenide transistors [73, 74, 75, 76]. Digital readout circuits built directly from superconducting electronics, such as nanocryotrons [77] and single flux quantum (SFQ) circuits [78, 79], have also been demonstrated. These integrated superconducting circuits are low-noise and scalable, but usually require additional biasing and suffer from leakage current and crosstalk.

An alternative approach to increase the output signal is to increase Z_{load} . Compared to a standard 50 Ω load, a high-impedance load is often more desirable—it not only increases the detector output, but also enables direct mapping of hotspot resistance and photon number/energy resolution [80, 81, 82]. However, high-impedance loading is difficult to achieve in practice. The lack of high-impedance coaxial cables makes it necessary to place the high-impedance amplifiers close to the detectors (at the low-temperature stage), which imposes a more stringent power budget. More importantly, even if a high-impedance amplifier is available [75], loading a standard SNSPD directly with high impedance can lead to latching [83].

In this work, without using high-impedance cryogenic amplifiers or any active circuit elements, we break the $I_B \times 50 \Omega$ limit with an impedance transformer. The transformer is an integrated superconducting transmission line taper, which gradually reduces its characteristic impedance from k Ω to 50 Ω . It effectively loads the SNSPD with a k Ω impedance without latching. We designed the taper to be a co-planar waveguide (CPW) and fabricated it on the same superconducting thin film as the SNSPD. Using a taper with a starting width of 500 nm and nominal passband from 116 MHz, we experimentally observed $3.57 \times$ higher output voltage and no added noise compared to the non-tapered reference device. This voltage gain is equivalent to a 11 dB passive, dissipation-free cryogenic amplifier. Despite its large DC inductance, the taper preserves the detector’s fast rising edge, resulting in an increased slew rate and reduced timing jitter (from 48.9 ps to 23.8 ps). The integrated impedance taper demonstrated here is useful for interfacing high-impedance nanowire-based devices to conventional low-impedance components, such as memory, and electrical or optical

modulators.

3.2 Concept of tapered readout

To understand how impedance matching taper amplifies SNSPD output voltage, it is useful to review the standard lumped-element circuit model. Figure 3-1(a) shows a circuit model of a conventional SNSPD readout circuit, where the detector is modeled as a kinetic inductor L_K in series with a time-dependent variable resistor R_N . When an incident photon triggers the detector, R_N switches from 0 to $\approx k\Omega$ within ≈ 100 s of ps and diverts the bias current to the load. The evolution of R_N is determined by the non-linear electrothermal feedback in the detector [6, 83]. The currents from the bias source (I_B), in the nanowire (I_D), and to the load (I_L) simply follow Kirchhoff's law $I_L = I_B - I_D$. The maximum I_L is therefore limited to I_B , corresponding to the case where R_N pushes out all the current in the nanowire ($I_D = 0$). The output voltage on the load thus can not exceed $I_B \times 50 \Omega$. In practice, due to the electrothermal feedback [83], I_D usually has some remanding value, which depends on the bias current, kinetic inductance, and thermal constants of the materials.

Figure 3-1(b) shows a simplified circuit diagram for the tapered readout. The taper is inserted between the SNSPD and load, with a low impedance $Z_L = 50 \Omega$ on the load end and a high impedance Z_H on the detector end. In our implementation, the taper consists of a continuous nanowire transmission line without any dissipative elements. The taper is high-pass—it works as a transformer at high frequency but acts as an inductor at low frequency. When an incident photon triggers the SNSPD, R_N switches on and pushes the current away from the nanowire. Instead of diverting the current directly to the 50Ω load as in the conventional readout, the SNSPD injects current to the taper at Z_H . As the electrical pulse travels towards the low impedance end, its current amplitude increases while the voltage amplitude drops, with a ratio that satisfies the change of impedance (Fig. 3-1(c)). Assuming an ideal broadband transformer with perfect impedance matching and power transmission, the current leaving the low-impedance end (to the load) ΔI_{DL} is related to the current injected to

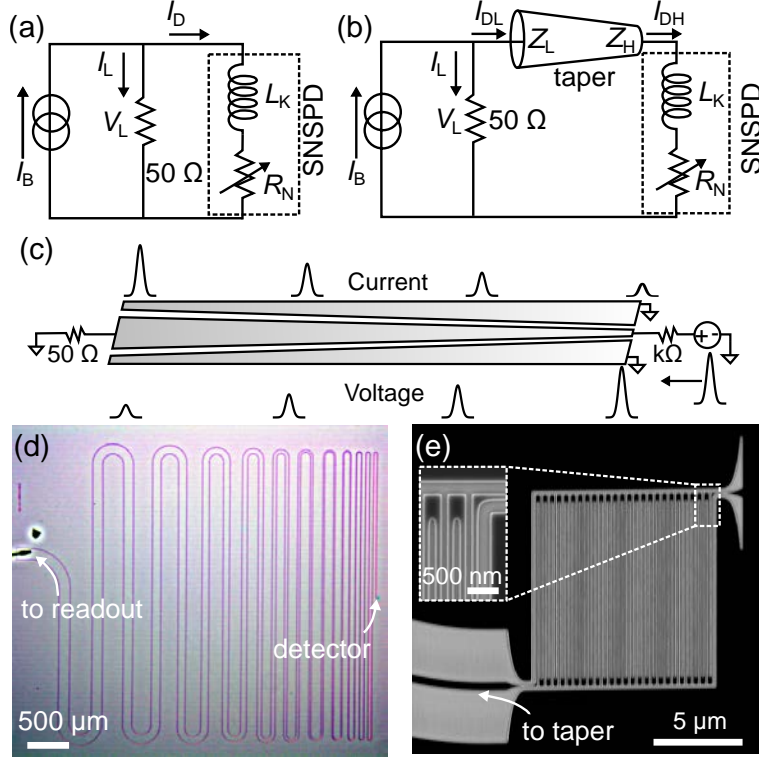


Figure 3-1: Circuit diagram and micrographs of the tapered SNSPD readout. (a) A circuit diagram of a conventional SNSPD readout. (b) A circuit diagram of a tapered readout. The taper loads the SNSPD with high impedance while interfacing at its other end to the readout electronics at $50\ \Omega$, resulting in a larger output voltage. (c) Schematic diagram of a co-planar waveguide transmission line taper. When an electrical pulse is launched from the high-impedance end, its voltage drops but current increases while traveling towards the low-impedance end. (d) An optical micrograph of the integrated transmission line taper. Light area: NbN; red outlines: substrate. (e) A scanning electron micrograph of the SNSPD. Dark area: NbN; light area: substrate.

the high-impedance end ΔI_{DH} by $\Delta I_{DL}^2 Z_L = \Delta I_{DH}^2 Z_H$. In our transmission line taper, this relation is valid only at high frequency (passband of the taper), which dominates the rising edge of the detector pulse. In the extreme case where the SNSPD pushes all the bias current out, i.e., $\Delta I_H = I_B$, the current diverted to the load can be as large as $I_L = \Delta I_{DL} = I_B \sqrt{\frac{Z_H}{Z_L}}$, corresponding to an output voltage of $V_L^{\text{taper}} = I_B \times 50\ \Omega \sqrt{\frac{Z_H}{Z_L}}$ and an effective voltage gain of $\sqrt{\frac{Z_H}{Z_L}}$ with respect to the conventional readout. In practice, when terminated with the high-impedance taper, the SNSPD latches, leaving the residual current at the hotspot current I_{ss} , then resets through reflection from the

taper. As we will show later, the actual effective voltage gain is always less than $\sqrt{\frac{Z_H}{Z_L}}$ due to the electro-thermal feedback and limited taper bandwidth.

3.3 Design and fabrication

Figure 3-4(d) shows an optical micrograph of a fabricated SNSPD with a meandered transmission-line taper. The bright area is NbN, and the red area is the substrate, where the NbN was etched away. The NbN was sputtered at room temperature on a silicon substrate with a 300 nm thick thermal oxide layer [84]. The film had a critical temperature of 8.1 K and room-temperature sheet resistance of $342 \Omega/\text{sq}$. The sheet inductance was estimated to be $80 \text{ pH}/\text{sq}$ by fitting the falling edge of the output pulse from a reference detector. The nanowire fabrication process is described in Ref. [40, 8]. The taper was made from a CPW with a fixed gap size of $3 \mu\text{m}$, and a varying center conductor width from $135 \mu\text{m}$ (50Ω) to 500 nm ($1.7 \text{ k}\Omega$). Its left/wide end is wire bonded to external circuit board, and the right/narrow end connects to the SNSPD with through a $1 \mu\text{m}$ -long hyperbolic taper. The SNSPD was 100 nm wide, densely packed with a 50% fill factor, and spanned a rectangular area of $11 \mu\text{m} \times 10 \mu\text{m}$ (see Fig. 3-1(e)). A 200 nm gap surrounded the detector region to reduce proximity effect in fabrication. On the same chip, we also fabricated non-tapered detectors as references.

The taper was designed to be a 5672-section cascaded transformer with a lower cut-off frequency of 116 MHz and a total electrical length of 1.5 m^1 , following the Klopfenstein profile [70]. The physical length was 77.9 mm due to the slow phase velocity of the superconducting transmission line, and the total inductance was $1.4 \mu\text{H}$ (see SI for the simulated S parameters). This length was chosen so that the maximum reflection in the passband would not exceed -20 dB. The total electrical length is calculated as $l_e = Ac/2\pi f_{co}$, where f_{co} is the nominal cut-off frequency

¹In the original paper [71], we reported the nominal cut-off frequency to be 200 MHz and electrical length to be 851 mm. We later realized that the actual cut-off frequency was 116 MHz and electrical length was 1.5 m . This error was due to the missing factor $A/2\pi (= 0.58)$ in the Matlab code that generated the taper profile. Physical length and taper inductance were correct. In fact, the discrepancy was captured by the SPICE simulation in the supplementary Fig.S2.

and c is the speed of light in vacuum. A is a factor that determines the maximum reflection in the passband and is calculated as $\cosh(A) = \rho_0/\rho_{\text{pb}}$, where ρ_0 is the initial reflection coefficient (i.e., without taper) and ρ_{pb} is the maximum passband reflection coefficient (taken as 0.1 here). For design convenience, we followed Klopfenstein’s original approach and took $\rho_0 = 0.5 \ln(Z_{\text{H}}/Z_{\text{L}})$ instead of $(Z_{\text{H}} - Z_{\text{L}})/(Z_{\text{H}} + Z_{\text{L}})$ [70].

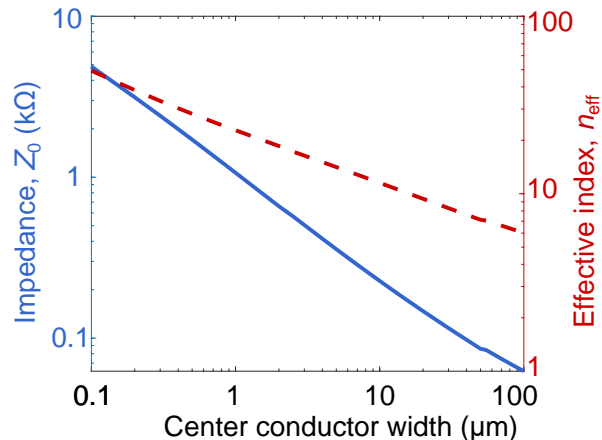


Figure 3-2: Characteristic impedance (Z_0) and effective index (n_{eff}) of the superconducting NbN coplanar waveguide simulated using Sonnet (a commercial software for high-frequency RF/microwave analysis). The gap size of the coplanar waveguide is fixed at 3 μm , and the NbN film has a sheet kinetic inductance of 80 pH/sq. The substrate is 300 nm SiO_2 on 500 μm intrinsic Si.

3.4 Device measurement

The detectors were measured at 1.3 K in a cryogen-free continuous-flow cryostat (ICE Oxford). Both the bias circuit and readout electronics were at room temperature. The output signal of the detectors were amplified using a 2.5 GHz, 25 dB gain low-noise amplifier (RF BAY LNA-2500), and a 3 dB attenuator was inserted before the amplifier to reduce reflection and prevent latching. The output pulses from the amplifier were then acquired by a 6 GHz real-time oscilloscope (Lecroy 760Zi). The detector chip was flood illuminated using attenuated sub-ps pulsed lasers at 1550 nm (FPL-02CCF) through an optical fiber (SMF-28e). The laser pulses were split into two

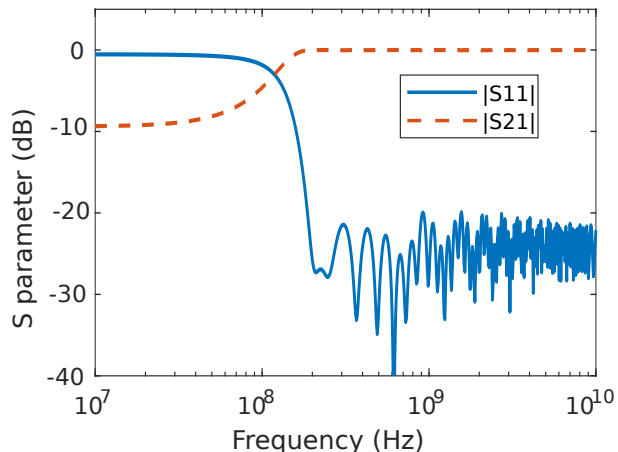


Figure 3-3: SPICE simulated S-parameter of the impedance taper. In the simulation, the taper is discretized and down-sampled to 300 sections, and each section is implemented using the LTRA model in LTspice. The taper is terminated with impedance matched resistive load on both ends.

arms, one to a variable attenuator then to the cryostat, and the other to a fast photodiode (Thorlabs DET08CFC) as timing references. Since the distance between the non-tapered detector and tapered detector (≈ 5 mm) was much less than the distance between the detector chip and fiber tip (≈ 10 cm), we expect the difference in photon arrival time to be < 1 ps. Both the tapered and non-tapered detectors had a switching current of $30 \mu\text{A}$, and were biased at $27.5 \mu\text{A}$ throughout the measurement.

3.5 Increasing output voltage

Figure 3-4(a) shows the measured pulse shapes from the reference and tapered detectors. The amplifier gain was removed to better compare with simulations. To avoid phase distortion in reconstructing the unamplified pulses, we used a weighted gain, $\bar{G} = \int df PSD(f)G(f) / \int df PSD(f)$, where $PSD(f)$ is the power spectral density of the pulse, and $G(f)$ is the measured system gain spectrum (see SI for details). \bar{G} was calculated to be 20.5 dB. As shown in Fig. 3-4(a), we observed a voltage gain of 3.6 and an extra delay of 2.8 ns from the tapered device compared to the reference device (by aligning the electrical pulses to the optical references). This voltage enhancement is equivalent to a passive, noise-free 11 dB amplifier.

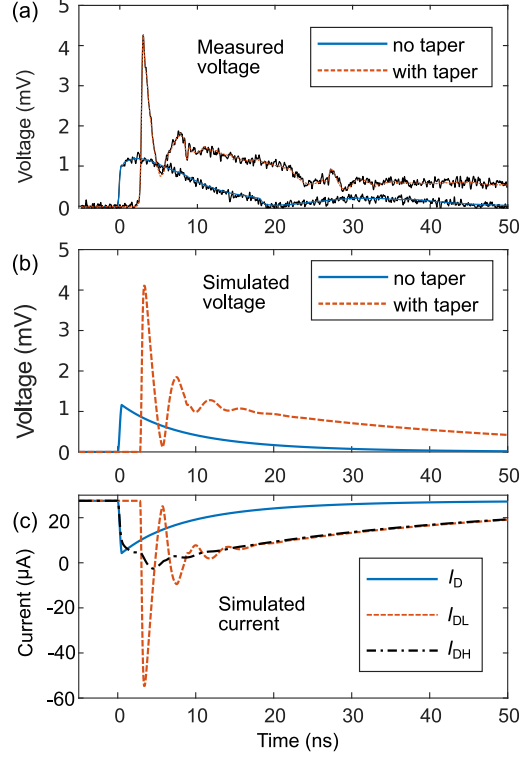


Figure 3-4: Measured detector pulses and comparison with SPICE simulation. (a) Measured voltage with amplifier gain and cable losses removed, i.e., raw output from the detector. The black traces are single-shot waveforms, and the superimposed colored lines are averaged waveforms. (b) Simulated output voltages for both the tapered and non-tapered detectors. (c) Simulated current distributions. I_D is the current in the SNSPD for a non-tapered readout. I_{DL} and I_{DH} are the currents on the low-impedance and high-impedance ends of the tapers in the tapered detector, respectively.

We simulated the tapered detector using a SPICE model that incorporates both the hotspot dynamics in the SNSPD and the distributed nature of the transmission line taper [85, 86]. The simulation was implemented in LTspice, a free electrical circuit modeling software. The SPICE model for SNSPD was developed by Berggren et al.[85] based on the phenomenological hotspot velocity model by Kerman et al.[83] The taper was simulated as cascaded lossless transmission lines (down-sampled to 300 sections) [86], and each section was implemented using the LTRA model in LTspice with different length, inductance, and capacitance settings.

Figure 3-4(b) plots the simulated load voltages, showing a voltage gain of 3.5 and a delay of 2.8 ns, as compared to the measured gain of 3.6 and delay of 2.8 ns.

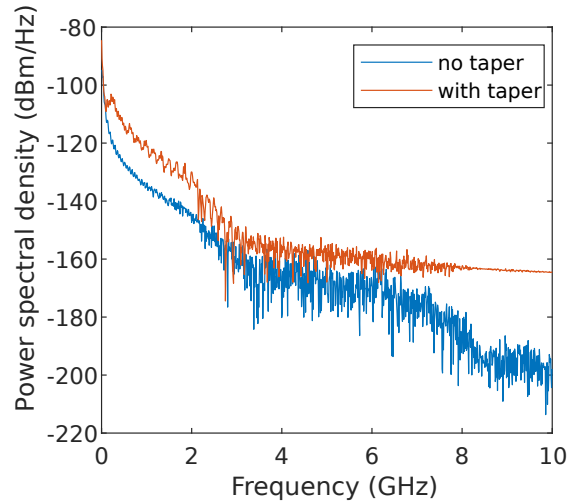


Figure 3-5: Power spectral density of the output pulses from tapered and reference detectors. The power spectral density was calculated by taking the Fourier transform of the averaged detector pulses acquired on the oscilloscope. The detector pulses were amplified through a 2.5 GHz amplifier. The sampling rate was 40 GS/s and the bandwidth was 3 GHz.

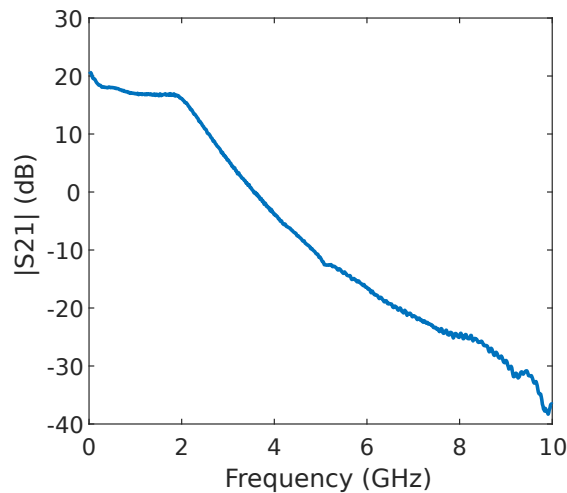


Figure 3-6: System gain characterization. The transmission coefficient (S_{21}) was measured using a vector network analyzer (Keysight N5224A) from the device under test up to the input port of the oscilloscope, including the cryocable, bias Tee, 3 dB attenuator, and low noise amplifier (LNA2500).

The subsequent peaks in the output voltage are spaced by ≈ 4.2 ns, which should correspond to the round trip time in the taper. The single-trip delay of the taper calculated from the reflection peaks (2.1 ns) is shorter than the delay between the

tapered detector and reference detector (2.82 ns), because the hotspot grows longer and larger in the tapered detector, as can be seen in the simulated currents.

Figure 3-4(c) shows the simulated currents. For the tapered detector, the current in the nanowire (I_{DH}) first drops at a similar rate as the non-tapered case (I_{D}), then enters an intermediate plateau due to latching [83]. Similar current plateau and latching behavior are often observed when loading an SNSPD with a $\text{k}\Omega$ resistor. However, at ≈ 4.6 ns, I_{DL} drops again and kicks the detector out of the latching state. The drop in current is from the reflection in the transmission line taper. Alternatively, it can be understood as that the distributed capacitors in the transmission line draw current from the SNSPD. After a few oscillations (high frequency), the current in the detector recovers with an $\tau = L/R$ exponential time constant (low frequency). Here, L is the total inductance of the SNSPD and the taper (at low frequency, the taper behaves as an inductor), and R is 50Ω . The extra inductance from the taper results in a longer τ of 39 ns. The simulated currents at the high- and low-impedance ends of the taper follow our intuitive understanding on how a transformer works.

In Fig. 3-7, we study the trade-off between the gain factor and taper's impedance, bandwidth, and inductance. In general, higher input impedance and lower cut-off frequency produce higher output voltages but comes with longer taper, large inductance, and hence slower reset.

3.6 Increasing slew rate and reducing timing jitter

The impedance taper amplifies the output pulse amplitude without sacrificing the fast rising edge, resulting in a faster slew rate. Figure 3-9(a) compares the averaged rising edges of the detector pulses from the reference and tapered detectors (with amplifier gain). The sampling rate was 40 GS/s. As shown in Fig. 3-9(b), the maximum slew rates (dV/dt) were $39 \mu\text{V}/\text{ps}$ for the reference detector, but $143 \mu\text{V}/\text{ps}$ (3.7 times faster) for the tapered detector.

The slew rate directly impacts the electrical noise's contribution on the timing jitter, usually referred as noise jitter, σ_{noise} [87]. We sampled the background electrical

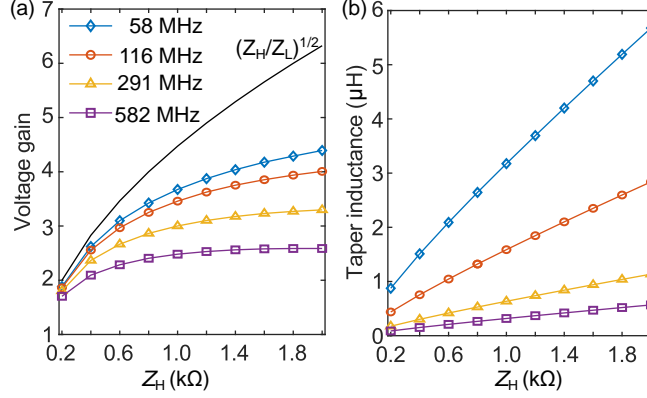


Figure 3-7: Simulated gain factor (the ratio between the maximum voltages of tapered and non-tapered detector) and taper inductance as a function of the starting input impedance (Z_H) under different nominal cut-off frequencies. Higher input impedance and smaller cut-off frequencies produce higher output voltages (a), but result in larger inductance (b), and hence longer rest time. The simulated non-tapered SNSPD has a bias current of $27.5 \mu\text{A}$, an inductance of 414 nH , and a maximum output voltage of 1.1 mV ($84\%I_B \times 50 \Omega$). Each simulated taper has 300 sections and the electrical length is designed to be $l_e = \text{arccosh}(\rho_0/\rho_{\text{pb}})c/2\pi f_{\text{co}}$, where $\rho_0 = 0.5 \ln(Z_H/Z_L)$, and $\rho_{\text{pb}}=0.1$, as described in the main text. Z_L is set to 50Ω . This figure is adapted from supplementary Fig.S8 in Ref [71]. As explained in Section 3.3, the taper cut-off frequency was overstated by a factor of $A/2\pi = 0.58$ in the original paper, and is now corrected here. Inductances, gains, and impedances were correct.

noise on the oscilloscope for both detectors by measuring the voltage at 400 ps before the rising edge of the pulses. The noise followed a Gaussian distribution and had a standard deviation of $559 \mu\text{V}$ and $547 \mu\text{V}$ for the reference and tapered detector, respectively (Fig. 3-8). Taking their respective fastest slew rates, we calculated that the reference detector would have σ_{noise} of 14.3 ps , and the tapered detector would have an σ_{noise} of 3.8 ps .

We measured the jitter of the detectors following the procedure described in Ref. [88]. The discrimination levels for time tagging were set to voltages with the fastest slew rates. Figure 3-9(c) shows the instrument response function (IRF) of the reference and tapered detectors at 1550 nm illumination wavelength. With the impedance taper, the full-width half-maximum (FWHM) jitter reduced from 48.9 ps to 23.8 ps . We fitted the IRF using an exponentially modified Gaussian distribution [8], and found $\sigma = 16.8 \text{ ps}$ and $1/\lambda = 17.4 \text{ ps}$ for the reference detector, and

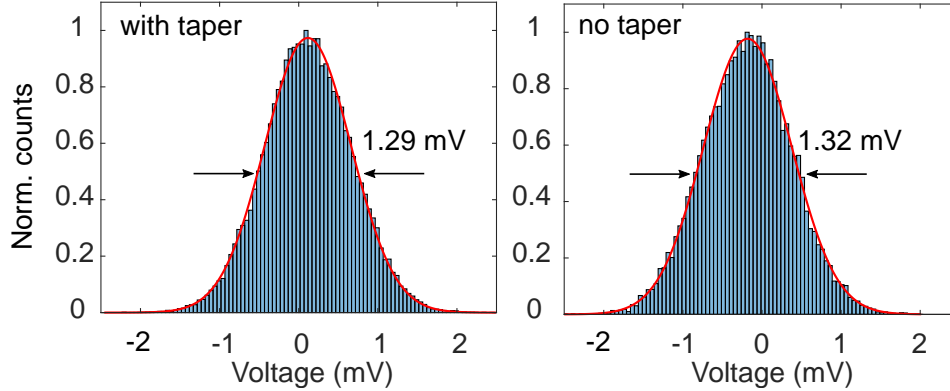


Figure 3-8: Measured noise floor from the tapered and non-tapered device. Compared to the reference detector, no added noise was observed from the tapered device. The noise voltage was sampled on the oscilloscope at 400 ps before the rising edge of detector pulses. The sampling rate of the oscilloscope was 40 GS/s and the bandwidth was set to 3 GHz.

$\sigma = 6.5$ ps and $1/\lambda = 13.6$ ps for the tapered detector. Here, σ is the standard deviation of the normal distribution, λ is the exponential decay rate. We observed a leading edge tail in IRF for the tapered detector. It is likely due to the counting events from the taper or the transition region between the taper and the detector.

We also compared the timing jitter at 1064 nm illumination, where both detectors operated at the saturation plateau (see Fig. 3-10 for the photon count rate vs. bias current curve for the tapered SNSPD). Similar jitter reduction was observed. The FWHM jitter reduced from 47.0 ps ($\sigma = 16.4$ ps, $1/\lambda = 15.9$ ps) to 22.4 ps ($\sigma = 6.2$ ps, $1/\lambda = 12.5$ ps).

3.7 Microwave characterization of impedance-matching taper

To characterize the microwave response of the impedance-matching taper, we fabricated two identical tapers connected head to head on the narrow end. The impedance therefore gradually transforms from 50Ω to $k\Omega$, then back to 50Ω . Doing so allows us to measure transmission spectra directly.

Figure 3-12 shows the measured S21 of two cascaded 116 MHz tapers used for

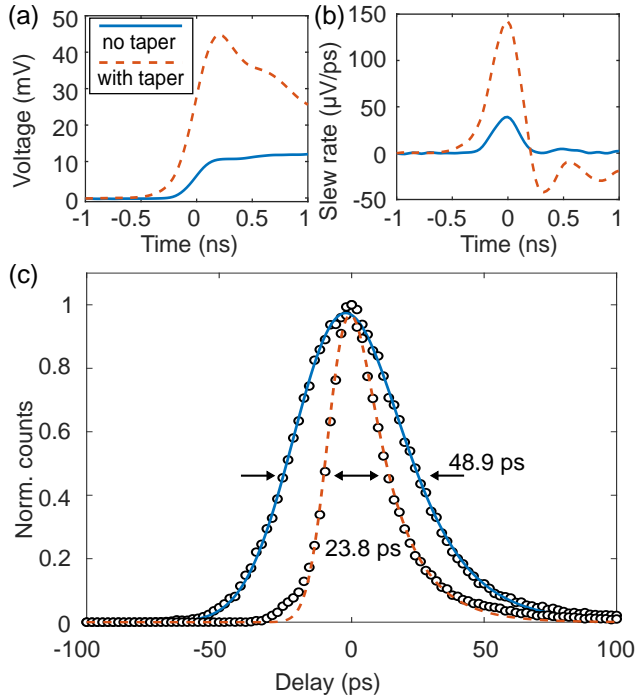


Figure 3-9: Experimental observation on the reduction of timing jitter as a result of faster slew rate. (a) Averaged rising edges of the detector pulses from the tapered and non-tapered detectors (amplifier gain not removed); (b) corresponding slew rate calculated as dV/dt . (c) The measured FWHM timing jitter reduced from 48.9 ps to 23.8 ps with the tapered readout.

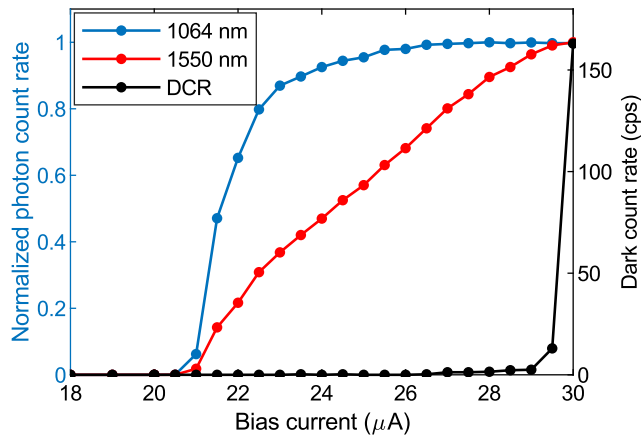


Figure 3-10: Normalized photon count rate (PCR, left axis) and dark count rate (DCR, right axis) as a function of bias current. At 1064 nm, the detector showed saturated internal quantum efficiency. All the pulse shape and jitter measurement reported in work were measured at a bias current of 27.5 μA .

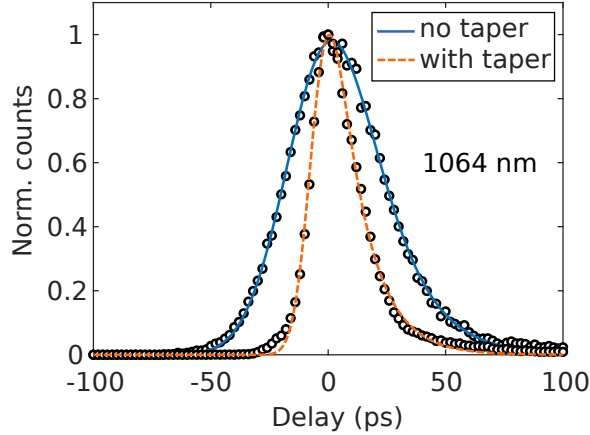


Figure 3-11: Instrument response function (IRF) under 1064 nm illumination. The bias current was kept at $27.5 \mu\text{A}$. For the reference detector, $\sigma=16.40 \text{ ps}$, $\lambda = 15.9 \text{ ps}$, $\text{FWHM}=47.0 \text{ ps}$. For the tapered detector, $\sigma = 6.2 \text{ ps}$, $1/\lambda = 12.5 \text{ ps}$, $\text{FWHM}=22.4 \text{ ps}$.

detector readout in Fig. 3-1. The taper was measured at 1.1 K, and the cable losses (calibrated at cryogenic temperature) was removed. We observed multiple resonance dips at frequencies above 2 GHz. They are likely caused by reflections at the bends, where CPW mode tends to convert to slotline modes due to the separated ground. To eliminate this problem, the CPW side grounds need to be well connected. In PCB design, this is achieved using by dense vias. So far, we have not developed a via process for thin-film NbN chips; instead, microstrip or “tunnel” transmission line discussed in Chapter 2 may be the near-term solution.

We also fabricated a shorter taper with a nominal cut-off frequency of 580 MHz and tested its transmission up to 8 GHz in a high-frequency packaging (gold-plated oxygen-free-copper box with flange-mount SMA connectors and Rogers PCB). We swept the temperature from 1.2 K to 6.0 K and observed red-shifts of the cut-off frequency as well as subsequent resonance dips (see Figure 3-13). These red-shift are due to increased kinetic inductance and hence large effective index of the nanowire transmission lines with increasing temperature.

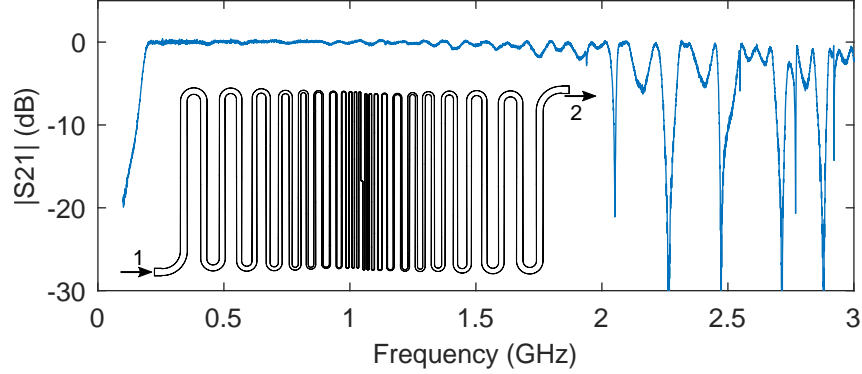


Figure 3-12: S_{21} of two cascaded 116 MHz tapers used in Fig. 3-1. Cable losses (measured at cryogenic temperature) were removed. The resonance dips above 2 GHz are likely caused by reflections from the bends, where CPW modes are converted to slotline modes. Microstrip or “tunnel” transmission lines may be used to avoid these reflections. The frequency range was limited by the RF packaging (FR4 PCB with surface-mount SMP connector).

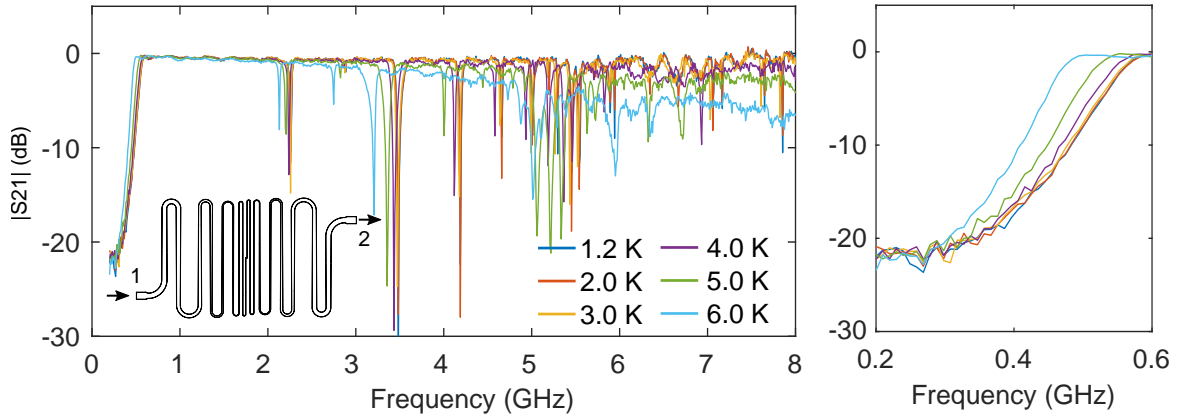


Figure 3-13: S_{21} of cascaded 580 MHz taper at different temperatures. Compared to the 116 MHz taper, this taper had a shorter length and fewer bends, and was measured in an RF package that works up to 10 GHz. As temperature increases, the electrical length of the taper increases due to the increased kinetic inductance, so the cut-off frequency red-shifts. Resonance dips due to reflections on the bends were again observed, and they red-shifted with increasing temperature as well.

3.8 Conclusions

In summary, by engineering the impedance of superconducting nanowires, we developed a tapered readout for SNSPDs. This readout method boosts detector’s output voltage, increases slew rate, and reduces timing jitter.

So far, we have treated the SNSPD as a lumped element, because the nanowire was

closely meandered and had a dispersion similar to an ideal inductor at the frequency of interest [38]. Despite this choice, multi-photon absorption would generate a different hotspot resistance than the single-photon events [80, 35]. We will show in the next chapter that the impedance taper provides an effective $k\Omega$ load without latching and enables direct discrimination of hotspot resistance and hence photon numbers. In another scheme, where the nanowire is sparse or integrated into a transmission line [86], the taper can serve as an impedance-matched readout and has been used to resolve photon location and photon numbers (Chapter 4 of this thesis) [40, 89]. We expect the integrated taper to become a widely used tool for matching high-impedance nanowire-based devices to low-impedance systems.

Chapter 4

Resolving photon numbers in tapered SNSPD

Time-resolved single-photon detection is crucial for photonic quantum technologies. Many quantum information processing protocols further rely on the ability to resolve photon numbers[90, 29, 32, 91, 92], such as linear optical quantum computing[93], quantum key distribution[94, 95], and non-classical state generation[96]. Here, we demonstrate a photon-number-resolving (PNR) detector at telecommunication wavelengths based on a superconducting nanowire with an integrated impedance-matching taper. The taper provides the nanowire a $k\Omega$ load impedance[71], making the detector's output voltage sensitive to the number of photon-induced hotspots. The superconducting tapered nanowire detector (STaND) demonstrated here was able to resolve up to five absorbed photons, and had 16.1 ps timing jitter, ~ 2 c.p.s. device dark count rate, ~ 86 ns reset time, and 5.6% system detection efficiency (without optical cavity). The large distinction between single- and multi-photon responses of the STaND made it ideal for coincidence counting. We used it to directly observe bunching of photon pairs from a single output port of a Hong-Ou-Mandel interferometer with 98.0% visibility.

This chapter builds on Chapter 3. It explores the multi-photon response of tapered SNSPDs. For convenience, we give an acronym to this detector architecture—Superconducting Tapered Nanowire Detector (STaND). This name suggests that (1)

the taper is an integrated part of the nanowire detector, and (2) the detector is beyond click/no-click. Materials presented in this chapter is prepared to be submitted to a journal for publication.

4.1 Introduction

Unlike transition-edge sensors (TES)[29] or microwave kinetic inductance detector (MKID)[30], SNSPDs do not resolve photon numbers and are categorized as click/no-click detectors. The common practice to circumvent this problem is to use an array of closely-packed nanowires, each detecting one photon[31, 32, 33]. The array is then read out through certain multiplexing schemes, but they usually require complex fabrication[32, 34] or signal processing[89]. Moreover, to avoid multiple photons hitting the same element, the array size must be much larger than the number of photons one wants to resolve [97, 31, 98]. These architectural limits have severely hindered the use of SNSPD arrays in applications that require PNR detectors.

Closer scrutiny of the detection mechanism suggests that the lack of photon-number-resolving (PNR) capability in SNSPDs may not be intrinsic. In 2007, Bell et al. recognized that n -photon absorption in a long meandered superconducting nanowire should induce n resistive hotspots (n is an integer)[80]. However, the resistance change due to different numbers of hotspots is hardly observable because of the large impedance mismatch between the hotspots/nanowire ($k\Omega$) and the readout circuitry ($50\ \Omega$). More specifically, regardless of n , the $50\ \Omega$ load will always divert most of the bias current in the nanowire, since $n\ k\Omega / (n\ k\Omega + 50\ \Omega) \approx 1$; and therefore, the output voltage remains almost constant. While it is possible to develop a high-impedance cryogenic readout to avoid this limitation [81, 76], the load impedance must be kept low to prevent latching effects [99]. As a result, matching the readout to the hotspot resistance remains impractical. As an alternative approach, Cahall et al. studied the rising edge slope instead of the output amplitude of the detector pulses and observed faster slew rate for multi-photon events [35, 100]. However, the resolution was largely limited by signal-to-noise ratios and variations of hotspot

resistances.

In Chapter 3, we developed an impedance-matching technique for SNSPDs based on tapered transmission lines[71]. The taper provided the SNSPD a $k\Omega$ load impedance while interfacing with the readout electronics at 50Ω . Here, we use it to enable photon number resolution in a single-element SNSPD. This detector architecture does not require multi-layer fabrication or complex readout, and offers significant advantages over array-type PNR detectors. It is particularly useful for applications that require multi-photon discrimination and high timing resolution.

4.2 Architecture and operating principle

The basic architecture of the tapered superconducting nanowire detector (STaND) is summarized in Figure 4-1. As introduced in Chapter 3, the STaND consists of two parts: (1) a photon-sensitive nanowire meander (similar to a conventional SNSPD), and (2) an impedance matching taper, whose characteristic impedance gradually decreases from $Z_H \sim k\Omega$ on the narrow end to $Z_L = 50 \Omega$ on the wide output end (Fig. 4-1(a); drawing not in scale; see Fig. 4-4 for micrographs of the device). The STaND can be represented using an equivalent circuit shown in Fig. 4-1 (b). The nanowire meander is modeled as a photon-number-dependent variable resistor $R_{HS}(n)$ in series with a kinetic inductor L_K [101]; and the taper is represented as an impedance transformer. n -photon absorption in the nanowire induces n initial hotspots, which then expand through electro-thermal feedback. In general, $R_{HS}(n)$ is at $k\Omega$ and increases with n (but scales sub-linearly, see Section 4.3). Following a simple division rule, the current leaving the nanowire (entering the taper) scales roughly as $\sim R_{HS}(n)/(R_{HS}(n) + Z_H)$. Note that this dependence on n becomes appreciable only when Z_H is comparable to R_{HS} , a condition that could hardly be achieved without the taper. The simplistic picture described here ignores the complex electrothermal feedback and microwave dynamics [71, 86]. Next, we study the detailed detection mechanism using SPICE simulations.

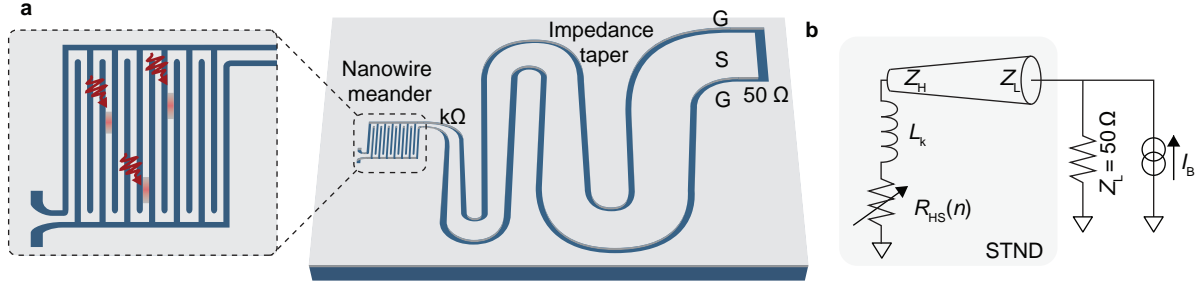


Figure 4-1: Architecture and working mechanism for superconducting tapered nanowire detector (STaND). **a**, The STaND consists of a photon sensitive nanowire meander, and a transmission line taper (drawing not in scale), whose characteristic impedance transitions from $k\Omega$ to $50\ \Omega$. Grey: NbN film; blue: substrate (SiO_2 on Si). Zoomed panel: n -photon absorption induces n hotspots in the nanowire meander. **b**, Equivalent circuit diagram of STaND. The variable resistor $R_{\text{HS}}(n)$ captures the photon-number-dependent hotspot resistance ($k\Omega$ scale). The taper provides an effective load impedance (Z_{H}) that is comparable to $R_{\text{HS}}(n)$, making the output voltage sensitive to n .

4.3 SPICE simulation

We simulate the STaND using a SPICE model that incorporates both the electrothermal feedback and microwave dynamics[86, 71, 85]. To simulate the multi-photon response, we model the nanowire meander as 5 lumped SNSPDs (each with $1/5$ of the total inductance) and trigger n of them simultaneously to mimic an n -photon event. Figure 4-2 shows the simulation setup. The taper is formed by 300 cascaded transmission lines, each section with impedance and phase velocity set to match the actual taper profile. The SPICE model of each SNSPD is implemented by Berggren et al. [85], based on the phenomenological hotspot velocity model by Kerman et al. [83]

Figure 4-3 shows the simulation results. Photons arrive at $t = 0$ ns. The hotspots start to grow immediately and push current in the nanowire meander towards the taper. After ~ 2 ns, the current leaves the taper at the low impedance end and enters the $50\ \Omega$ load (and the voltage across the $50\ \Omega$ load is what we see as output). In general, when more photons hit the nanowire, the total hotspot resistance grow faster and larger, and so does the output voltage. However, the maximum hotspot resistance scales sub-linearly as n . The taper bandwidth, nanowire inductance, and

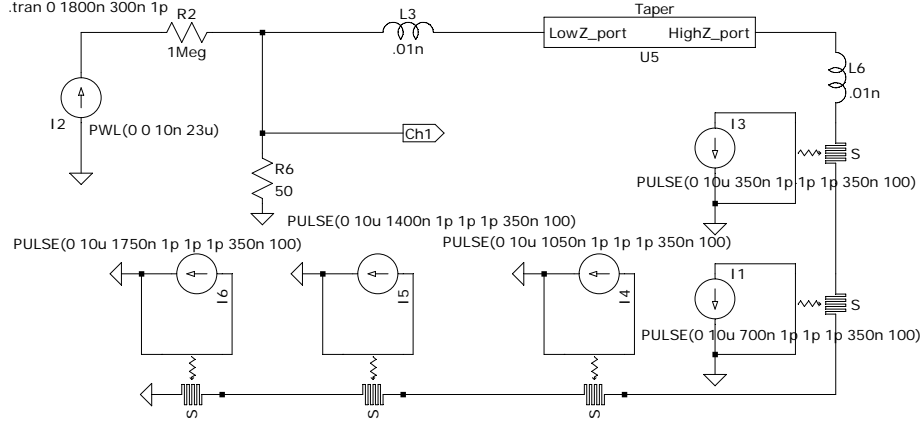


Figure 4-2: Schematics of the SPICE simulation for multi-photon events in the STaND. The taper is modeled as cascaded transmission lines (300 sections) with varying impedances and phase velocities. To mimic multi-photon events, we divide the nanowire meander into 5 small SNSPDs, each with $1/5$ the inductance, and trigger n of them simultaneously.

hotspot growth rate together determine the detector output. We have not been able to derive a closed-form analytical expression for it.

4.4 Device design and fabrication

The device design and fabrication followed Chapter 3, but the taper was modified to have a higher input impedance ($2.4 \text{ k}\Omega$) for better PNR, and a higher cut-off frequency (291 MHz) and thus shorter length for faster reset. Figure 4-4 shows micrographs of the device. The nanowire meander was 100 nm wide and covered an area of $11\mu\text{m} \times 10 \mu\text{m}$ with 50% fill factor. The taper was a coplanar waveguide with a fixed center conductor width of $3 \mu\text{m}$. Its center conductor width increased from 300 nm ($2.4 \text{ k}\Omega$) to $160 \mu\text{m}$ (50Ω) following the Klopfenstein profile[70]. The STaND reported in this work had a switching current of $25 \mu\text{A}$ at 1.0 K . The reference SNSPD compared in Fig. 4-7 was fabricated on the same chip with the same meander design, and had a switching current of $27 \mu\text{A}$.

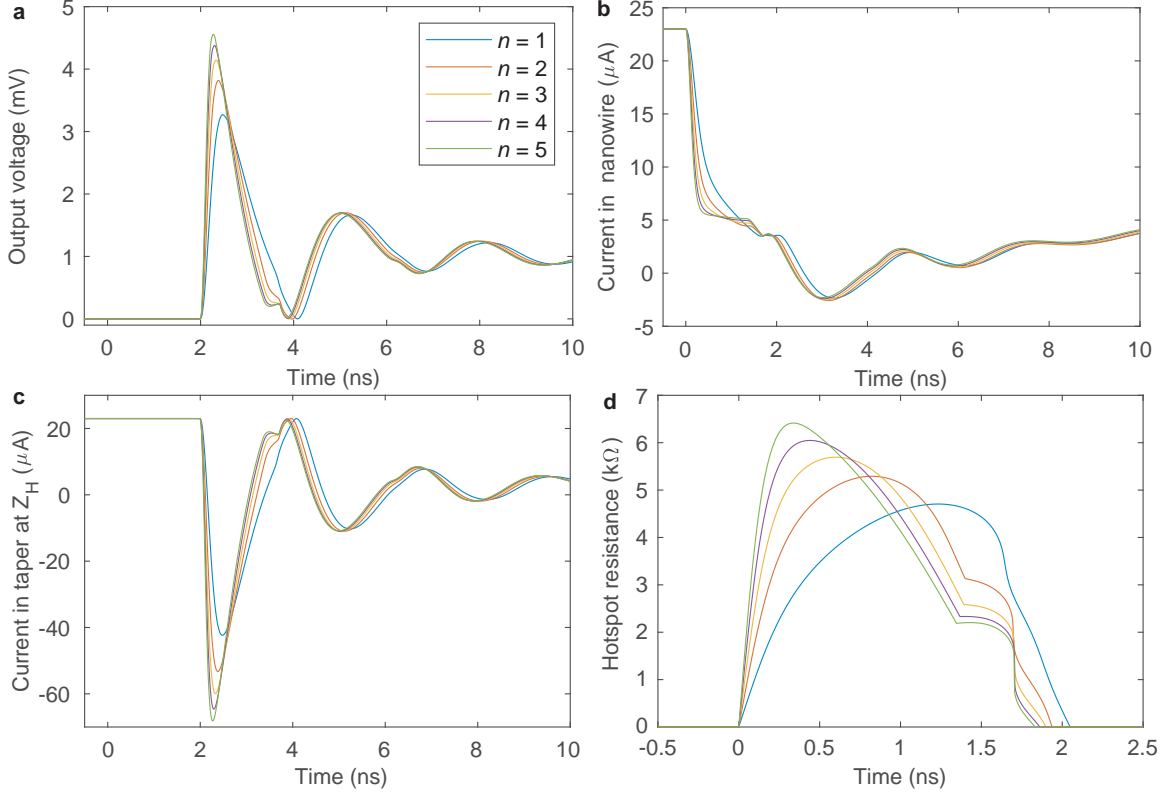


Figure 4-3: SPICE simulated pulse shapes, current distributions, and hotspot resistances in the STaND. (a) Output voltage on the 50Ω load resistor (output voltage); (b) Current in the nanowire, which is also the current at the high-impedance end of the taper (current flowing rightwards are defined as positive); (c) current in the taper at the low impedance (50Ω) end; (d) evolution of the total hotspot resistance. In general, more photons (i.e., more initial hotspots) create output pulses with larger amplitudes and faster slew rates. This result is qualitatively consistent with our experimental observations. The hotspot resistance increases as n , but scales sub-linearly.

4.5 Measurement setup

Figure 4-5 shows the measurement setup for characterizing the STaND. The detector chip was measured in a closed-cycle cryostat (ICE Oxford) at 1.0 K. Throughout the measurement the detector was biased at $23 \mu\text{A}$. Its output was amplified using room-temperature amplifiers—an RF Bay LNA2500 followed by a LNA2000. Because the output of the STaND was too large and saturated the second amplifier, a 16 dB attenuator was added in front. The amplified detector pulses were either captured using a 6 GHz oscilloscope (Lecroy 760Zi, 40 G samples/s sampling rate) or a universal

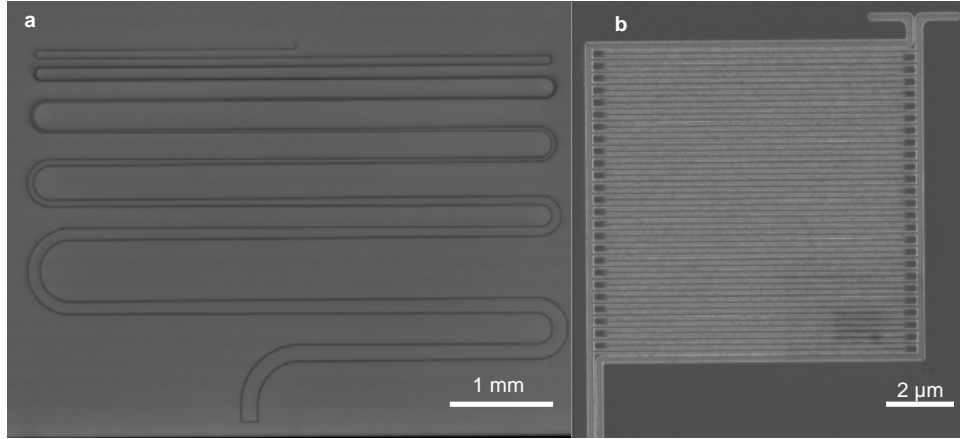


Figure 4-4: Micrographs of the STaND. (a) Optical micrograph of the taper. Its center conductor starts at 300 nm, and gradually increases to 160 μm . The darker outlines are the gap (3 μm). The taper size could be significantly reduced by using microstrip or grounded CPW designs. (b) Scanning electron micrograph of the nanowire meander. Dark regions are NbN; bright regions are substrate, where NbN was etched away.

counter (Agilent 53132A).

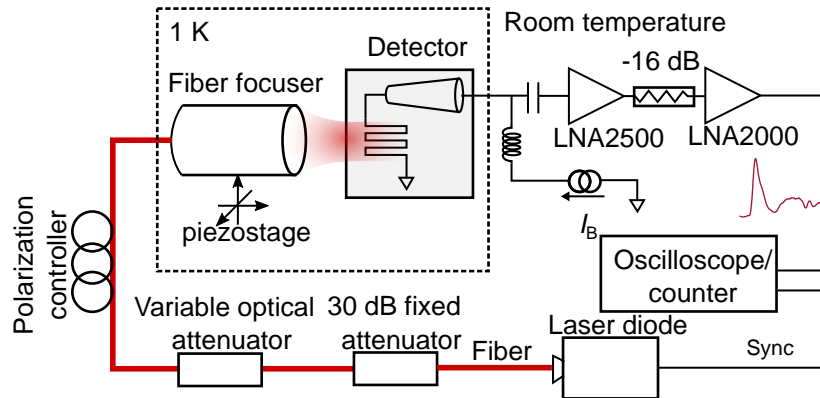


Figure 4-5: Measurement setup for characterizing the STaND with classical light source. The fiber-coupled pulsed laser diode (1550 nm) was attenuated and coupled to the detector chip with a fiber focuser. The fiber focuser was mounted on a piezopositioner (Attocube), and could be moved between the reference SNSPD and the STaND. The detector output was amplified by two room-temperature amplifiers, and a 16 dB attenuator was inserted in between to prevent saturation of the second.

A 1550 nm fiber-coupled modulated pulsed diode laser was used (PicoQuant LDH-P-C-1,550 laser head with PDL 800-B driver) to probe the multi-photon response of the STaND. It was attenuated (30 dB fixed fiber attenuator inline with a 0 – 100 dB calibrated variable attenuator) and coupled to the detector through a fiber

focuser. The input polarization was adjusted to maximize detection efficiency. The fiber focuser has a beam diameter ($1/e^2$) $< 10 \mu\text{m}$. It was mounted on a piezopositioner (Attocube ANPx101 and ANPz101 stack) and could focus on either the reference SNSPD or the STaND (see Fig. 4-6). We found that when the count rate was high (close to MHz), the detector output would charge the amplifier and the measured output pulses artificially drifted towards higher amplitude. To avoid this effect, we set the laser repetition rate to 100 kHz. In real detector systems where high count rate is necessary, an in-line cryogenic shunt can be added to eliminate charging.

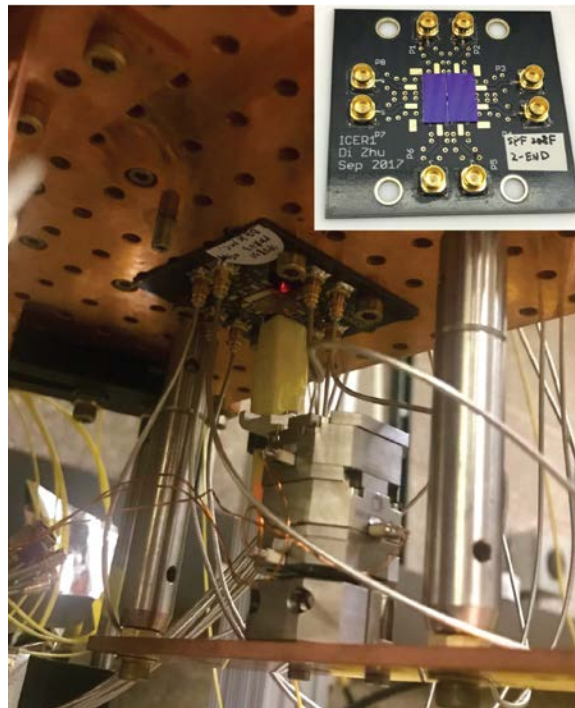


Figure 4-6: Optical alignment setup in the cryostat. A fiber focuser was mounted on a piezostage for real-time alignment at cryo-temperature. The chip was glued on a PCB using GE varnish and mounted directly on the 1 K plate of the cryostat.

When measuring timing jitter of the detectors, we used a 1550 nm mode-locked sub-ps fiber laser (Calmar FPL-02CCF). Since the 16 dB attenuator was not necessary for the reference SNSPD, we removed it to increase its signal-to-noise ratio (but kept it on for the STaND).

When measuring HOM interference, since the counter had a limited trigger level resolution (5 mV), we used a transistor-transistor-logic (TTL) comparator (PRL-

350 TTL, bandwidth: 300 MHz) for level discrimination, and used a programmable battery source (SRS SIM928, 1 mV resolution) to supply the threshold.

4.6 Photon number resolution

In this section, we show experimental results on multi-photon responses of the STaND, including amplitude separation, slew rate, rise time, and its ability to recover photon statistics of the coherent-state source.

4.6.1 Pulse shapes and timing jitter

Figure 4-7 compares the output waveforms from the STaND and a reference SNSPD. The STaND output not only had larger amplitude (> 3.6 times) and faster slew rate (> 4 times)[71], but also exhibited level separation (colored according to maximum pulse height for clear visualization). The faster slew rate reduced timing jitter (from 27.4 ps full-width at half-maximum (FWHM) to 16.1 ps at 1,550 nm, as shown in Fig. 4-7 inset). The level separation led to photon number resolution. Other than amplitude difference, the pulse shapes were also observed to exhibit distinct signatures due to microwave reflections in the nanowire and taper. For example, the blue traces separate at $t = 3$ ns, making three- and higher-photon events distinguishable.

4.6.2 Pulse height distribution

Figure 4-8 shows histograms of the pulse heights when the detector was probed using the 1550 nm modulated pulsed laser. The laser was deeply attenuated and the effective mean photons per pulse $\tilde{\mu}$ was varied 3.21×10^{-2} to 1.02×10^1 , where $\tilde{\mu} = \eta\mu$ included the coupling losses and detector efficiencies. We observed level separation up to five photons. When $n \geq 5$, the levels were no longer separable, and further increasing $\tilde{\mu}$ only gradually shifted the peak position.

In the pulse height histograms, we observed a broad shoulder at < 220 mV, and the should was more prominent for dark counts (black line). This shoulder was likely

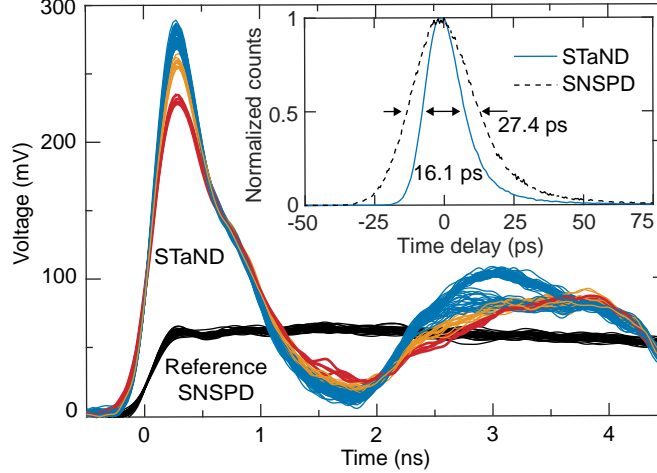


Figure 4-7: Pulse shape and timing jitter. Compared to a regular SNSPD (black traces), the output pulses from the STaND (colored traces) not only had larger amplitude and faster slew rate but also showed level separation for multi-photon events. Red: single-photon events; orange: two-photon events; blue: three- or higher-photon events. Inset: instrument response function at 1550 nm in the single-photon regime, where STaND showed a FWHM timing jitter of 16.1 ps as compared to 27.4 ps for the reference SNSPD.

from counting events at the nanowire bends as shown in Fig. 4-9, where the nanowire width gradually increases. In these regions, the hotspot cannot grow as large as that in the middle of the meander, and its size has larger variation due to the range of widths in the bends. Moreover, current tends to crowd in the bends and create “hot” corners that are more likely to generate dark counts. To further confirm this hypothesis, we drove the fiber focuser out of focus to illuminate more on the bends, and observed increased shoulder that is similar to the dark count histogram (Fig. 4-10). It will be interesting to see if a spiral SNSPD would have reduced shoulder [102, 103].

4.6.3 Rise time and rising-edge slope

In Fig. 4-11, we processed the detector pulses at a range of optical attenuations (63 dB to 81 dB with 3 dB steps; 63 dB corresponded to $\tilde{\mu} = 5.1$) and extracted their rising edge slope (slew rate) and rise time. The slope was extracted by linearly fitting the rising edge from 40% to 60% pulse amplitudes, while the rise time was extracted as 20% to 80% time span.

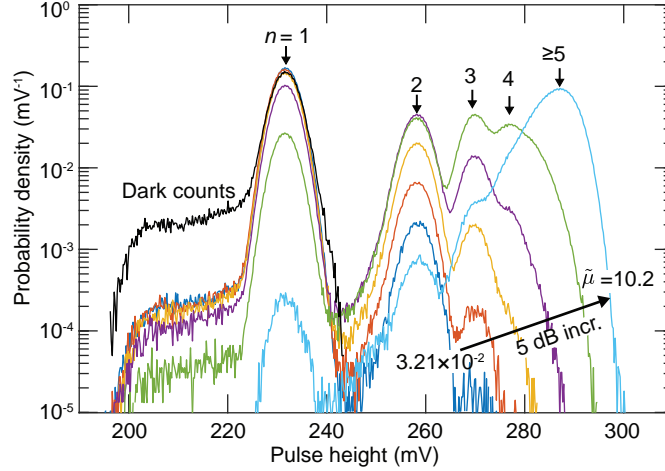


Figure 4-8: Histograms of the STaND's pulse heights under pulsed laser illumination. The effective mean photon per pulse $\tilde{\mu}$ were attenuated from 10.160 to 0.032 with 5 dB steps. Each photon counting histogram was constructed from 10^6 detection events, while the dark count histogram (black curve) was from 2×10^5 events.

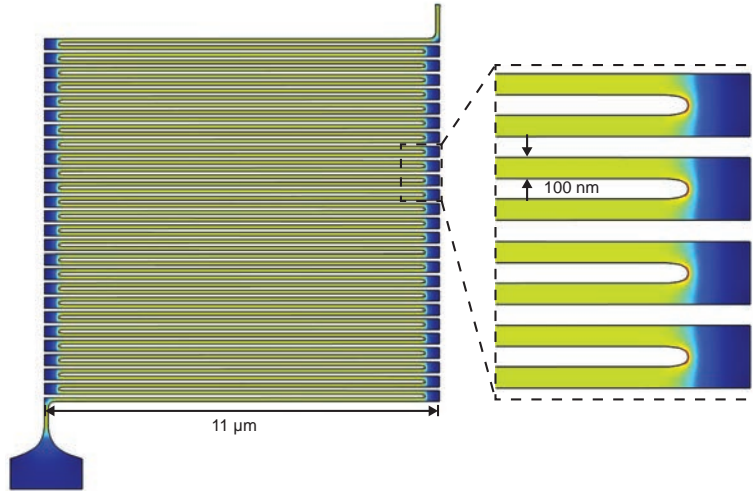


Figure 4-9: Geometry and current density near the bends. At the bends, the nanowire gradually increases its width. Despite the use of optimized bending curve[48], there are still some current-crowding effect. These areas had higher current density and are prone to generate dark counts. Color represents current density; red: high; blue: low.

The slope roughly followed a linear correlation to the pulse amplitude, and thus could also be used to resolve photon numbers, similar to the results reported by Cahall et al.[35] However, in our detector architecture, the slope had less distinction than amplitude. As shown in Fig. 4-11(a), the detection events are less separable

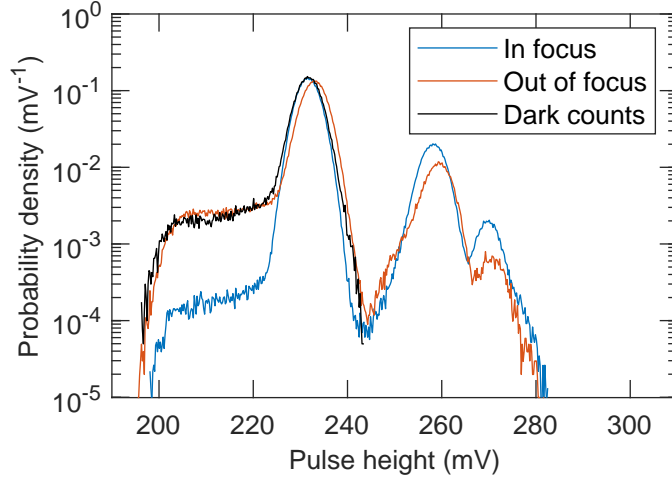


Figure 4-10: Comparing pulse height distributions under different illumination conditions. When we drove the fiber focuser far away from the detector, light uniformly illuminated both the wires and bends. In this case, we observed increased shoulder (similar to the dark count), strongly suggesting that the shoulder were originated from the bends.

along the y-axis (slope) than along the x-axis (amplitude). In Fig. 4-11(b), the rise time is around 200 ps, and reduces slightly as photon number increases. These results qualitatively follow our SPICE simulation—larger number of photons generate detector pulses with larger amplitudes, faster slew rates, and shorter rise time.

4.6.4 Photon statistics

Figure 4-12(a) and (b) show Gaussian fittings of the pulse height histograms at $\tilde{\mu} = 1.01$ and 3.19. The FWHM of individual Gaussians (5.5 mV for $n = 1$ and > 5.8 mV for $n \geq 2$) was larger than the measured electrical noise floor in the system (4.2 mV FWHM, see Fig. 4-13), suggesting the existence of other fluctuation mechanisms. The excessive fluctuation may be due to the following factors. (1) Variation in the nanowire width may cause different hotspot sizes, viz., wider wires generally create smaller hotspots and vice versa. (2) Variation in hotspot location may result in different microwave dynamics, viz., hotspots near the taper will experience different RF reflections than the ones near the ground. This effect is particularly significant when the wire length is long, where the lumped element picture breaks down and

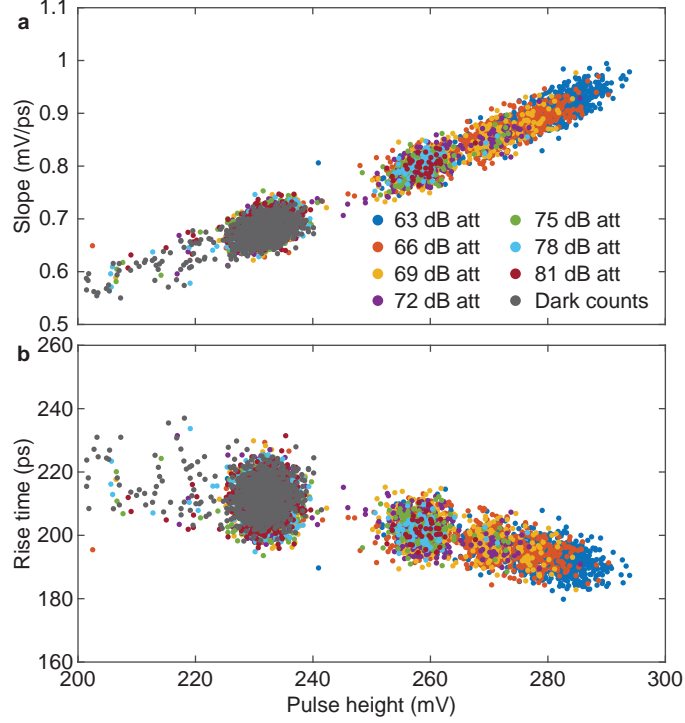


Figure 4-11: Correlation among pulse height, rising slope (a), and rise time (b). In general, more photons generate pulses with larger amplitude, faster slew rate, and slightly shorter rise time. Pulse amplitude shows the clearest distinction among the three. For each optical attenuation, 1000 pulse traces were recorded and post-processed. The slope was linearly fitted from 40% to 60% pulse amplitude, and the rise time was extracted as the time to increase from 20% to 80% pulse amplitude. The effective mean photon per pulse at 63 dB attenuation was 5.1.

distributed model becomes appropriate[86, 89, 40]. (3) Variation in inter-arrival time of the photons may cause difference in hotspot evolution, viz., if the second photon is delayed relative to the first photon, it will see a reduced bias current and the hotspot growth will be slower.

Here, the separation between single- and two-photon events (26.4 mV) was more than 10.7 standard deviations (σ) of their spreading, making the STaND suitable for high-fidelity coincidence counting.

We integrated the area under each Gaussian curve to reconstruct the counting statistics $Q(n)$ (Fig. 4-12(c)). We grouped $Q(n \geq 4)$ since these events were not well-separated. In general, $Q(n)$ directly followed the Poisson statistics of the laser source $S(n) = e^{-\tilde{\mu}} \tilde{\mu}^n / n!$. Since the total length of the nanowire ($\sim 500 \mu\text{m}$) was about 1,000

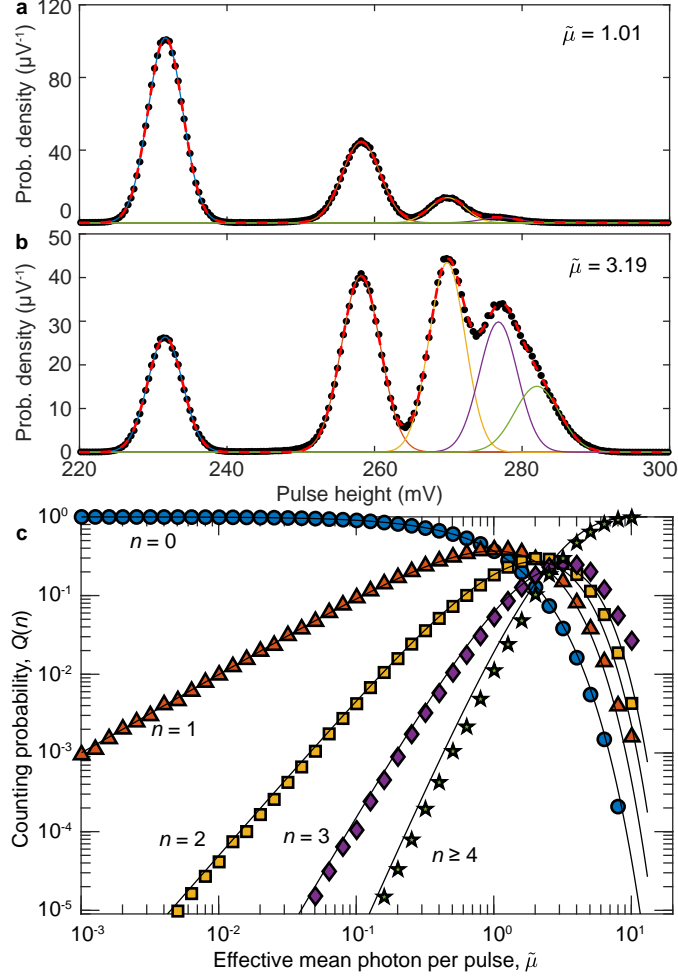


Figure 4-12: Counting statistics under coherent state illumination. **a**, **b**, Gaussian fitting of the pulse height histogram when the STaND was illuminated using a pulsed laser with $\tilde{\mu}$ at 1.01 and 3.19, respectively. Black dots: measurement data; dashed red line: fitting result; solid lines: decomposed Gaussian functions. **c**, Photon counting statistics reconstructed from the pulse height distributions. $Q(n)$ is the probability of detecting an n -photon event. The measured counting statistics (symbols) followed the Poisson statistics of the coherent source, $S(n) = e^{-\tilde{\mu}} \tilde{\mu}^n / n!$ (lines).

times longer than the hotspot size (100s of nm), the probability of overlapping, usually a significant factor in finite-size spatially-multiplexed PNR detectors [32, 89, 31], was negligible here. However, the STaND required the photons to overlap in time. We discuss this aspect next.

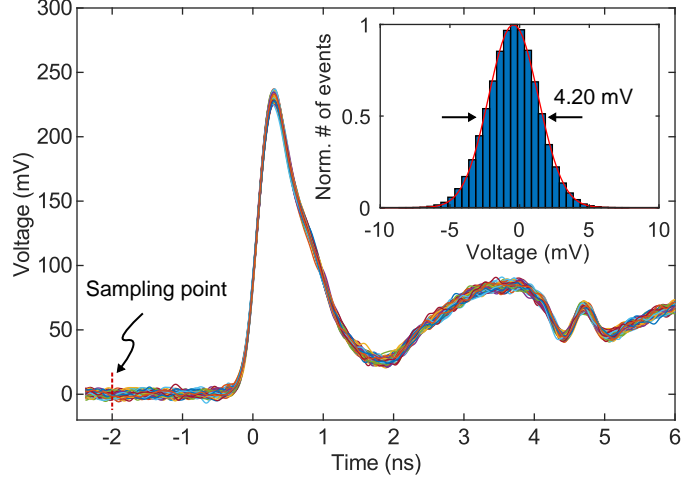


Figure 4-13: System electrical noise. We sampled the electrical noise on the oscilloscope at 2 ns before the rising edge of the detector pulses. The noise followed a Gaussian distribution with a FWHM of 4.20 mV ($\sigma = 1.78$ mV).

4.6.5 Effects of photon inter-arrival time

The working principle of PNR in the STaND requires photons to arrive simultaneously, i.e., the photon wavepacket needs to be short temporally. Upon absorption of the first photon, the current in the nanowire starts to drop immediately. It takes about 200 ps for the current to drop to 90% (inferred from detector rise time in Fig. 4-11(b)), and more initial hotspots, the faster the current drops (Fig. 4-3(b)). If the second photon arrives with some time delay, the nanowire will be at a lower bias current. The second photon will either create a smaller hotspot or fail to initiate a hotspot expansion at all. Therefore, if the laser pulse width is wide (e.g., more than 50 ps), higher-photon events are likely to be under-estimated.

The pulse width of the modulated laser diode used in our experiments could be changed by tuning the drive current. Since the STaND had a timing jitter as small as 16.1 ps, we used it to directly estimate the laser pulse width. Figure 4-14 shows the measured time delay between laser sync signal and detector output when the modulated laser diode was driven at different current settings (these settings are nominal values and the actual currents were not measured). In the previous sections, all experiments were performed with the current setting at 2.5, which produced 33 ps (FWHM) pulses. When we increased the drive current ($I_d = 4.0$), the pulse width

increased to ~ 100 ps (FWHM), and the measured photon statistics differed significantly from the expected Poisson statistics of the source (see Fig. 4-15), especially for higher photon numbers.

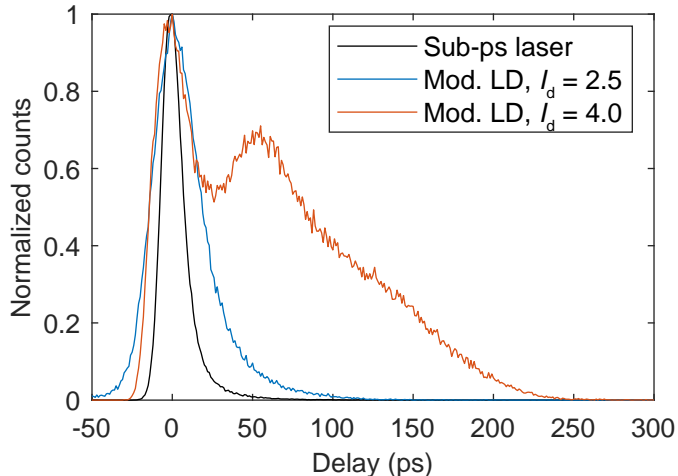


Figure 4-14: Estimating laser pulse width using the STaND. The time delay between the laser sync signal and detector pulses were measured. Since the sub-ps laser has negligible pulse width (laser pulse width: 0.18 ps, spectral width: 16.18 nm, fiber dispersion: 18 ps/(nm·km), calculated pulse broadening from 2 m fiber: ~ 0.6 ps), the black curve represents the detector’s instrument response function. When the modulated laser diode was driven at current setting of 2.5, the pulse width was ~ 33 ps (FWHM); and when it was driven at 4.0, the pulse broadened significantly (~ 100 ps FWHM) and became asymmetric.

4.7 Direct observation of photon bunching in Hong-Ou-Mandel interference

The large distinction between single- and multi-photon responses of the STanND makes it ideal for coincidence counting. Here, we demonstrate its direct application in measuring non-classical states of light.

When two indistinguishable photons interfere at a beam splitter, they tend to leave from the same output-port (bunching), a phenomenon known as Hong-Ou-Mandel (HOM) interference [104]. It is usually measured using two single-photon detectors—one at each output-port. A coincidence dip then indirectly infers that the

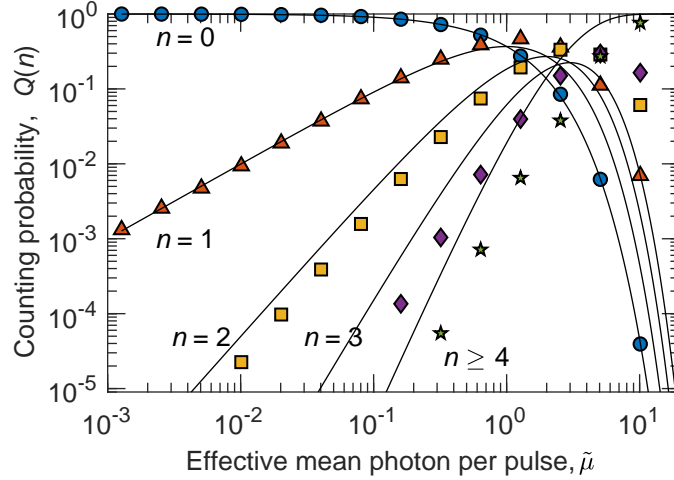


Figure 4-15: Counting statistics when the modulated laser diode was driven to have a wider pulse width (~ 100 ps FWHM, shown as orange curve in Fig. 4-14). Higher-photon-number events were significantly under-estimated. Symbols: measured data; lines: theoretical photon statistics of the source, $S(n) = e^{-\tilde{\mu}} \tilde{\mu}^n / n!$.

two photons leave from the same port. The STaND, however, allows us to directly observe the photon bunching from a single output-port of the beam splitter[105, 106].

Figure 4-16(a) shows the experimental setup for the HOM interference. Frequency-entangled photon pairs were generated from SPDC process in a type-II phase-matched periodically-poled KTiOPO4 (PPKTP) crystal pumped by an 80-MHz mode-locked, ~ 100 fs (FWHM 7.8 nm) Ti:sapphire laser centered at 791 nm at 90 mW [107, 108]. The crystal was temperature stabilized at 21.4°C to yield degenerate signal and idler output at 1582 nm. After the pump was filtered by a long-pass filter (Semrock BLP02-1319R-25), the orthogonally-polarized signal and idler photons were coupled into a polarization maintaining (PM) fiber. The signal and idler were separated by a polarization beam splitter and recombined on a 50:50 beam splitter. The polarization of signal and idler photons were made to be the same through a polarization controller; and their relative delay (τ) was controlled using a tunable air gap on a translational stage (~ 3 dB loss). One output of the beam splitter was connected to the STaND located in a different building while the other output was left unconnected. The polarization of the output photons were tuned for the maximum detector efficiency.

We used a comparator for level discrimination. It would generate a pulse only

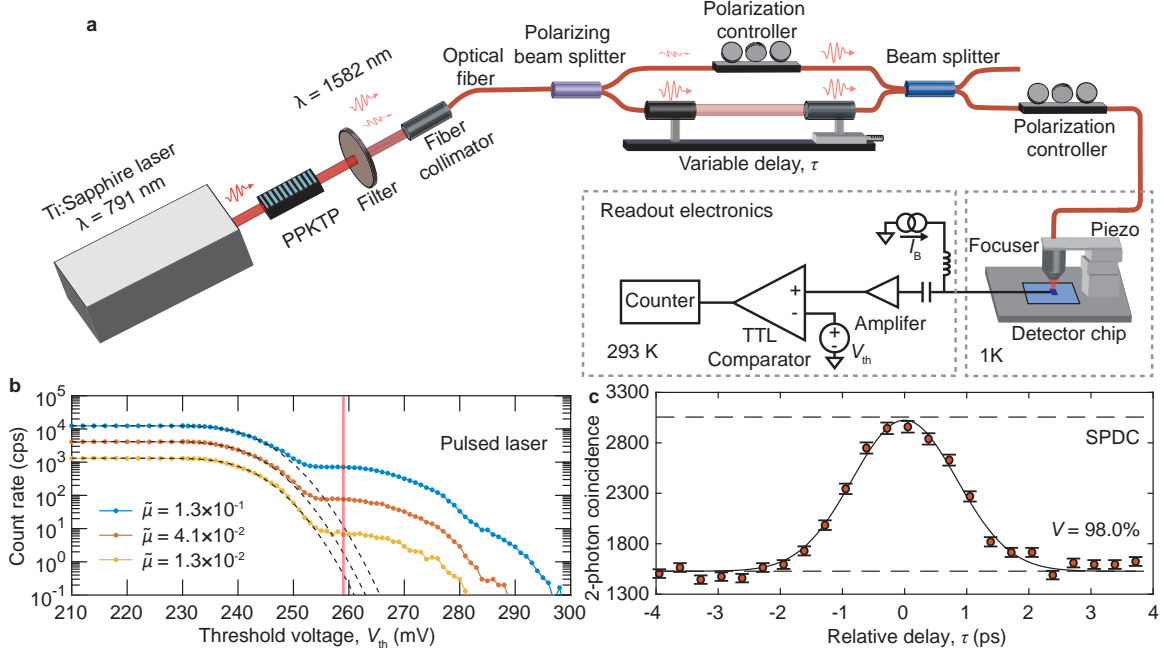


Figure 4-16: Measuring Hong-Ou-Mandel interference (HOM) interference using a single STaND. **a**, Experimental setup. Frequency-entangled photon pairs were generated in a type-II phase-matched PPKTP crystal and were separated based on their polarization. They then interfere at a 50:50 beam splitter with a relative time delay τ , and the coincidence was monitored using a STaND at a single output port. The amplified detector pulses went through a TTL comparator, whose threshold voltage V_{th} was set by a programmable battery source. **b**, Calibrating the comparator threshold voltage for coincidence counting with a pulsed laser ($f_{\text{rep}} = 100$ kHz). Dashed lines are erfc fitting, and the red line at 259 mV marks the chosen V_{th} for coincidence counting. **c**, Coincidence counts (with background subtracted) measured in a 300 s time window as a function of relative delay between the two photons, showing clear bunching with interference visibility of 98% (well above the 50% classical limit). Error bar: one standard deviation due to Poisson noise; solid curve: Gaussian fit; dashed lines: base line and theoretical ceiling for perfect interference (twice the base line).

when the input passed the threshold voltage V_{th} . Figure 4-16(b) shows the count rate registered at the counter as a function of V_{th} when the detector was illuminated with a pulsed laser at 100 kHz repetition rate. We chose $V_{\text{th}} = 259$ mV as the coincidence counting threshold, which, from a complementary error function (erfc) fitting of the roll-off (black dashed lines in Fig. 4-16(b)), is 3.28σ away from the single-photon main peak (241 mV). The limited bandwidth (300 MHz) and noise performance of the comparator had largely degraded the level discrimination integrity. Nevertheless,

it was faster than post-processing and had finer threshold resolution than the counter’s internal trigger settings.

Figure 4-16(c) shows the coincidence counts (300 s integration time) as a function of the relative time delay τ . It shows clear photon bunching with interference visibility V of $98.0 \pm 3.0\%$ (uncertainty indicates 95% confidence bound of the Gaussian fitting). V is defined as $(N_{\max} - N_{\min})/N_{\min}$, where $N_{\max/\min}$ represents the maximum (minimum) coincidence counts. Here, we subtracted background two-photon counts (55 ± 7 from the air-gap delay path and 256 ± 16 from the polarization controller path) measured by blocking individual beam path of the interferometer. These background two-photon counts were likely caused by non-perfectly degenerate signal idler spectrum, imperfections in polarization controls, and multi-pair events from SPDC process. Without subtraction, the raw coincidence counts had visibility of $81.4 \pm 2.8\%$. In the experiment, we did not observe any two-photon dark counts (with pump laser blocked) during the integration time, which ensured high signal-to-noise ratio for the measurement.

In this experiment, we only had access to one STaND. Rigorously, the other output-port of the beam splitter should also be measured using a STaND, similar to Ref. [105]. The correlations between the two STaNDs can then comprehensively confirm the quantum interference and rule out other possibilities such as interference of coherent laser pulses with specific phase relation. However, since the SPDC source used here was already tested using a standard HOM setup with commercial click/no-click SNSPDs [107, 108], the bunching effects observed here should be interference from indistinguishable single photons.

4.8 Other basic detector metrics

Here, we report the detector efficiency, dark count rate, and reset time of the STaND. We also show that the reset time and footprint can be reduced using a grounded CPW taper.

4.8.1 Efficiency and dark count rate

Figure 4-17(a) shows the normalized photon count rate (PCR) as a function of bias current. Under 1064 nm illumination, the detector showed saturated quantum efficiency. At 1550 nm, it passed its inflection point and was close to saturation. At 23 μA with 1550 nm illumination, we measured the system detection efficiency (including coupling loss up to the fiber feedthrough at the cryostat) to be $\sim 5.6\%$.

Figure 4-17(b) shows the dark count rate (DCR). When the fiber focuser was moved away, the DCR dropped by an order of magnitude, indicating that the DCR was dominated by leakage photon channeled through the fiber. At $I_B = 23\mu\text{A}$, the system dark count rate (fiber in focus) was 26.8 c.p.s., and the device dark count rate (fiber out of focus) was 1.7 c.p.s.

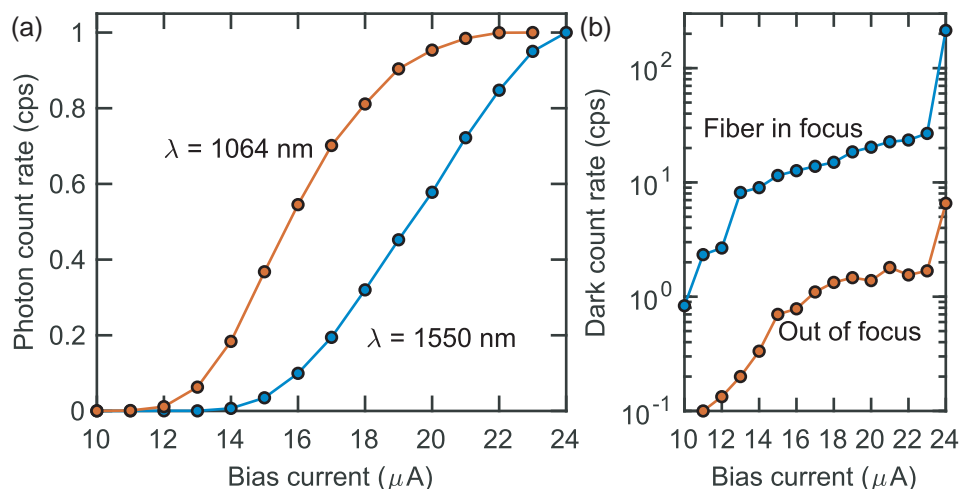


Figure 4-17: Normalized Photon count rate (PCR) and dark count rate (DCR) as functions of bias current.

4.8.2 Reset time

We estimated the detectors' reset time from the pulse decay. The reset time of the SNSPDs and STaNDs is limited by the kinetic inductance, and the output pulse follows an exponential decay $\exp(-t/\tau)$, where $\tau = L/R$. L is the total inductance of the device, including both the nanowire meander and the taper, and $R = 50\ \Omega$ is the load impedance of the readout circuitry.

Figure 4-18 shows the averaged pulse shapes of the SNSPD (a) and STaND (b). To reduce reflection and overshoot in the slow decay, we used an amplifier with lower frequencies (MITEQ AM-1309, gain: 50 dB, bandwidth: 1 kHz - 1 GHz) instead of the LNA2500 (100 kHz - 2.5 GHz) and LNA2000 (10 kHz - 2 GHz). Note that the MITEQ amplifier was saturated at the rising edge, but it did not affect our analysis on the falling tail. From exponential fitting, we have $\tau = 9.5$ ns for the reference SNSPD and $\tau = 28.6$ ns for the STaND. Using $1/(3\tau)$ as a rule of thumb, their maximum count rates were 35.1 MHz and 11.7 MHz, respectively.

The SNSPD was designed to be 5,200 squares, and the STaND was designed to be 21,800 squares (i.e., the taper was 16,600 squares). The fitted L/R time constants did not strictly follow the ratio of the device's number of squares. This deviation may be due to (1) the nanowire meander had larger sheet inductance due to the presence of near-switching bias current, or (2) fabrication error that led to discrepancy in device geometry.

4.8.3 Reducing taper size with grounded CPW design

The taper footprint and inductance can be readily reduced by using microstrip or CPWs with closely placed top or bottom ground (grounded CPW). Figure 4-19 compares the sizes of (a) the CPW taper used in this work and (b) a grounded CPW taper. The calculated grounded CPW taper shown in Fig. 4-19(b) has a gap size of 1 μm , and a top gold ground separated by a 120 nm SiO_2 spacer. The substrate is Si with 300 nm thermal oxide. Adding the top ground increases the capacitance per unit length of the transmission line, which increases the effective index and reduces taper size. Both tapers follow Klopfenstein profile[70] and have the same cut-off frequency at 290 MHz. They both start with 300 nm center conductor width, and end with 50 Ω impedance. The CPW taper has a total length of 52 mm (16,600 squares). Assuming a sheet inductance of 80 pH/sq for the NbN film, the total inductance will be $\sim 1,328$ nH. The grounded CPW taper, on the other hand, only has a length of 11 mm (9118 squares) and total inductance of 729 nH. Moreover, the gold ground may serve as a mirror to form an optical cavity with a properly chosen dielectric spacing[109].

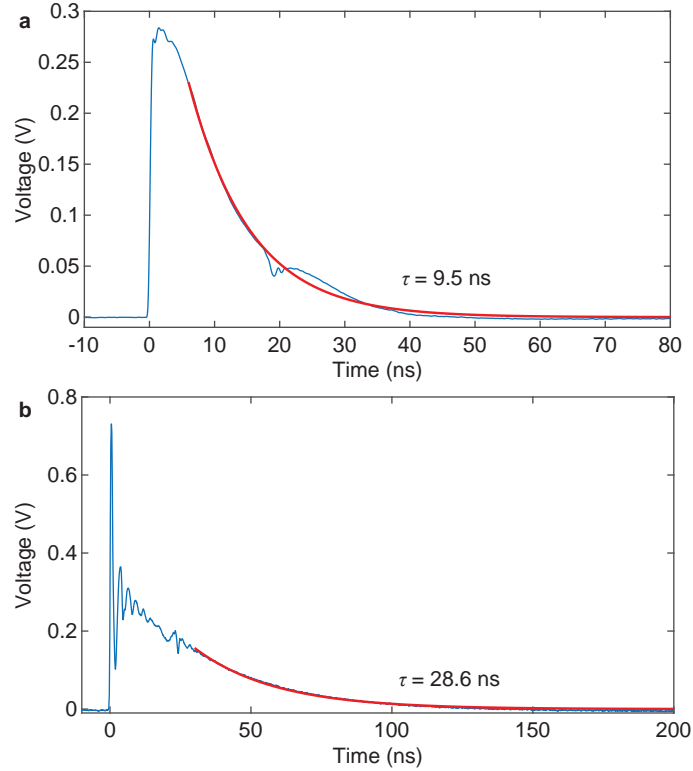


Figure 4-18: Estimating reset time from pulse decay. Exponential fitting ($e^{-t/\tau}$, where $\tau = L/R$) of pulse decay shows that reference SNSPD has τ of 9.5 ns (a), and the STaND has τ of 28.6 ns.

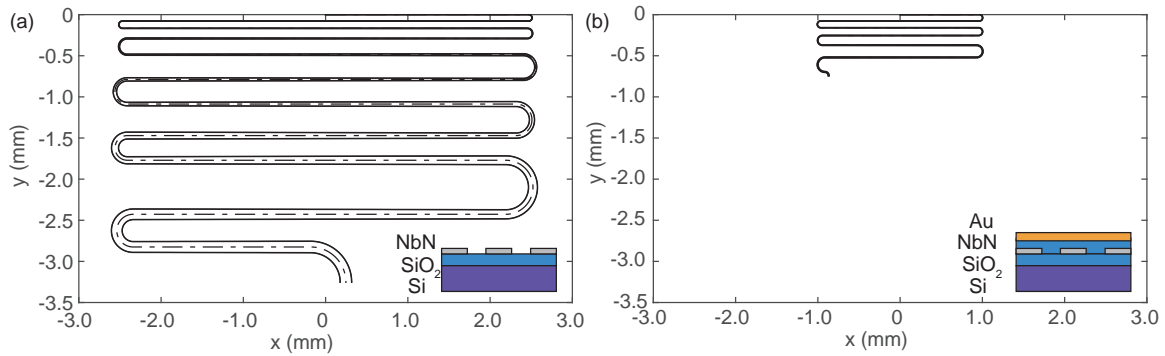


Figure 4-19: Reducing taper inductance and footprint by using CPW with a top ground. (a) Profile of the CPW taper used in the measured device. (b) Profile of a CPW taper (1 μm gap) with top ground (grounded CPW). Adding a gold ground on top of the NbN with a 120-nm-thick SiO_2 spacer increases the line inductance and shrinks the size of the taper. Both tapers have the same cut-off frequency (290 MHz) and initial center conductor width (300 nm). The CPW in (a) is 52 mm long and has 16600 squares (1,328 nH assuming 80 pH/sq for the NbN film), while the grounded CPW in (b) is only 11 mm long and has 9118 squares (729 nH). The reduced inductance will shorten the reset time of the detector.

4.9 Derivation of photon counting statistics

In this section, we justify the use of effective mean photon per pulse $\tilde{\mu}$ in our measurement, and derive the advantage of using STaNDs arrays over SNSPDs arrays for resolving large number of photons.

4.9.1 Counting statistics and estimation of effective mean photon per pulse

Here we show, in the case of coherent state illumination, that the coupling loss and detector efficiency can be treated as an effective attenuation to the source, and the effective mean photon $\tilde{\mu} = \eta\mu$ can be estimated by fitting the photon count rate as a function of the known optical attenuation applied to the pulsed laser source.

A uniformly illuminated STaND can be treated as a spatially-multiplexed, N -element (N is on the order of 1,000), uniform detector array. Such detector array is usually modeled as an N -port beam splitter, where each output port is coupled to a single-photon detector with efficiency η . For n -photon input, the probability of no-click is $P_\eta^N(0|n) = (1 - \eta)^n$, and the probability of getting the photon number correctly is $P_\eta^N(n|n) = (\eta/N)^n N!/(N - n)!$, for $n \leq N$. The cases in between, i.e., input has n photon but detector tells k , can be solved recursively[98, 31],

$$P_\eta^N(k|n) = \binom{N}{k} \sum_{j=0}^k (-1)^j \binom{k}{j} \left[(1 - \eta) + \frac{(k - j)\eta}{N} \right]^n \quad (4.1)$$

where $\binom{N}{k} = N!/[k!(N - k)!]$.

For coherent state illumination with a mean photon number of μ , the counting

probability follows

$$\begin{aligned}
Q(k) &= \sum_{n=0}^{\infty} P_{\eta}^N(k|n) S_{\mu}(n) \\
&= \sum_{n=0}^{\infty} \binom{N}{k} \sum_{j=0}^k (-1)^j \binom{k}{j} \left[(1-\eta) + \frac{(k-j)\eta}{N} \right]^n \frac{e^{-\mu} \mu^n}{n!} \\
&= \binom{N}{k} e^{\frac{\eta\mu(k-N)}{N}} \left(1 - e^{-\frac{\eta\mu}{N}} \right)^k,
\end{aligned} \tag{4.2}$$

where $S_{\mu}(n) = e^{-\mu} \mu^n / n!$ is the Poisson statistics of a coherent state input.

Now, if we illuminate a unity-efficiency detector array using a coherent state with mean photon $\tilde{\mu} = \eta\mu$, the counting probability will be

$$\begin{aligned}
Q'(k) &= \sum_{n=0}^{\infty} P_{\eta=1}^N(k|n) S_{\tilde{\mu}}(n) \\
&= \sum_{n=0}^{\infty} \binom{N}{k} \sum_{j=0}^k (-1)^j \binom{k}{j} \left[\frac{(k-j)}{N} \right]^n e^{-\tilde{\mu}} \frac{\tilde{\mu}^n}{n!} \\
&= \binom{N}{k} e^{\frac{\eta\mu(k-N)}{N}} \left(1 - e^{-\frac{\eta\mu}{N}} \right)^k,
\end{aligned} \tag{4.3}$$

which is identical to $Q(k)$, meaning that the counting statistics is equivalent between the two cases. Note that when $N \gg k$, $Q(k) \approx e^{\tilde{\mu}} \tilde{\mu}^k / k!$, which is appropriate for Fig. 4-12(c).

To estimate $\tilde{\mu}$ experimentally, we measured the photon count rate (*PCR*) as a function of applied optical attenuation (γ), as shown in Fig. 4-20. Since the clicking probability PCR/f_{rep} is essentially $Q(k \geq 1) = 1 - Q(k = 0)$, we fit it with $1 - \exp(-\gamma\tilde{\mu})$, and get $\tilde{\mu} = 10.080 \pm 0.050$ at 60 dB attenuation. The accuracy of this method was ensured by the stability of laser power and repetition rate as well as calibration of the variable optical attenuator. The use of $\tilde{\mu}$ in analyzing the measured counting statistics helped us isolate the detector's intrinsic architectural limit of PNR from external factors that could be later optimized, such as optical coupling loss and absorption efficiency.

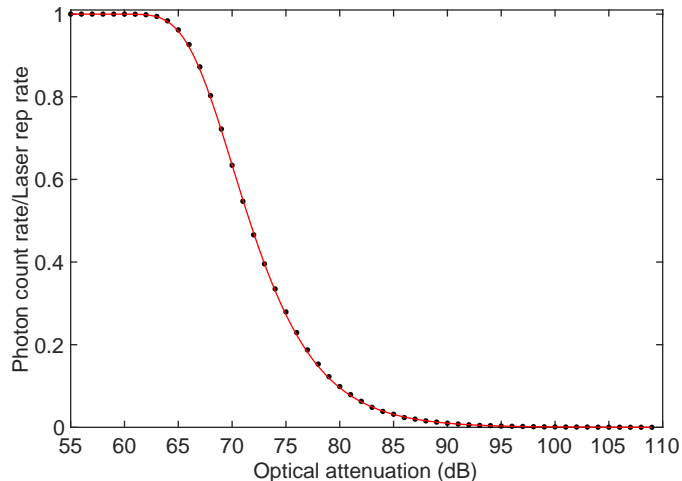


Figure 4-20: Estimation effective mean photon per pulse $\tilde{\mu}$. For coherent state illumination, the counting/clicking probability $P_{\text{click}} = PCR/f_{\text{rep}} = 1 - \exp(-\gamma\tilde{\mu})$, where PCR is the photon count rate, f_{rep} is the laser repetition rate, γ is the applied optical attenuation. By fitting the counting probability as a function of applied external optical attenuation, we get $\tilde{\mu} = 10.080 \pm 0.050$ at 60 dB attenuation (uncertainty indicates 95% confidence bound).

4.9.2 STaND array vs. SNSPD array

Similar to spatially multiplexed SNSPD arrays, it is possible to use arrays of STaNDs to resolve larger number of photons. Here we treat the STaND as a perfect two-photon detector, and compare the PNR fidelity of N -element STaND arrays against N -element click/no-click SNSPD arrays. The probability of correctly resolving an n -photon input in an N -element SNSPD array follows $P_N^{\text{SNSPD}}(n|n) = \eta^n N!/[N^n(N-n)!]$ for $N \geq n$, i.e., no 2-or-more-photon hits on a single. For an N -element STaND array, we demand no 3-or-more-photon hits on a single element. For instance, neglecting the η^n term for all cases, $P_N^{\text{STaND}}(3|3) = 1 - 1/N^2$, $P_N^{\text{STaND}}(4|4) = 1 - \frac{1+4(N-1)}{N^3}$, $P_N^{\text{STaND}}(5|5) = 1 - \frac{1+5(N-1)+10(N-1)^2}{N^4}$, and so on ($N \geq \text{ceil}(n/2)$). Unfortunately, we have not reached a closed-form solution. Instead, we plot them numerically in Fig. 4-21 (assuming $\eta = 1$). On average, to achieve similar fidelity (e.g., 90% with $\eta = 1$), we need roughly 10 times more SNSPDs than STaNDs.

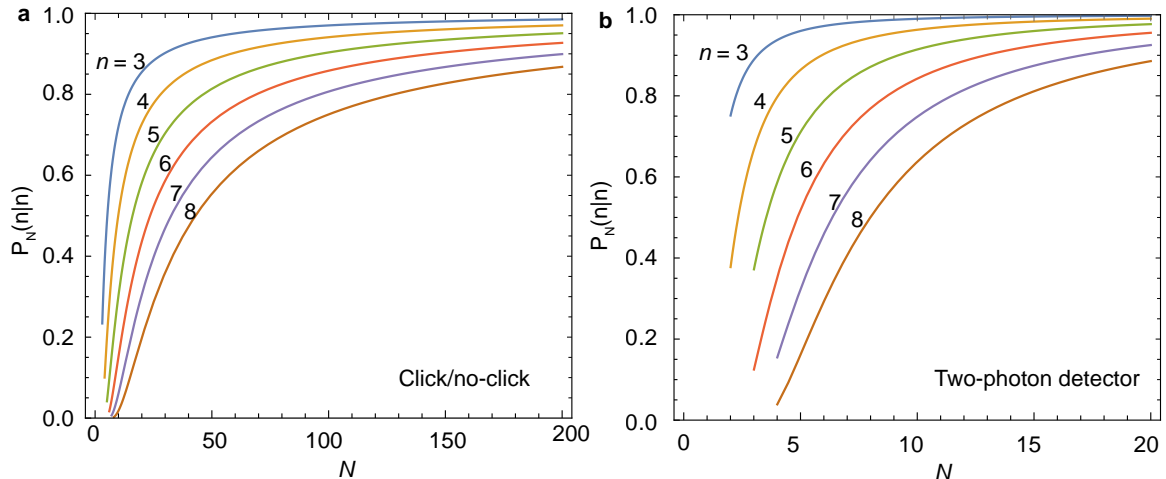


Figure 4-21: Comparison of resolving fidelity of large photon numbers using arrays of SNSPDs and STaNDs (note difference in x axis scales). Here, we assume unity detection efficiency. To include actual efficiency, a scaling factor of η^n needs to be multiplied to both cases.

4.10 Conclusion

In summary, we have demonstrated a STaND whose output amplitude directly encoded photon numbers. We observed up to five-photon responses, and used it to measure HOM interference directly. The PNR fidelity and dynamic range may be improved by using low-noise cryogenic amplifiers/comparators and tapers with higher input impedance. The STaND only required single-layer fabrication, and inherited the outstanding detector metrics from existing high-performance SNSPDs, including 16.1 ps FWHM timing jitter, 26.8 cps system dark count rate (1.68 cps device dark count rate), and sub-100-ns reset time. The taper inductance and footprint could be significantly reduced by using microstrip[89] or grounded coplanar waveguide designs. The current system efficiency ($\sim 5.6\%$) was limited by optical coupling, and could be readily improved by cavity integration and self-aligned fiber packaging[110, 109, 7]. With our ongoing effort on optimizing system efficiency and incorporating low-noise cryogenic readouts, we expect the STaND to find many immediate applications, such as heralding/rejecting multi-pair generation in SPDC, characterizing single-photon emitters, preparing/verifying non-classical state of light.

Chapter 5

A scalable coincidence detector based on superconducting nanowire transmission line

Coincidence detection of single photons is crucial in numerous quantum technologies and usually requires multiple time-resolved single-photon detectors. However, the electronic readout becomes a major challenge when the measurement basis scales to large numbers of spatial modes. Here, we address this problem by introducing a two-terminal coincidence detector that enables scalable readout of an array of detector segments based on superconducting nanowire microstrip transmission line. Exploiting timing logic, we demonstrate a 16-element detector that resolves all 136 possible single-photon and two-photon coincidence events. We further explore the pulse shapes of the detector output and resolve up to four-photon coincidence events in a 4-element device, giving the detector photon-number-resolving capability. This new detector architecture and operating scheme will be particularly useful for multi-photon coincidence detection in large-scale photonic integrated circuits.

In this chapter, we exploit the slow phase velocity of superconducting nanowire microstrip transmission lines to achieve time-delay multiplexing of SNSPDs. Materials presented in this chapter has been previously published and is reproduced from *Nat. Nanotechnol.* **13**, 596 (2018) [89].

5.1 Introduction

Single-photon detection plays a key role in quantum information processing, including modular quantum computing with trapped ions [111] and solid-state quantum emitters [112, 113, 114], photonic quantum walks and Boson sampling [115, 116, 117, 118], quantum simulations [119], and linear optical quantum computing [120]. Most of these applications rely on coincidence measurement of single or entangled photons over a large number of spatial modes and require an equal number of time-resolved single-photon detectors. Among various single-photon detectors [2], the superconducting nanowire single-photon detector (SNSPD) has become increasingly attractive because of its outstanding detector metrics [18, 7, 121, 11, 9] and feasibility of on-chip integration [122, 123, 14, 124, 125, 126, 10]. Traditional SNSPD arrays used for space communication [127], photon number resolution [128], and few-channel coincidence counting [125] adopt parallel readout of individual detector elements. However, scaling these arrays for coincidence counting over large numbers of channels presents formidable challenges, especially for the electrical readout [129].

A number of multiplexing schemes and device architectures have been developed to solve the readout problem. Row-column multiplexing is an efficient scheme but still requires $2N$ readout channels for N^2 pixels [23]. Another promising scheme is the frequency-division multiplexing, where SNSPDs are embedded in resonators operating at different radio-frequency (RF) tones [130, 24]. Though a common feed line can couple multiple resonators, each RF tone needs a demultiplexing circuit. Besides frequency-domain multiplexing, time-domain multiplexing has also been explored. Hofherr *et al.* demonstrated time-tagged multiplexing in a proof-of-concept two-element array [25], in which the signals from the two elements were separated in time using a delay line. While this approach only required a single readout line, the device dimension and array size were limited by the delay line design. More recently, we employed a time-tagged multiplexing to create a single-photon imager from a continuous nanowire delay line [40]. This imager resolves photon position but is only used to detect one photon at a time. Another architecture connects nanowires in

parallel and encodes the desired information in the amplitude of the electrical output, such as photon number [32] or position [131]. However, these detectors require on-chip resistors for biasing, and the array size is limited by the leakage current to the parallel branches.

Here we report on a two-terminal detector based on superconducting nanowire microstrip transmission lines that works as a scalable array. Unlike previous work [25, 40], this detector resolves the location of more than one photon and works naturally as a coincidence counter. With simple timing logic, we demonstrated the resolution of all 136 possible single- and two-photon events in a 16-element detector. With pulse shape processing, we resolved up to four-fold coincidence events and showed photon-number-resolving capability in a 4-element device. The microstrip transmission line used in the detector had a group velocity as low as $1.6\%c$ (where c is the speed of light in vacuum) and may allow denser packing compared to co-planar structures [40]. The detector was designed for integration on optical waveguide arrays and fabricated on a waveguide-compatible substrate material. We expect it to find immediate applications in large-scale on-chip coincidence detection for quantum information processing.

5.2 Architecture and operating principle

Figure 5-1 illustrates the basic architecture and operating principle of the detector. In our design, individual detecting elements were connected by nanowire delay lines, resulting in a one-dimensional detector array. Figure 5-1 shows a sketch of a 16-element (D_1 to D_{16}) array. Figure 5-1(b) panel (i) shows an SEM of a fabricated detector chain, and (ii) zooms to a delay line that connects two detector segments (iii). Each meandered delay line had a width of 300 nm, a period of $1.8\ \mu\text{m}$, and a total length of $429\ \mu\text{m}$. Each detector segment consisted of a pair of 80-nm-wide, $5\text{-}\mu\text{m}$ -long parallel nanowires. This detector segment design is known as a 2-element superconducting nanowire avalanche photodetector (2-SNAP) [132]. Compared to a standard hairpin nanowire [123], the 2-SNAP enhanced signal-to-noise ratio and provided relatively good impedance matching to the 300-nm-wide delay lines. To

make the nanowires into transmission lines, we capped the device area with a 450-nm-thick oxide spacer and 60-nm-thick gold ground plane on the top. Designing the isolated nanowires as transmission lines was essential for the delay-line-based detector: the transmission line guided the microwave signal along the nanowire with a slow propagation speed and minimized microwave coupling in the meander. The device design was intended for future integration with AlN photonic waveguide array (see Section 5.8). The blue shaded band in Fig. 5-1(a) panel (iii) marks the potential position for an optical waveguide.

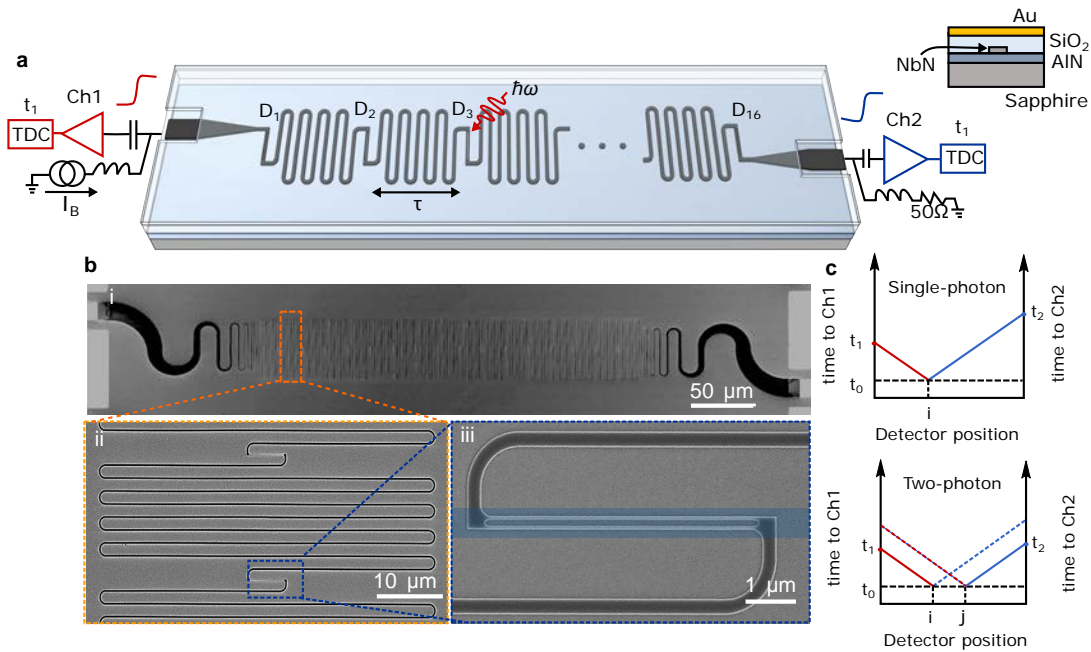


Figure 5-1: Device architecture and operating mechanism for the delay-line-multiplexed coincidence detector array. **a**, Device layout. The detector is a two-terminal array that connects a chain of single-photon detector segments using slow-wave nanowire delay lines. The nanowire was designed to be a microstrip waveguide with a dielectric spacer and top ground plane (see top right schematics). TT: time tagger. **(b)** Scanning electron micrograph (SEM) for a fabricated device. (i) A 16-element detector chain with impedance-matching tapers on the two ends; (ii) delay line formed by a 300-nm-wide meandered nanowire; (iii) a detector segment consisted of two 80-nm-wide parallel nanowires. The blue band marks the site for future waveguide integration. **c**, Illustration of the timing logic in the detector. t_0 is the photon arrival time; t_1 and t_2 are the times when the electrical signal arrives at Ch1 and Ch2, respectively.

To operate the detector, we biased it using a constant DC current and read out on

both terminals (Ch1 and Ch2) using room-temperature low-noise amplifiers [39, 40]. When the 2-SNAP was biased close to its critical current, the delay line was only biased at $\sim 50\%$ and therefore would not respond to incident photons.

Figure 5-1(c) illustrates the timing logic in the detector. In the single-photon regime (see the upper panel), only one segment fires at a time, following the timing logic as presented in Ref. [40, 25]. For instance, if a photon arrives on the i -th detector D_i at time t_0 and excites a pair of counter-propagating pulses, the left-propagating pulse will reach Ch1 at time $t_1 = t_0 + (i - 1)\tau$, where τ is the delay between two adjacent segments; and the right-propagating pulse will reach Ch2 at time $t_2 = t_0 + (N - i)\tau$, where N is the number of segments in the array. In this case, the arrival time of the photon can be derived from the sum of the two pulse times, $(t_1 + t_2)/2 = t_0 + (N - 1)\tau/2$, while the arrival location of the photon is determined from their difference, $(t_1 - t_2)/2\tau = i - (N + 1)/2$.

The timing logic is different for the two-photon case (see the lower panel in Fig. 5-1(c)). When two segments fire at the same time, each of them launches a pulse pair, but each readout channel will only identify the pulse edge from its nearest segment because the pulse width (ns) is significantly larger than the delay time (ps). So if D_i and D_j both fire ($i < j$), Ch1 will tag $t_1 = t_0 + (i - 1)\tau$, while Ch2 will tag $t_2 = t_0 + (N - j)\tau$. If t_0 is known, one can trace back both i and j . This method requires the knowledge of t_0 , which is available in many practical applications. For pulsed single-photon or photon-pair sources, the excitation laser gives t_0 ; in communication or computing, the reference clock gives t_0 as long as the timing window and timing jitter are smaller than τ .

5.3 Detector fabrication

Figure 5-2 shows the fabrication flow, and the step by step process is listed as follows:

1. The NbN film was deposited on an AlN-on-sapphire substrate (Kyma Technologies, Inc.) using DC magnetron sputtering at 840°C . The NbN deposition and nanowire patterning follows that described in Ref. [133, 121]. The AlN was

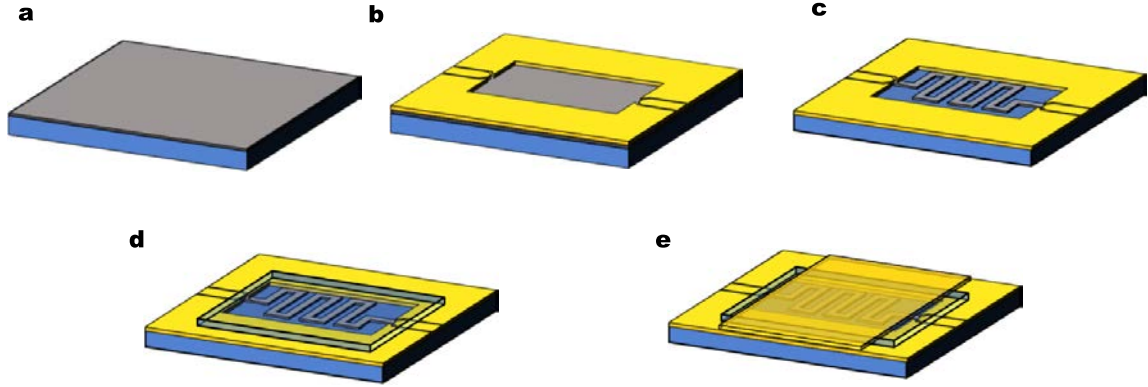


Figure 5-2: Fabrication process for the detector with microstrip delay lines. **a**, Sputtering NbN on an AlN-on-sapphire substrate. **b**, Defining bottom gold contact and alignment mark. **c**, Patterning NbN nanowires. **d**, Fabricating dielectric spacer. **e**, Putting top grounding plane.

c-axis oriented with a thickness of $200 \pm 5\%$ nm. The NbN film had a thickness of ~ 5 nm, critical temperature of 10.7 K, transition width of 1.63 K, sheet resistance of $510 \Omega/\text{sq}$, and residual resistance ratio of 0.85. More details on NbN on AlN were reported in [134].

2. The bottom electrical contact pads and alignment marks were defined using contact photolithography. Bilayer resists with PMGI SF9 and S1813 were used to facilitate lift-off. The metal layers (5 nm Ti/50 nm Au/5 nm Ti) were deposited using electron-beam evaporation and lifted off in acetone followed CD-26 dip and DI rinse.
3. The superconducting nanowires were patterned using electron-beam lithography (EBL). 4% hydrogen silsesquioxane (HSQ) was spin coated on the sample at 4 krpm for 1 min (~ 65 nm thick). A 125 keV EBL system (Elionix F125) was used to expose the resist. The beam current was 1 nA, and the dose was $3840 \mu\text{C}/\text{cm}^2$. The HSQ was developed in 25% TMAH for 2 min and rinsed with DI water. The HSQ pattern was transferred to the NbN film using reactive ion etching with CF_4 chemistry (He: CF_4 7 sccm: 15 sccm). The etching was at 10 mTorr, 50 W for 1 min 45 s.
4. A low contrast FOX process was used to define the dielectric spacer. Dow

Corning FOX-16 (flowable oxide, which is essentially high concentration HSQ) was spin coated at 3 krpm for 1 min and baked at 250°C for 2 min. The intended area (which covers all the nanowires) was exposed using EBL at 20 nA with a dose of 800 $\mu\text{C}/\text{cm}^2$, then developed in CD-26 for 70 s followed by rinsing in DI water. We measured the thickness of the spacer to be 450 nm using a surface profiler (Dektak).

5. The top grounding plane (5 nm Ti and 60 nm Au) was fabricated using an aligned photolithography followed by metal lift-off using a similar process as the bottom contact pads.

Figure 5-3(a) shows an optical micrograph of a fabricated unit cell. The chip had 9 cells, each cell hosted 4 detector chains, and each chain had 16 detector segments. The bottom Au contact pads (gray color) were designed to be 50 Ω CPWs, and directly transitioned to the NbN microstrip. Because of proximity effect and low resist contrast, the middle dielectric spacer (colored purple) had a natural slope on its edges, allowing the top ground to climb the step conformally. The top ground (colored yellow) was intentionally designed to extend outside the dielectric spacer to make contact to the bottom common ground.

5.4 Measurement setup

All measurements were performed in a pulse-tube-based cryostat at 3.0 K (Cryomech). Each detector was wire bonded to a printed circuit board and connected to room-temperature readout circuits through a pair of SMP cables (Ch1 and Ch2). The DC bias current was injected from Ch1 using a bias tee. The RF signal from each channel was amplified using a low-noise amplifier (MITeq AM-1634-1000, gain: 50 dB, bandwidth: 50 kHz-1GHz) and acquired using a 6 GHz real-time oscilloscope (Lecroy 760Zi) or counted using a 22 MHz universal counter (Agilent 53132A). The detector chip was back illuminated through a single-mode optical fiber (SMF-28e). The fiber was mounted on a piezo-stage (Attocube) for alignment and focusing (see

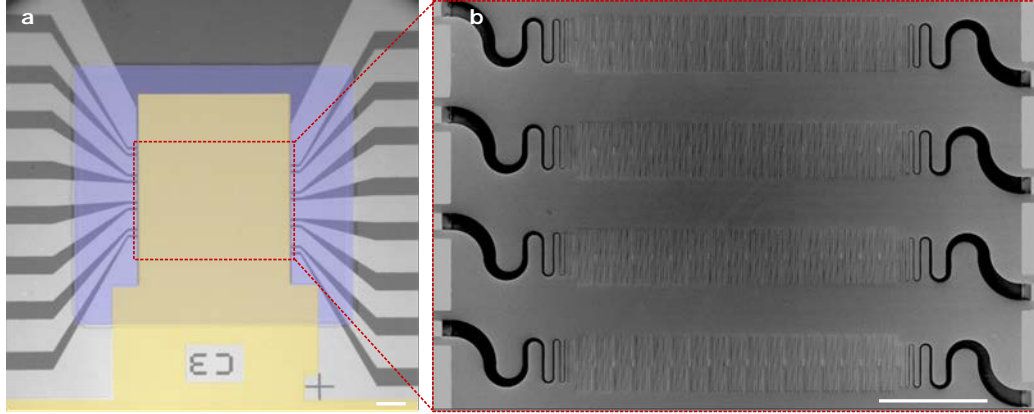


Figure 5-3: Micrographs of the fabricated device. **a**, Optical micrograph of the final fabricated device. The light gray area on the bottom is the gold contact pads, and the dark gray area is the substrate. The purple area marks the middle dielectric spacer. The yellow area marks the top gold grounding plane. The red box at the center marks the actual location of the superconducting nanowire. **b**, Scanning electron micrograph of the superconducting nanowires before putting on the dielectric spacer and top ground. 4 sets of detectors were fabricated in the same device area. Scale bar: 100 μm .

Fig. 5-4 for the packaging). When measuring the 16-element detector and probing the intrinsic timing response of the 4-element detector, a sub-picosecond fiber-coupled mode-locked laser (Calmar FPL-02CCF) was used. It has a center wavelength of 1550 nm and repetition rate of 20 MHz. During the experiment, the repetition rate was reduced to 500 kHz using an electro-optic modulator. When measuring the multiphoton response of the 4-element detector, a 1550 nm modulated diode laser was used (PicoQuant LDH-P-C-1550 laser head with PDL 800-B driver). The optical pulse was asymmetric, non-Gaussian, with a width of >200 ps (see Fig. 5-9(d) right panel for the pulse shape estimation). The repetition rate was set to 1 MHz. In both cases, the laser output was split into two paths, one to a fast photodetector (Thorlabs DET08CFC) as the timing reference, and the other to the detector through a calibrated variable attenuator (JDSU HA9) and a polarization controller.

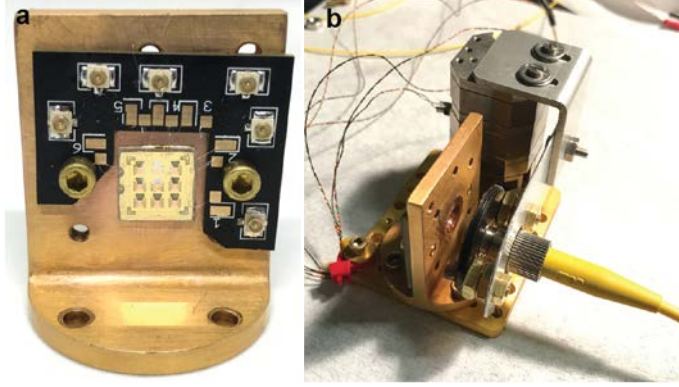


Figure 5-4: Packaging of the detector chip for back illumination. **a**, The detector chip was glued on a vertical holder with a hole in the center and wire bonded to a U-shaped PCB. **b**, A 1550 nm single-mode fiber was carried by a piezo-positioner (Attocube) to illuminate the chip from the back.

5.5 Demonstration of a 16-element detector

In this section, we present the measurement results from a 16-element detector, including timing distribution for both single- and two-photon detection, device efficiency, dark count rate, and maximum counting rate.

5.5.1 Multi-photon timing distribution

Figure 5-5 shows the measured timing distribution in a 16-element detector. 136 groups of detection events can be distinguished. The diagonal groups correspond to the 16 single-photon detection cases, and the off-diagonal groups correspond to the 120 (C_2^{16}) two-photon detection cases. Like all array-type photon-number-resolving detectors, the cases where two photons hit the same detector (with probability $O(1/N)$) cannot be resolved. The observed higher counting rate at $t_1 - t_0$ and $t_2 - t_0$ near zero (lower-left corner in the histogram) was because these detection groups included more three-or-more photon events. More details on “beyond two-photon detection” will be discussed later. The histogram was constructed from 1 million detection events, discretized here in bins of ~ 3 ps. The detector was measured at 3.0 K and flood-illuminated from the back of the chip using a 1550 nm sub-ps pulsed laser. It was biased at $14.5 \mu\text{A}$ with a switching current of $15.3 \mu\text{A}$.

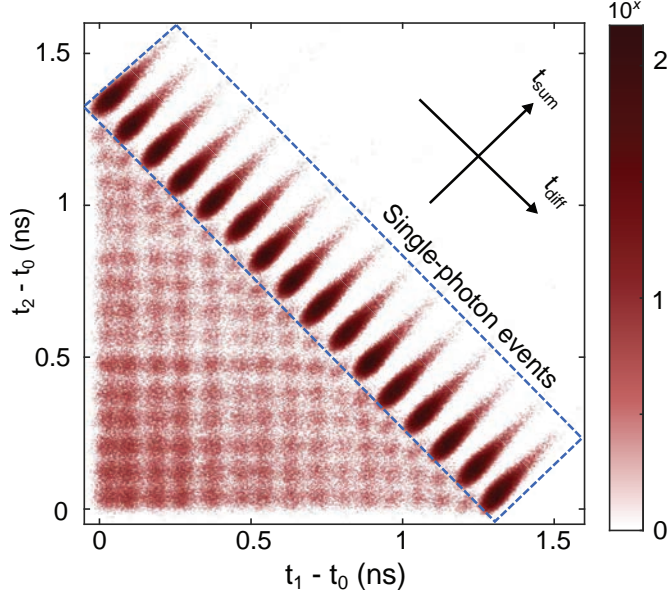


Figure 5-5: Measured timing distribution from the 16-element array that resolved all 136 distinguishable groups. The histogram was constructed from 1 million detection events. The color bar represents number of events per time bin (log scale) with a bin size of ~ 3 ps.

It is useful to introduce two characteristic timing variables: the sum time, $t_{\text{sum}} = (t_1 + t_2)/2 - t_0$, and the difference time, $t_{\text{diff}} = (t_1 - t_2)/2$. $(t_{\text{sum}}, t_{\text{diff}})$ forms a basis that is rotated relative to the $(t_1 - t_0, t_2 - t_0)$ basis by 45° . As illustrated in the space-time diagram shown in Fig. 5-1(c), in the single-photon regime, t_{diff} reveals the segment position, while t_{sum} is a constant regardless of the position.

5.5.2 Single-photon difference and sum time distribution

To characterize the delay line and the uniformity of each detecting segment, we operated the detector in the single-photon regime and constructed a 1-D histogram for t_{diff} . As shown in Fig. 5-6(a), the difference time histogram consisted of 16 Gaussians. The full-width at half-maximum (FWHM) was 20.3 ± 0.6 ps (average value with 1σ uncertainty), and the standard deviation of the peak amplitudes was 6% of its mean.

The $429\text{-}\mu\text{m}$ -long delay line between adjacent detectors created an 86.8 ± 0.3 ps delay, corresponding to a signal propagation speed of $1.6\%c$. The slow group velocity was due to the high kinetic inductance of the superconducting nanowire and large

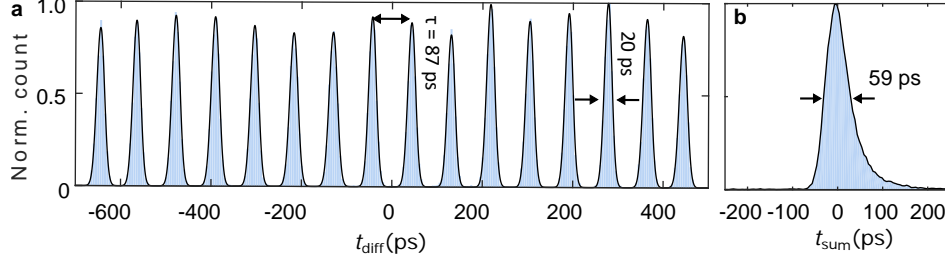


Figure 5-6: 1-D histogram of the difference time ($t_{\text{diff}} = (t_1 - t_2)/2$) and sum time ($t_{\text{sum}} = (t_1 + t_2)/2 - t_0$) when the detector was operating in the single-photon regime. The efficiency of the segments was uniform with a standard deviation of 6% of its mean value. The average FWHM differential jitter was 20 ps and timing delay between adjacent segments was 87 ps. The FWHM sum jitter was 59 ps.

capacitance offered by the top ground plane placed 450 nm above the nanowire [135]. The characteristic impedance and phase velocity of the nanowire transmission line was estimated using a distributed circuit model, where $Z_0 = \sqrt{\mathcal{L}/\mathcal{C}}$ and $v_{\text{ph}} = 1/\sqrt{\mathcal{L}\mathcal{C}}$. Here, $\mathcal{L} = \mathcal{L}_k + \mathcal{L}_m \approx \mathcal{L}_k$, where \mathcal{L}_k and \mathcal{L}_m are the kinetic and Faraday inductances per unit length, respectively; and \mathcal{C} is the capacitance per unit length. From numerical simulation, we estimated $\mathcal{L} \approx 0.3 \text{ mH/m}$ ($0.3 \text{ nH}/\mu\text{m}$) and $\mathcal{C} \approx 128 \text{ pF/m}$ ($0.128 \text{ fF}/\mu\text{m}$).

Fig. 5-6(b) shows the distribution of t_{sum} , which had a FWHM sum jitter of 59 ps. The sum jitter corresponds to the detector's timing accuracy in determining photon arrival time.

5.5.3 Detector efficiency and dark count rate

Figure 5-7 shows the normalized photon count rate (PCR) and dark count rate (DCR) as functions of bias current (I_b). At 780 nm illumination, the PCR was saturated, indicating high internal quantum efficiency. The increased PCR near I_{SW} at 780 nm may be due to (1) triggering of the delay line by the high energy photons when flood illuminated, (2) capacitive charging of the AC coupled amplifier at high count rate which increases the effective bias [136], or (3) increased dark count rate under illumination which in turn increases measured photon count rate [137].

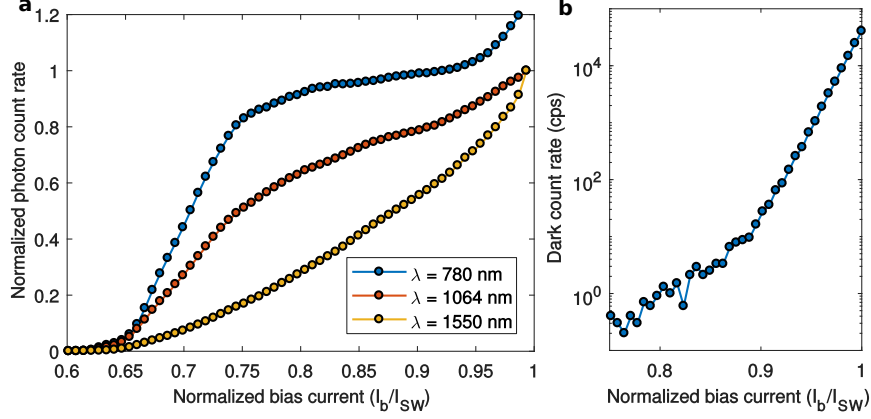


Figure 5-7: Detector efficiency and dark count in the 16-element detector. **a**, Normalized photon count rate (PCR) vs. normalized bias current under different photon energies. The PCR for 1064 nm and 1550 nm was normalized to their maximum count rates, while the PCR for 780 nm were normalized to the “plateau” region, and the value was chosen to be the average of the points near minimum $\frac{dPCR}{dI_b}$. **b**, Dark count rate vs. normalized bias current.

5.5.4 Maximum counting rate

Figure 5-8 shows the counting rate measurement of the 16-element detector. At 3 dB efficiency suppression point, the maximum count rate was 4.8 MHz.

The reset time of the detector is limited by the kinetic inductance of the nanowire [101]. The maximum count rate can be roughly estimated as $R_{load}/[3N(L_{det} + L_{delay})] = O(1/N)$, where N is the number of segments, L_{load} is the load impedance (50Ω in our case), L_{det} and L_{delay} are the inductance for each detector segment and each delay line.

5.6 Timing and photon statistics analysis in a 4-element detector

To reduce analysis complexity, we studied in detail the timing property and photon counting statistics on a widely separated 4-element (D_1 - D_4) detector array. The 4-element detector had the same design as the 16-element device but with a five times longer delay between adjacent detector segments.

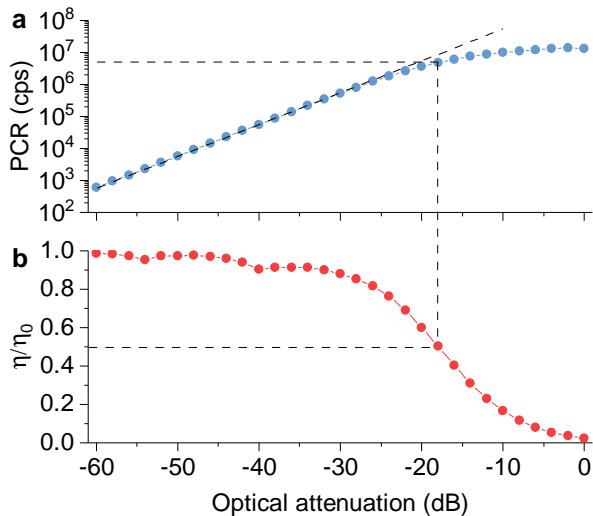


Figure 5-8: Maximum count rate of the 16-element detector. **a**, Measured photon count rate (subtracted dark count rate) as a function of optical attenuation. **b**, Normalized detection efficiency as a function of optical attenuation. The maximum count rate was measured to be 4.8 MHz at the 3 dB suppression point for the detection efficiency. The light source was a superluminescent diode with a center wavelength at 1550 nm. We used the setup described in Ref. 6 to avoid capacitive charging at the amplifier.

5.6.1 Pulse shapes of single-photon events

Figure 5-9(a) shows 200 pairs of electrical pulses from the detector when illuminated using a sub-ps pulsed laser in the single-photon regime. The pulses were aligned according to the timing reference from the laser. The dashed line marks the trigger level for time tagging, where the four groups of pulses were separated by ~ 426 ps.

Depending on the position of the firing segment, the output pulse shapes were different. This position dependence was due to signal reflections in the nanowire and taper. Besides the major impedance mismatch between the nanowire ($1.5 \text{ k}\Omega$) and the readout (50Ω), the resistive hotspot (a dynamic resistance at $\text{k}\Omega$ scale) also contributed to reflections. The reflections caused distinct pulse shapes for each detection case. For instance, the pulses from D_1 on Ch1 had two rising edges separated by ~ 3 ns, which matched the round trip time in the nanowire. Due to symmetry, pulses from D_4 on Ch2 also had the same feature. Impedance matching tapers could in principle be used to minimize reflections, enhance signal levels, and provide faster

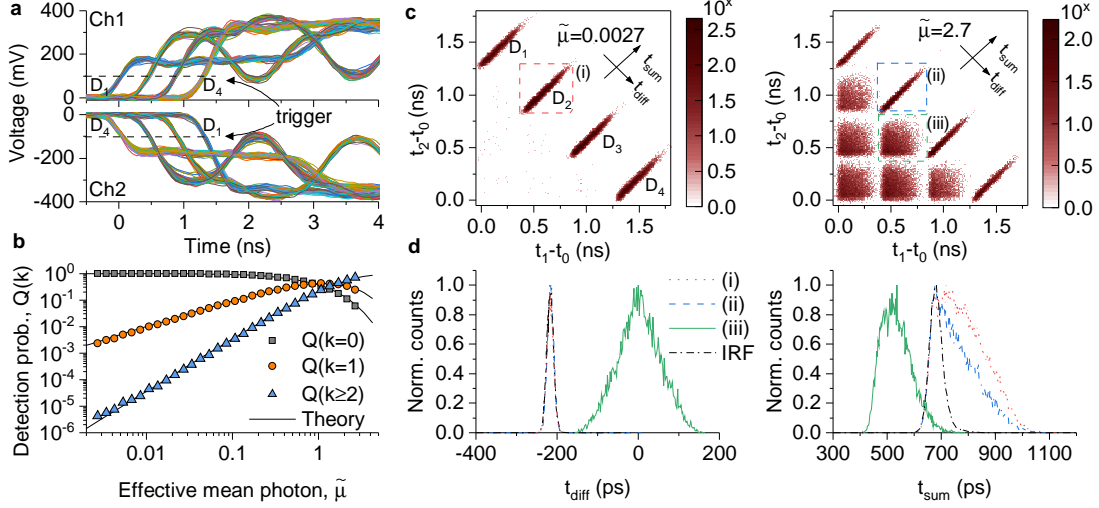


Figure 5-9: Timing logic based two-photon detection in a 4-element detector chain. **a**, Electrical pulses from a 4-element device when illuminated with a sub-ps pulsed laser in the single-photon regime. The dotted lines mark the trigger level for time tagging. **b**, Photon counting statistics under different input powers. $\tilde{\mu} = \eta\mu$ is the effective mean photon per pulse which included detector efficiency. $Q(k)$ is the probability that k segments fire. The symbols are measurement results, and for comparison, the lines are calculated from a theoretical model based on the detector conditional probability and the Poisson distribution of the coherent state input. **c**, Measured timing distribution for $\tilde{\mu} = 0.0027$ (left) and $\tilde{\mu} = 2.7$ (right) when illuminated using a laser with pulse width of ~ 200 ps. The time bin in the plot is 10 ps and color bar is in log scale. **d**, Histogram of the difference (left) and sum (right) time for 4 representative groups of detection events. (i), (ii): D_2 fires under weak and strong illumination, respectively; (iii): D_2 and D_3 fire simultaneously. (i-iii) are labeled in **c** and were measured using a 200-ps pulsed laser. IRF: instrument response function of D_2 probed using a sub-ps pulsed laser in the single-photon regime, showing a FWHM differential jitter of 20 ps and sum jitter of 56 ps.

rising edges to reduce timing jitter [40]. In our case, instead of performing a perfect impedance matching with a centimeter long taper, we used a short taper with high cut-off frequency. Though the imperfect impedance matching resulted in large reflections, it was possible to trigger at a lower threshold to capture only the initial part of the rising edge. Also, as will be shown later, the distinctive pulse shapes caused by reflection actually enabled us to resolve more than two photons.

5.6.2 Photon counting statistics

We verify the detector's ability to resolve single- and two-photon events by performing a photon-statistics measurement of a coherent source. The measured photon statistics $Q(k)$ are related to the source distribution $S(m)$ by $Q(k) = \sum_{m=0}^{\infty} P(k|m)S(m)$, where $P(k|m)$ is the conditional probability that k detector segments click given m photons in the source. The laser diode serving as the input in our experiment follows the Poisson distribution, $S(m) = \sum_0^{\infty} \frac{\mu^m}{m!} e^{-\mu}$, where μ is the mean photon number. Figure 5-9(b) shows the measured $Q(k)$ when the effective mean photon per pulse of the input laser $\tilde{\mu}$ was attenuated from 2.7 to 0.0027 using a calibrated variable attenuator. The measurement result (symbols) matched our theoretical model (lines, see Section 5.6.4 for the derivation). Here, $\tilde{\mu} = \eta\mu$ included detector and coupling efficiencies. The value of $\tilde{\mu}$ was estimated by fitting the measured zero-photon probability to $e^{-\tilde{\mu}}$ based on the known attenuation value. For each mean photon number, we accumulated 100,000 detection events (not including non-click events) and extracted the one- and two-photon detection probabilities using the timing logic. The zero-photon probability was measured separately by counting the number of non-click events over 50,000 photon pulses. Doing so ensured enough samples for low probability events and minimized measurement shot noise, while avoiding the unnecessarily large number of measurements for high probability events.

5.6.3 Timing resolutions

Figure 5-9(c) shows the timing distribution for $\tilde{\mu} = 0.0027$ (left panel) and $\tilde{\mu} = 2.7$ (right panel). When $\tilde{\mu} = 0.0027$, the detector was operating in the single-photon regime, and only the 4 diagonal groups were present. When $\tilde{\mu} = 2.7$, the 6 off-diagonal groups became prominent. Here, each 2-D histogram was constructed from $\sim 100,000$ detection events. In these measurements, the probing laser had a FWHM pulse width of ~ 200 ps. Therefore, the spread of each detection group in the 2-D histogram was significantly wider than that shown in Fig. 5-5.

The spread of the timing distribution was affected by both the device timing

jitter and the laser pulse width. As shown in Fig. 5-9(c), the single-photon events, compared to the two-photon events, had a slimmer distribution in the t_{diff} axis. The timing uncertainty for each time tag consists of 3 parts: $\sigma_{t_{1,2}-t_0}^2 = \sigma_{\text{ph}}^2 + \sigma_{\text{det}}^2 + \sigma_e^2$, where σ_{ph} is the photon arrival jitter, i.e. the photon could hit the detecting segment at anytime in the optical pulse duration; σ_{det} is the detector intrinsic jitter, i.e. the absorbed photon could trigger a voltage pulse with a variable time delay; and σ_e is the electrical jitter, i.e. the electrical noise would fluctuate the trigger point on pulse rising edge [138, 87]. The photon arrival jitter introduced by the laser pulse width mimics the uncertainty of the timing reference in many real applications, and restricts the minimum delay required to distinguish photon events from adjacent detectors.

We extracted the timing distributions for 4 representative groups of detection events and compared them in Fig. 5-9(d). The 4 groups are (i) weakly illuminated single-photon detection on D_2 , (ii) strongly illuminated single-photon detection on D_2 , (iii) two-photon detection where D_2 and D_3 both fire, and (iv) single-photon detection on D_2 probed using a sub-ps pulsed laser instead of a ~ 200 ps modulated laser diode. The last group is labeled as IRF (instrument response function) in the figure, because the laser pulse width had negligible contribution to the measured timing jitters. For all of the single-photon detection events, the differential timing jitter (left panel) only contained the electrical jitter (σ_e) since both the photon arrival jitter (σ_{ph}) and detector intrinsic jitter (σ_{det}) were canceled (see curves i, ii, and IRF). The measured FWHM differential jitter here was 20 ps. For the two-photon detection cases, however, two segments could absorb photons at different times due to the finite optical pulse width, so the differential jitter also contained the photon arrival jitter (σ_{ph} , see curve (iii)). For the sum jitter (right panel), the IRF shows an intrinsic FWHM sum jitter of 56 ps, which was primarily electrical jitter and detector intrinsic jitter. This value is consistent with our previous results in an NbN SNSPD on AlN substrate [133]. It is noticeable that under strong illumination (ii and iii), the sum jitter became narrower compared to that in the weak illumination case (i). This effect is due to the higher probability of detecting a photon in the early part of a strong optical pulse and is often referred as “pile-up.” [139]

5.6.4 Derivation for photon counting statistics

In the generic case, when an optical mode illuminates on an N -element detector, each photon has probability c_i of reaching detector D_i with a detection efficiency η_i . c_i depends on the spatial mode of the input field, while η_i is intrinsic to the detector. To simplify the modeling, we assumed a uniform detection efficiency for all elements (i.e. $\eta_i = \eta_j = \eta$). This assumption is reasonable based on our experimental characterization. We measured the detection efficiency distribution by driving the probing fiber far away from the device and uniformly illuminating the detector. For both the 4-element and 16-element detector chains, the standard deviation in η_i was $< 6\%$ of its mean (see Fig. 5-6(a) and Fig. 5-10). Under this assumption, we treated each segment as a perfect detector with unity efficiency and incorporated the actual detector efficiency to the input field, which makes the input mean photon number $\tilde{\mu} = \eta\mu$. Here, we also included coupling efficiencies to μ so that $\sum c_i = 1$.

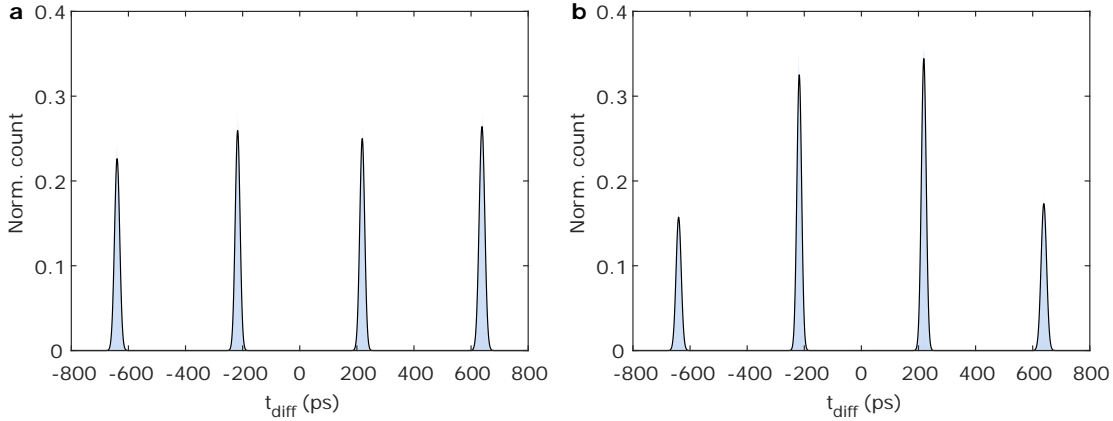


Figure 5-10: **Counting rate distribution in the 4-element detector.** **a**, When the probing fiber was far away from the detector, all the segments were illuminated uniformly, and they have a relatively uniform counting rate with a ratio of [0.2263, 0.2595, 0.2500, 0.2642]. **b**, When the fiber was focused at the center of the detector, the middle two segments had a higher counting rate, and the counting ratio was [0.1573, 0.3252, 0.3443, 0.1732]. This ratio was used as c_i in the photon statistics modeling.

For $\eta_i = 1$ and $\sum c_i = 1$, the conditional probability for m input photon and k

detector output, $P(k|m)$, can be evaluated as

$$\begin{aligned}
P(k|m) &= \sum_{l_1, l_2, \dots, l_N=0}^m C_{l_1}^m c_1^{l_1} \times C_{l_2}^{m-l_1} c_2^{l_2} \times \dots \times C_{l_N}^{l_N} c_N^{l_N} \\
&= \sum_{l_1, l_2, \dots, l_N=0}^m m! \times \frac{c_1^{l_1}}{l_1!} \times \frac{c_2^{l_2}}{l_2!} \times \dots \times \frac{c_N^{l_N}}{l_N!}
\end{aligned} \tag{5.1}$$

where l_i denotes the number of photons arriving on detector D_i ; $\{l_1, l_2, \dots, l_N\}$ has k non-zero terms and $\sum l_i = m$; $C_y^x = \frac{x!}{y!(x-y)!}$ is the combination operation. This expression can be evaluated numerically with $O(m^N)$ complexity, which is tractable for a 4-element detector. In the experiment, c_i 's were characterized by measuring the counting distribution in the single-photon regime (see Fig. 5-10 for the measurement of c_i 's).

5.7 Beyond two-photon detection

Two time tags can only resolve up to two photons. When 3 segments fire simultaneously, each readout channel will only register the rising edge from its nearest segment, and the signal from the middle segment will be ignored. For instance, in the 4-element detector, when D_2 , D_3 , and D_4 fire together, it will produce the same time tags as D_2 and D_4 firing simultaneously. This ambiguity, however, may be eliminated by processing the pulse shapes.

5.7.1 Fingerprints

Figure 5-11 shows traces of 100 pairs of detector pulses from the events where D_2 and D_4 fired (orange traces) or D_2 , D_3 , and D_4 fired (blue traces). Despite the large photon-arrival jitter from the ~ 200 -ps pulsed laser, these detector pulses have distinct signatures that allow them to be distinguished (e.g. the opening eye marked in Fig. 5-11). In principle, due to the reflections in the nanowire, each detection event should have its own fingerprint in the output pulse shape. By learning and discriminating these pulse shapes, one could resolve all events without ambiguity. Next, we show a

complete list of all observed pulse shapes and their fingerprints.

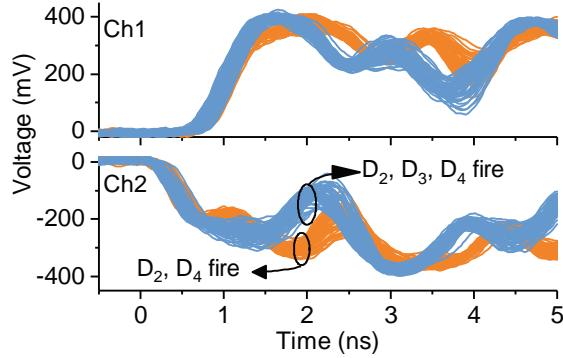


Figure 5-11: Traces of 100 pairs of detector pulses, corresponding to detection events where D_2 and D_4 fired, or D_2 , D_3 , and D_4 fired. These events are indistinguishable based on timing logic since they have identical time tags, but can be resolved from their pulse shapes.

5.7.2 Full list of pulse shapes and identified fingerprints

In total, there are 15 observed pulse shapes from the 4-element array, including 4 single-photon cases, 6 two-photon cases, 4 three-photon cases, and 1 four-photon case. Fig. 5-12 shows the averaged pulse shapes. As we can see, many pulses share the same rising edges (i.e. giving the same time tags), but start to diverge after about 400 ps to a few ns. This time scale is close to the delay time between adjacent detecting elements (426 ps), and is consistent with our hypothesis that the distinct pulse shapes from different detection events are caused by reflections from the hotspots and terminals in the nanowire. Moreover, the pulse shapes deviate further after more reflections, forming distinct ripples in the falling edge.

We separate the observed pulse shapes into 4 categories: (1) single-photon events (Fig. 5-13), where only 1 detector fires; (2) unambiguous two-photon events (Fig. 5-14), where 2 adjacent detectors fire; (3) ambiguous two-photon events (Fig. 5-15), where a detector and its next-nearest neighbor fire, leaving an ambiguity of whether the middle detector fires; and (4) ambiguous two, three, and four-photon events (Fig. 5-16), where D_1 and D_4 fire, leaving four possible situations (D_1D_4 , $D_1D_2D_4$,

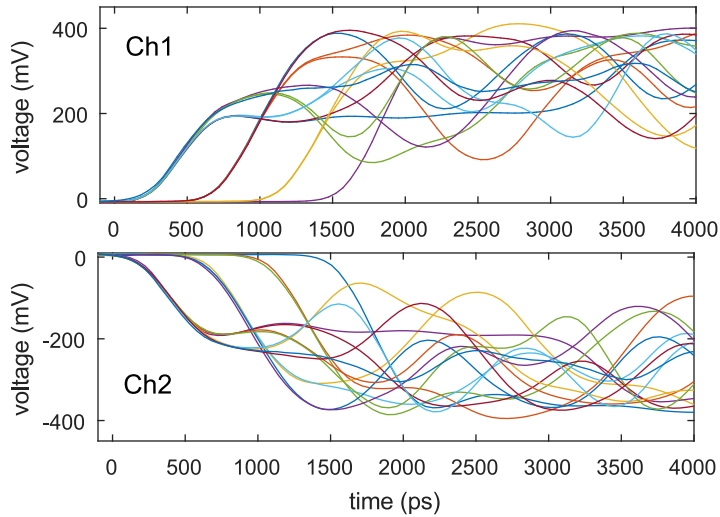


Figure 5-12: Averaged pulse shapes for all detection cases measured in the 4-element array. The upper panel shows the output pulses from Ch1, and the lower panel shows the output pulses from Ch2, which has the opposite polarity.

$D_1D_3D_4$, and $D_1D_2D_3D_4$).

Different from the clean averaged pulse shapes shown in Fig. 5-12, the single-shot waveforms have more variation and noise. In the current measurement, the variation was primarily due to the photon arrival jitter. Given the 200 ps laser pulse width, when multiple detectors fire, the hotspot formation/growth in one detector could delay another by as long as 200 ps. This variation can be seen in the jitter of the rising edge. More importantly, this initial time variation will further affect the reflection dynamics in the nanowire, especially when the two detectors are nearby. When the photon-arrival jitter is low, other effects, such as the avalanche process in the SNAP [140, 88] or multiphoton absorption on the same pixel [141], may also lead to variations in the output pulses.

5.7.3 Reconstructing photon statistics from pulse shape analysis

In Fig. 5-17 we demonstrated the capability of resolving up to four photons using the 4-element detector through pulse shape analysis. The input optical field was

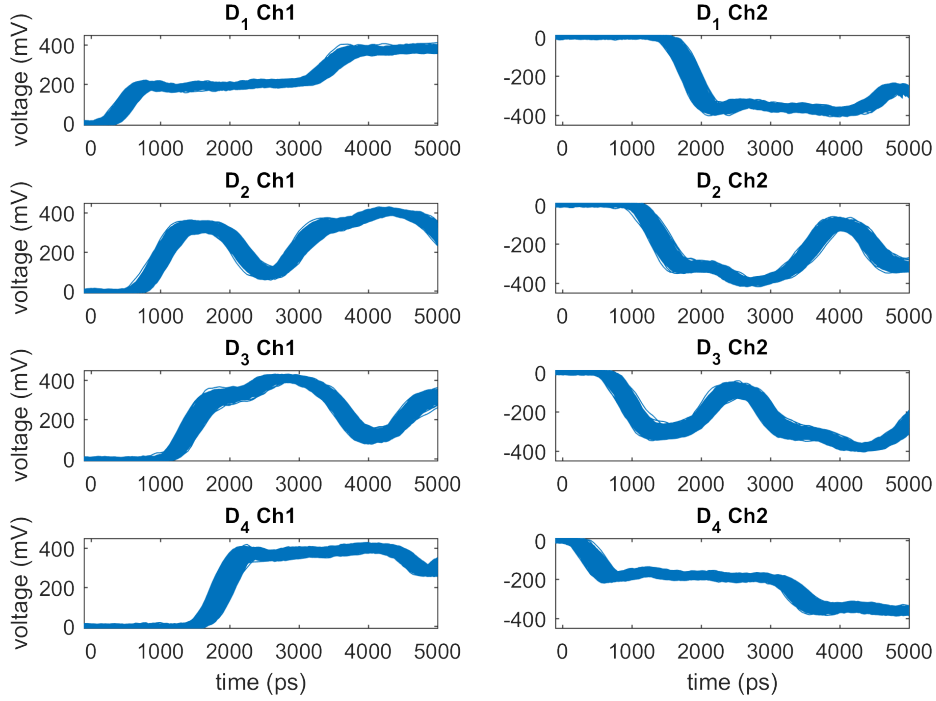


Figure 5-13: **Detector pulses for all single-photon cases.** Left panels show output pulses from Ch1, and the right panels show output pulses from Ch2, which have opposite polarities.

attenuated from an effective mean photon per pulse of 2.7 to 0.27. The maximum effective mean photon number was mainly limited by the sparse and small active area of the detector ($< 10^{-5}$ of the illumination area), the unpolished backside of the chip (scattered $\sim 60\%$ of the light), and illumination power ($\sim 4 \times 10^6$ photons per pulse). For each measured attenuation level, we acquired 50,000 pairs of detector pulses. By analyzing the pulse shapes, we discriminated all 15 combinations of detection cases and sorted them into one-, two-, three-, and four-photon events. The zero-photon probability was measured in the same way as in Fig. 5-9(b).

5.8 Discussions on optical coupling and scalability

The detection efficiency is the product of the internal quantum efficiency (η_{int}) and optical absorption (η_{abs}). The detector in our experiment was broadband responsive and had saturated internal quantum efficiency at 780 nm wavelength (see Fig. 5-7). Based on our previous results [133], a 60-nm-wide 2-SNAP using the same material

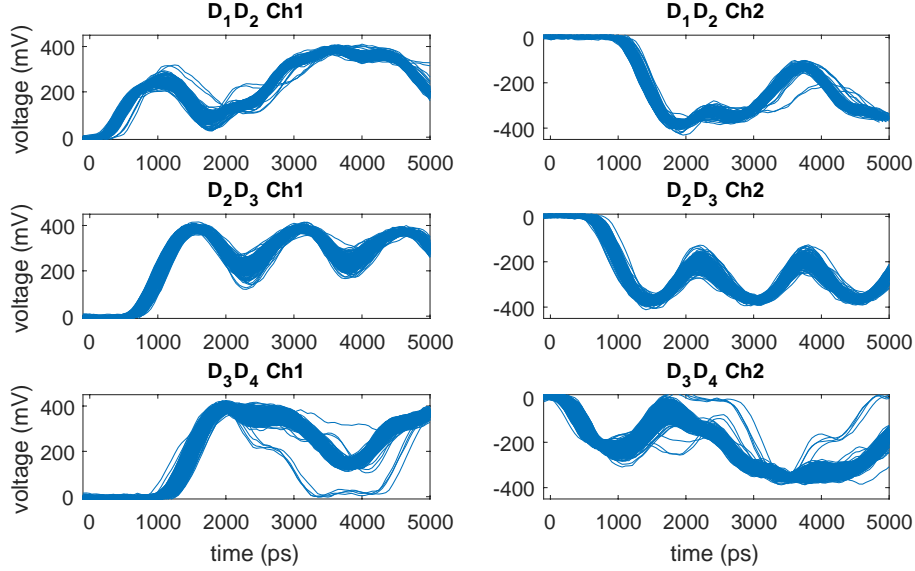


Figure 5-14: Detector pulses for unambiguous two-photon events. These two-photon detection events originated from adjacent detectors. In these cases, the timing logic on its own was sufficient to determine which two detecting elements fired without ambiguity, since no detecting elements in between could fire. We noticed some irregular pulse shapes for D_1D_2 and D_3D_4 events, but the reason was not completely understood yet.

and substrate can saturate at 1550 nm. The optical absorption can in principle reach unity when the detector is integrated on an optical waveguide [142, 123]. Simply etching the AlN substrate into a $450\text{ nm} \times 200\text{ nm}$ ridge waveguide, the 80-nm-wide 2-SNAP will have an absorption rate of $1.15\text{ dB}/\mu\text{m}$ for the transverse electric (TE) mode at 637 nm wavelength, which corresponds to the zero-phonon line of nitrogen vacancy centers in diamond. Figure 5-18 shows the numerical simulation for the waveguide mode and absorption rate. To achieve $>90\%$ absorption, the 2-SNAP needs to be $8.7\text{ }\mu\text{m}$ long. Adding a reflector or photonic crystal cavity on the waveguide can further reduce the length [143]. The ability to control absorption by changing the nanowire length can be used to cascade multiple partially absorbing detector chains in parallel on an optical waveguide array. This method can be used to resolve multi-photons in the same mode/waveguide.

The microstrip architecture used here offers significant advantages. When used as a free-space or fiber-coupled detector, the ground plane and dielectric spacer can form

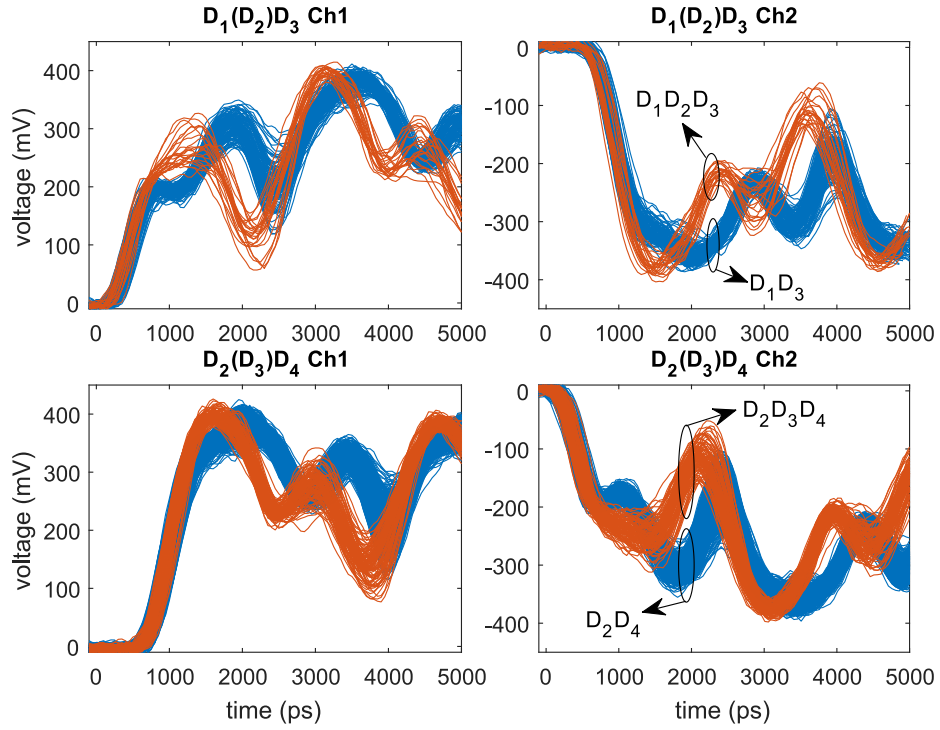


Figure 5-15: Detector pulses for ambiguous two-photon events. The circles indicate the fingerprints used to distinguish the events.

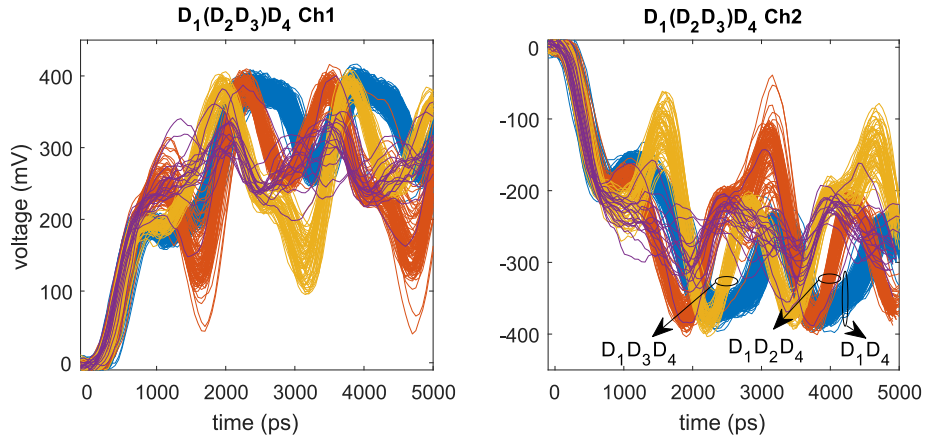


Figure 5-16: Detector pulses for ambiguous two, three, and four events. The circles indicate the fingerprints used to distinguish the events. We counted $D_1D_2D_3D_4$ events (purple) by identifying pulses that do not match the other three fingerprints.

an optical cavity to enhance absorption [109]. Compared to co-planar waveguides, the microstrip can be meandered with a higher fill-ratio without having light-absorbing ground plane around the nanowire, which is suitable for high-efficiency single-photon imagers [40].

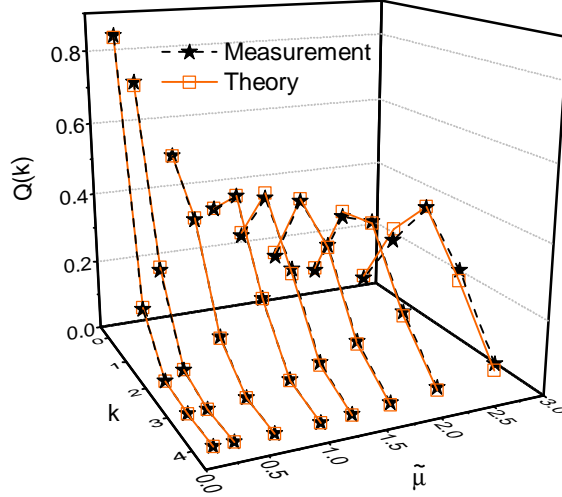


Figure 5-17: Resolving up to four photons based on pulse shape processing. Measured photon statistics $Q(k)$ for k up to 4 under coherent source illumination with mean photon per pulse $\bar{\mu}$ from 0.27 to 2.7. 50,000 pairs of detection pulses were processed for each mean photon number, and the error of each data point was limited by the measurement shot noise.

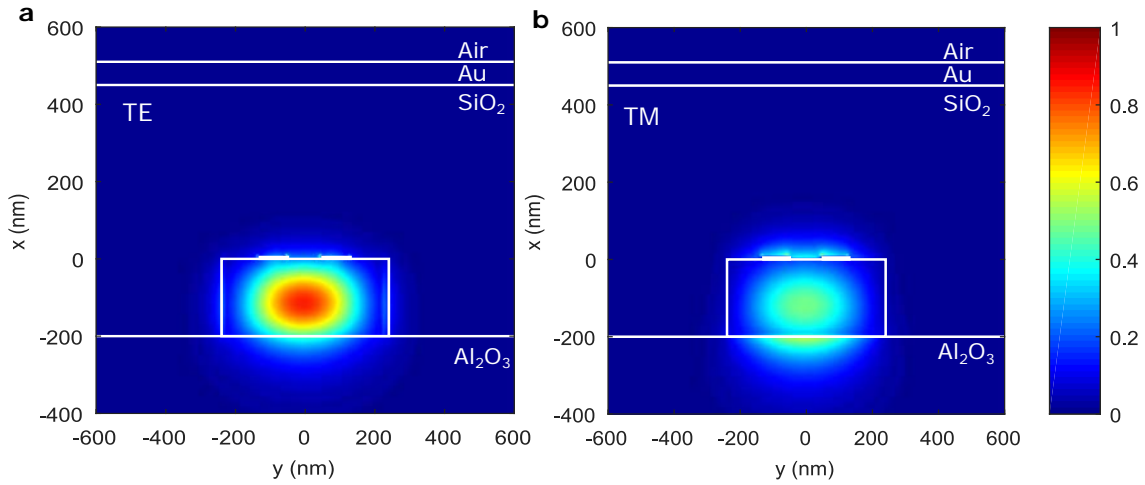


Figure 5-18: Calculation of the optical absorption in the superconducting nanowire when integrated on waveguide. The mode pattern (normalized $|\mathbf{E}|^2$) for a $450 \text{ nm} \times 200 \text{ nm}$ AlN waveguide with integrated 2-SNAPs at 637 nm wavelength. **a**, Transverse electric mode. $n_{\text{eff}} = 1.86 + 0.0134i$, and absorption rate is $1.146 \text{ dB}/\mu\text{m}$. **b**, Transverse magnetic mode. $n_{\text{eff}} = 1.83 + 0.0085i$, and absorption rate is $0.73 \text{ dB}/\mu\text{m}$. The simulation was performed using Lumerical MODE Solutions.

The number of segments in the detector can be increased without additional biasing/readout resources. However, the maximum counting rate will decrease due to the kinetic inductance limit [101]. Our current 16-element detector had a maximum

counting rate of 4.8 MHz (see Fig. 5-8). With increasing segments, the timing logic remains simple, but the pulse shape analysis may become challenging. An accurate physical and mathematical model may be needed to predict the detailed pulse shapes [86].

The current device with relatively small active area was designed for future waveguide integration. To implement an array of large-area detectors for free-space or fiber coupling, the detecting segment needs to be designed as an impedance matched meander to allow uninterrupted propagation of electrical signals along the detector chain. However, due to the large kinetic inductance associated with each detecting segment, the reset time will then become long. Some potential solutions to this issue include using a high-impedance readout to reduce the L/R time constant, or using an AC/pulsed bias to gate the detector through impedance matched terminals.

5.9 Conclusions

In conclusion, we have developed a scalable coincidence detector based on superconducting nanowires. We engineered the nanowire to a microstrip transmission line with a signal speed as low as $1.6\%c$. By varying the width at different sections, the nanowire serves either as a photon-sensitive detector segment or a compact delay line. The timing-logic operation is ideal for two-photon coincidence counting over large numbers of spatial modes, while the pulse-shape processing can be used for higher-order coincidence measurements in relatively small arrays. The device architecture is suitable for integration on optical waveguides and cavities. With increasing number of detector segments, we expect it to provide a practical solution for implementing large-scale photonic quantum information processing systems.

Chapter 6

Progress on waveguide-integrated 65-channel detector array

Integrated photonics is a promising platform to realize large-scale quantum information processing. A full integrated quantum processor requires 3 main components: (1) solid-state single-photon sources and memories; (2) low-loss and high-fidelity photonic circuit elements, such as waveguides, beam-splitters, and modulators; and (3) high-efficiency single-photon detectors. In this chapter, we describe our progress and preliminary results of implementing a delay-line-multiplexed 65-element SNSPD array on Si-on-insulator waveguides. An on-chip detector array at this scale may enable many interesting quantum simulation tasks.

6.1 Introduction

SNSPDs are made from a single layer of material and are suitable for waveguide integration. Waveguide-integrated SNSPDs absorb light evanescently and can achieve high on-chip detection efficiency with a compact size (10s of μm long) [142, 123]. With proper cavity designs, coherent perfect absorption can be achieved with even shorter detector lengths [143, 10]. Furthermore, small device footprints can reduce the detectors' reset times and suppress background counts.

Waveguide-integrated SNSPDs have been demonstrated in a number of material

systems, such as Si [123, 143], SiN_x [121, 124], diamond [126, 144], GaAs [122], and LiNbO_3 [145, 146, 147] (not measured directly on waveguides). Among various photonic platforms, silicon-on-insulator (SOI) is currently the most popular one. It has high index contrast, which allows dense packing, and can be produced in large scale from photonic foundries.

Practical photonic simulations [119], such as quantum walk [115, 148] and Boson sampling [117, 116], require large arrays of single-photon detectors. Though photonic circuits now have achieved impressive size and complexity [149, 150], the number of detectors remains an obstacle to scale. So far, the largest array size of waveguide-integrated detectors is 8 [151]. To scale up, beside challenges in fabrication yield [125], the electrical readout is a major problem.

Here, we report our progress on implementing a 65-element SNSPD array on SOI photonic integrated circuits (PIC). We designed the PIC for a quantum walk (of correlated photons) experiment [115]. The detector array is multiplexed using microstrip delay lines and only requires one pair of RF cable and readout electronics. We have developed a fabrication process for this hybrid, multi-layered system. By flood illuminating the entire chip, we have observed all 65 detectors working.

6.2 Device architecture

In this section, we describe the design of the PIC and SNSPD array, and show the theory and simulations of continuous-time quantum walk that may be performed using this device.

6.2.1 Device overview

Figure 6-1 illustrates the device architecture. Similar to Chapter 5, the detector segments are separated by slow-wave delay lines, but now they sit on top of a waveguide array directly.

Figure 6-2 shows micrographs of a fabricated device. Figure 6-2(a) shows the overall device (there are 4 such units in a $1\text{ cm} \times 1\text{ cm}$ chip). The detector area was

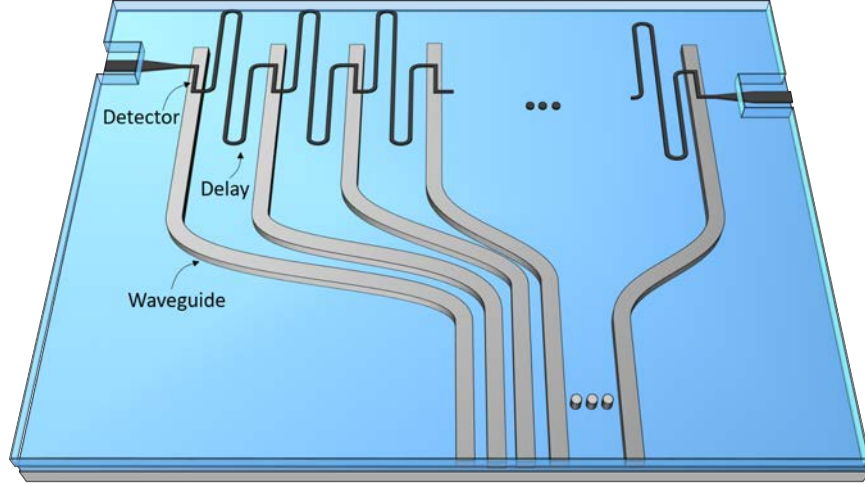


Figure 6-1: Notional schematics of the delay-line-multiplexed SNSPD array on SOI PIC.

covered by a dielectric spacer and a Au ground on the top, but the outline of the impedance-matching taper was still visible. The PIC was designed for a “continuous-time” quantum walk. Input photons could be coupled from a fiber array (8° facet) to the three input waveguides through grating couplers (Fig. 6-2(b)). The grating couplers were $127\ \mu\text{m}$ apart to match the fiber array. The input waveguides then merged into a 65-channel directional coupler for the walk (Fig. 6-2(c-d)). The optical waveguides were $500\ \text{nm}$ wide and $220\ \text{nm}$ thick (designed to support TE mode at $1550\ \text{nm}$). In the directional coupler region, neighbouring waveguides were separated by a $200\ \text{nm}$ gap. After $300\ \mu\text{m}$ of continuous coupling ($\sim 8L_c$, where L_c is the coupling length for full power transfer from one waveguide to its neighbor), the waveguides fanned out to larger spacings ($6.8\ \mu\text{m}$ between neighboring waveguides) to match the detector array (Fig. 6-2(d)). The detector array had 65 segments, each $100\ \text{nm}$ wide and $20\ \mu\text{m}$ long (20 dB absorption according to mode solutions). Each delay line was $150\ \text{nm}$ wide and $420\ \mu\text{m}$ long. The detectors and waveguides were covered by a $\sim 450\ \text{nm}$ dielectric spacer; the detector, delay line, and tapers were covered with Au to form microstrips. The designed cut-off frequency of the taper was $580\ \text{MHz}$.

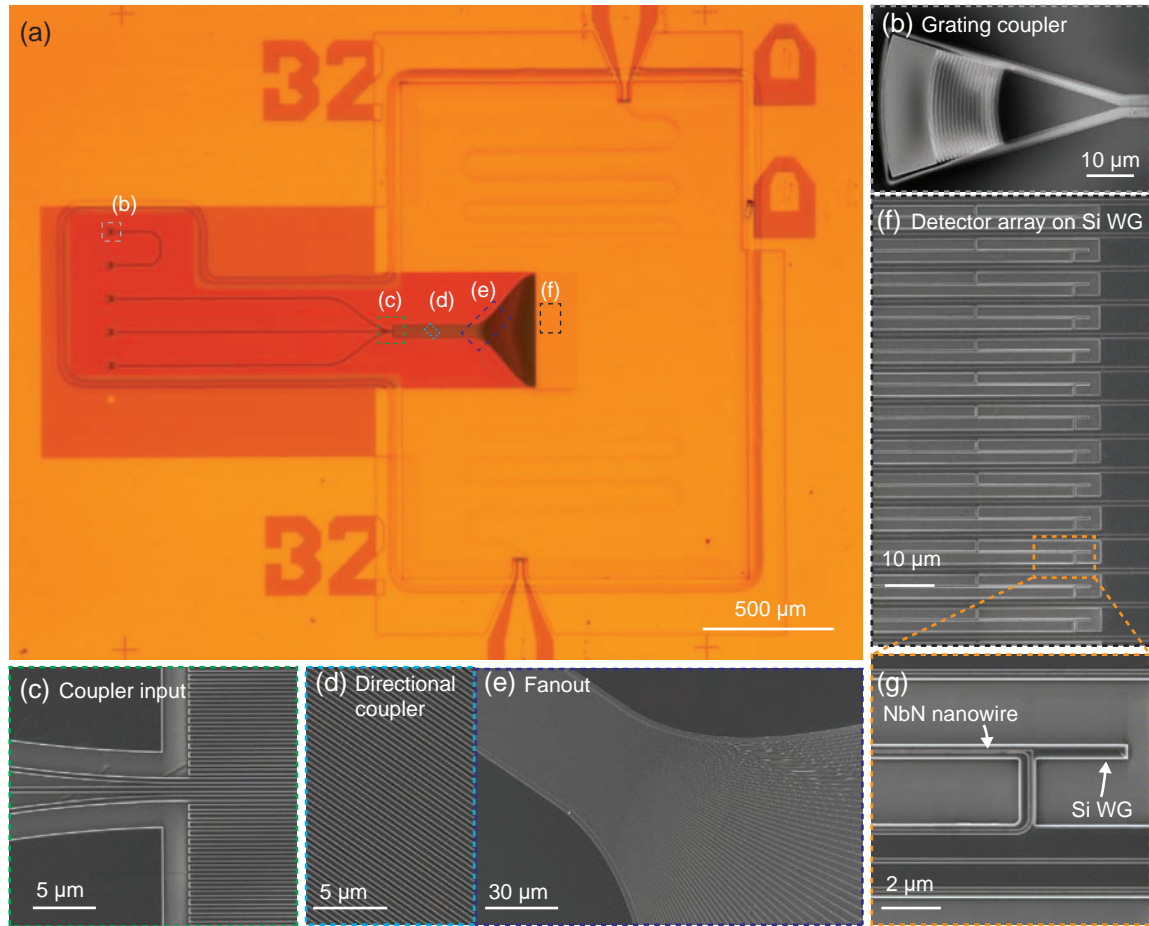


Figure 6-2: Overview of the waveguide-integrated, delay-line-multiplexed SNSPD array. (a) Optical micrograph of the device; (b)-(f) Scanning electron micrographs (SEMs) of individual components. The device was designed to run a quantum walk experiment. Photons could be coupled from a fiber array to the 3 input waveguides through the grating couplers (b). The waveguides were 220 nm thick and 500 nm wide. The input waveguides then merged into a 65-channel directional coupler (c), where the waveguides were separated with 200 nm gap (d). The coupling region was 300 μm long ($\sim 8L_c$, where L_c is the coupling length for full power transfer from one waveguide to its neighbor). After the coupling region, the 65 waveguides fan out to larger spacing (6.8 μm) to host the detector arrays (e). The detector array was delay-line multiplexed (f). Each detector segment is 100 nm wide and 20 μm long, sitting on top of the waveguide for evanescent coupling (g). Neighboring segments were connected using a 150 nm wide, 420 μm long delay line. The two ends were impedance tapered to 50 Ω and connected to the 50 Ω CPW Au pads (a). The detector area was capped with oxide spacer and Au top ground plane to transform the nanowires into microstrip. All photonic components were designed for TE mode at 1550 nm wavelength.

6.2.2 Simulation of continuous-time quantum walk

This photonic chip can be used to perform an on-chip quantum walk experiment similar to Ref [115]. However, our system allows simultaneous mapping of all coincidence events over 65 spatial modes with fast and efficient on-chip detection.

When a single photon walks down the directional coupler (propagate along z -direction), it evolves following a unitary operator $\hat{U}(z) = \exp[-i\hat{H}z]$, where

$$\hat{H} = \sum_{j=1}^N [\beta_j \hat{a}_j^\dagger \hat{a}_j + C_{j,j-1} \hat{a}_{j-1}^\dagger \hat{a}_j + C_{j,j+1} \hat{a}_{j+1}^\dagger \hat{a}_j] \quad (6.1)$$

is the Hamiltonian that captures the nearest-neighbor coupling. \hat{a}_j^\dagger and \hat{a}_j are the creation and annihilation operators for the photon on waveguide j ; β_j is the propagation constant; and $C_{j,\pm 1}$ is the hopping rate. Here we may assume that the waveguides are identical and uniformly spaced, so $\beta_j = \beta$, and $C_{j,j\pm 1} = C = \pi/(2L_c)$, where L_c is the coupling length at full power transfer between two neighboring waveguides.

The outcome of the single-photon walk is the same as that from a classical laser source. However, if we inject two indistinguishable photons (e.g., from SPDC photon pairs used in Chapter 4) into the waveguide array, the coincidence counting statistics measured on the detector array will render some non-classical feature due to quantum interference. Assuming we inject two indistinguishable photons on waveguide l and m ($l \neq m$), the input state is $|\Psi(0)\rangle = \hat{a}_l^\dagger \hat{a}_m^\dagger |0\rangle$ (for convenience, we write $\hat{a}(z)$ as \hat{a} when $z = 0$), and the probability of a coincidence event on waveguide j and k at position z (detector side) are [152]

$$\begin{aligned} \Gamma_{j,k}^q(z) &= \langle \Psi(0) | \hat{a}_j^\dagger(z) \hat{a}_k^\dagger(z) \hat{a}_j(z) \hat{a}_k(z) | \Psi(0) \rangle \\ &= \langle 0 | \hat{a}_l \hat{a}_m \left(\sum_n U_{j,n} \hat{a}_n^\dagger \right) \left(\sum_p U_{k,p} \hat{a}_p^\dagger \right) \left(\sum_q U_{j,q}^\dagger \hat{a}_q \right) \left(\sum_r U_{k,r}^\dagger \hat{a}_r \right) \hat{a}_l^\dagger \hat{a}_m^\dagger | 0 \rangle \\ &= \sum_{n,p,q,r} U_{j,n} U_{k,p} U_{j,q}^\dagger U_{k,r}^\dagger \langle 0 | \hat{a}_l \hat{a}_m \hat{a}_n^\dagger \hat{a}_p^\dagger \hat{a}_q \hat{a}_r \hat{a}_l^\dagger \hat{a}_m^\dagger | 0 \rangle \\ &= \frac{|U_{j,l} U_{k,m} + U_{j,m} U_{k,l}|^2}{1 + \delta_{j,k}}, \end{aligned} \quad (6.2)$$

where the superscript q denotes “quantum”, $\hat{a}(z) = \hat{U}(z)\hat{a}$, and $U_{a,b}$ ’s are the matrix elements of $\hat{U}(z)$.

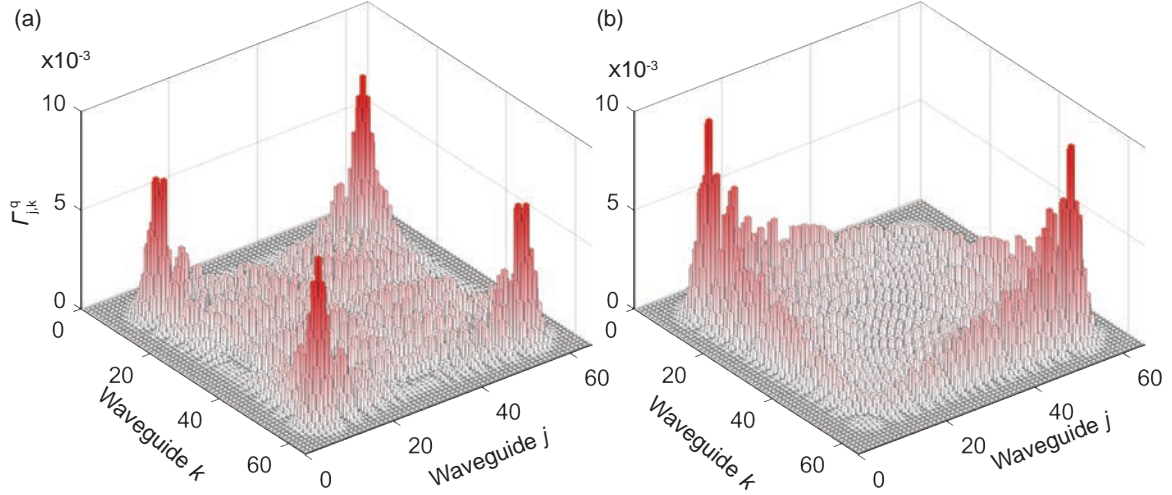


Figure 6-3: Simulated coincidence probability over the 65 channels with 2 indistinguishable input photons. (a) The 2 photons are injected into waveguides 32 and 34 (middle waveguides with 1 separation), and they tend to emerge on the sides. (b) The 2 photons are injected into waveguides 32 and 33 (2 neighboring waveguides in the middle). They tend to emerge on the sides and exhibit bunching. These figures are generated using a Matlab code written by Eugenio Maggiolini.

Without quantum interference, e.g., random phased incoherent sources, the (classical) intensity correlation will be $\Gamma_{j,k}^c(z) = I_0^2(|U_{j,l}U_{k,m} + U_{j,m}U_{k,l}|^2 + |U_{j,l}U_{k,l}|^2 + |U_{j,m}U_{k,m}|^2)$ [152], where I_0 is the power coupled to each input waveguide (m and l). This expression leads to two inequalities: $\Gamma_{j,k}^c > \sqrt{\Gamma_{j,j}^c \Gamma_{k,k}^c}/3$ and $\Gamma_{j,k}^c < \sqrt{\Gamma_{j,j}^c \Gamma_{k,k}^c}$.

Figure 6-3 shows the simulated coincidence counting map from the 65-channel “continuous-time” quantum walk circuit. Two indistinguishable photons are injected in the center waveguides, either next to each other or separated by one waveguide. These two situations are discussed intensively in Ref. [152] and [115], and both violate the inequalities list above.

6.3 Fabrication

Figure 6-2 summarizes the fabrication flow. A step-by-step description is listed below.

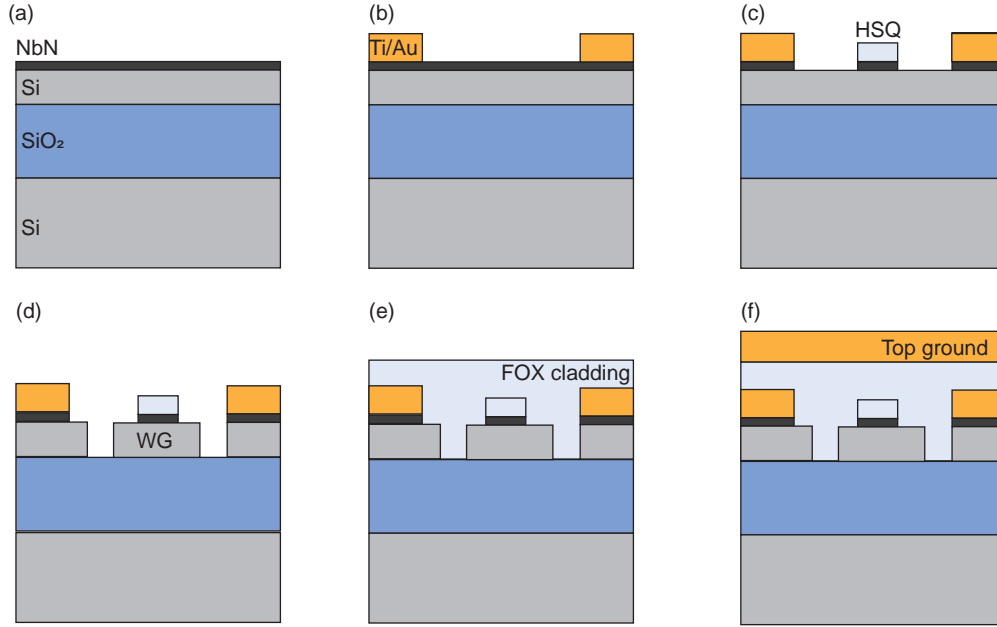


Figure 6-4: Fabrication flow. (a) Sputtering NbN on SOI substrate [220 nm Si/2 μm buried oxide (BOX)]. (b) Patterning Au contact pads and alignment marks using photolithography followed by metal liftoff (10 nm Ti/60 nm Au/10 nm Ti). (c) Nanowire patterning. (d) Waveguide patterning. (e) Putting down dielectric spacer. (f) Capping the nanowire region with Au top ground.

NbN deposition

The NbN film was sputtered on a $1\text{ cm} \times 1\text{ cm}$ SOI substrate using a room-temperature sputtering process described in Ref [153]. The films used for fabrication had a sheet resistance of $\sim 400\ \Omega/\text{sq}$, and a T_c of $\sim 8\text{ K}$ (these values were measured on sister chips from the same deposition runs).

Au contact pads and alignment marks patterning.

The contact pads were patterned using photolithography. PMGI SF9 was first spin coated at 4.5 krpm for 60 s ($0.5\ \mu\text{m}$ thick) and baked at 180°C for 90s. Microposit S1813 was then spin coated at 4.5 krpm for 60 s and baked at 100°C for 90s ($1.2\ \mu\text{m}$ thick). The patterns were exposed using a direct laser writing system (Heidelberg μPG 101) at 7 mW and 20% duty cycle. The exposed resist was developed in CD-26 for 80 s followed by DI rinse and N_2 blow-dry. The bi-layer resist created undercut to facilitate liftoff. 10 nm Ti/60 nm Au/10 nm Ti were deposited using

electron-beam evaporation and lifted off in N-Methyl-2-Pyrrolidone (NMP), followed by acetone/methanol/IPA rinse and N₂ blow-dry.

Superconducting nanowire patterning.

The chip was first immersed in MF CD-26 for 2 min, followed by 40 s dip in DI water and N₂ blow-dry. This step was to improve adhesion between HSQ and NbN. 6% HSQ was then spin coated at 3 krpm for 1 min without baking (~120 nm). The detector pattern was exposed using a 125-keV electron-beam lithography (EBL) system (Elionix ELS-F125) and aligned to the contact pads through the Au alignment marks. The detector segments (100 nm wide) and delay lines (150 nm wide) were exposed with 1 nA beam current and single-pass, while the tapers were exposed with 5 nA beam current and “multi-pass 2.” “Multi-pass 2” writes every feature twice from two different writing fields, each time with half the target dose, so stitching errors would smear out. For the nanowires and delay lines, multi-pass would increase the wire width; instead, we used single-pass and defined the field overlaps manually to avoid disconnection or constriction due to stitching error.

Field stitching deserves some special care. The detector is a continuous wire that extends multiple writing fields (500 μm). Different from photonic waveguides, where a few small discontinuities (tens of nm) are acceptable, discontinuities in the nanowire will cause open circuit or constriction to the entire line. To avoid inter-field stitching (caused by stage moving from field to field), the best practice is to define the writing fields manually, and add extra overlaps. Figure 6-5 shows some examples of inter-field stitching. Intra-field stitching could also happen. The best practice to avoid this is to make the writing sequence “follow geometry” (an option in the the GeniSys Beamer software) instead of jumping around in the field.

The exposed resist was developed in 25% TMAH for 2 min followed by DI rinse, IPA rinse (reduce surface tension), and N₂ blow-dry. After development, the HSQ pattern was transferred to the NbN using reactive ion etching (RIE) with CF₄/H₂ (7 sccm: 15 sccm at 10 mTorr) at 50 W for 2 min 40s (Plasmatherm at the NSL).

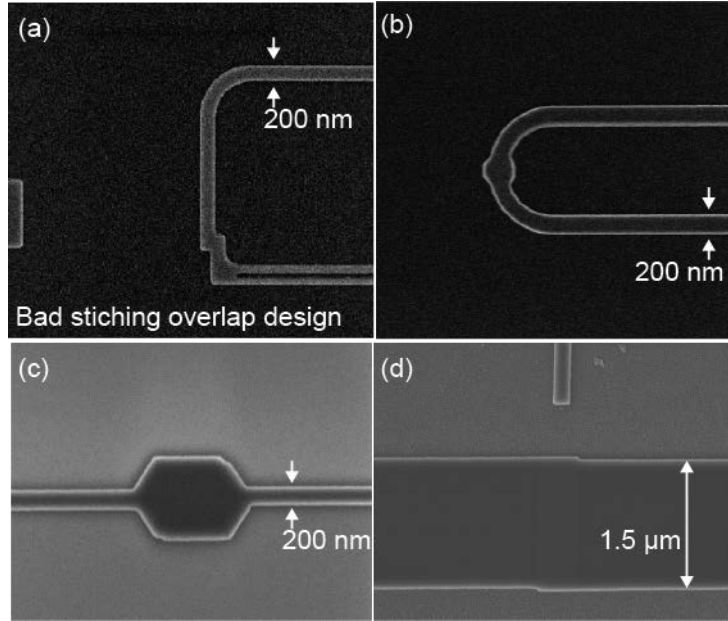


Figure 6-5: Examples of inter-field stitching in EBL. (a) Large stitching error and bad overlap design, as can be seen in the discontinuity. This design is bad because (1) it made field stitching happen near critical features; (2) the overlap avoids disconnection but not constriction (does not tolerate shift in the x-direction). (b)-(c) proper manual stitching overlap designs. If a narrow line has to pass two writing fields, we cut it into two parts (assigned to two different fields) and taper them up to make a manual overlap. (d) When the wire is wide (μm level), we just need to avoid disconnection, so an overlap in x-direction is sufficient.

Si waveguide patterning.

ZEP520A was spin coated on the chip at 2 krpm and then baked at 180°C for 2 min. The outlines of the waveguides ($2\ \mu\text{m}$ offset) were exposed using EBL. The writing was aligned to the nanowire layer through the Au alignment marks using the Reg 2 automatic alignment function. The beam current was set to 500 pA. The point spread function of the electron beam in ZEP on SOI was calculated using GeniSys Tracer, and proximity effect correction (PEC) was applied to the entire photonic circuits using GeniSys Beamer (see Fig. 6-6). Without PEC, the fanout section would be overdosed. To mitigate field stitching, the entire pattern was written with “multi-pass 2.” Since PEC gives a different dose factor to each fractured area, the actual areal dose varies. The nominal dwell time was set to 24 ns/dot ($2.5\ \text{nm}/\text{dot}$), so that the highest areal dose (assigned to sparse, isolated structures) was $\sim 500\ \mu\text{C}/\text{cm}^2$. The exposed resist

was developed in o-xylene at 5°C for 2 min 30 s, followed by 30 s IPA rinse and N₂ blow-dry.

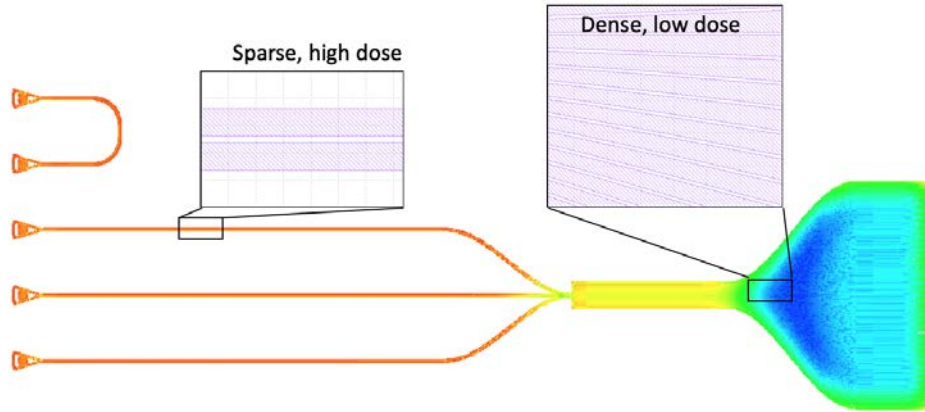


Figure 6-6: Proximity effect correction for the positive-tone waveguide pattern. The corrected dose distribution was calculated using a commercial PEC software (GeniSys Beamer). Sparse area (left) requires 80% more dose than the dense area (right).

The Si layer was then etched using CF₄/SF₆ (30 sccm: 10 sccm) in an electron-cyclotron resonance (ECR) RIE system (Plasmaquest). The chamber pressure was kept at 10 mTorr and the cooling temperature was set to 15°C (the actual chuck temperature was ~20°C). The ECR microwave power and RF bias power were set to 100 W and 20 W, respectively. To etch the The total etching time was set to 228 s (10% overetch). The etch rate was measured using a stylus profiler (Dektak) and double confirmed using cross-sectional SEM. The sidewall slope was very sensitive to the gas ratio, ECR power, and RF bias power. For instance, an increase of SF₆ flow would cause convex sidewall.

We also developed a negative-tone process for the Si waveguide. We used 6% HSQ (spin coated at 3 krpm) as the etch mask. Since the 65 closely-packed waveguides in the coupling regime (500 nm waveguide with 200 nm gap in between) was too dense, high-contrast salty development was needed [154]. The cured HSQ is close to SiO₂ and has good etch resistance to Cl₂ chemistry. We etched the Si waveguides in the ECR RIE using Cl₂/H₂ (40 sccm:20 sccm). The chamber pressure was kept at 10 mTorr. The ECR microwave power was set to 200 W and the RF bias was set to 20

W. The waveguides fabricated from HSQ process had smoother sidewalls compared to the ZEP process. However, Cl_2 etching would attack the Au contact pads, so additional protection layers were required. Despite that the negative-tone process exposes less area than the positive-tone process, HSQ requires much larger areal dose ($\sim 9000 \mu\text{C}/\text{cm}^2$ for salty developer), so the overall writing time for the HSQ process is longer. Also, once exposed, the HSQ is hard to remove, and rework is not possible. Considering the fabrication complexity and EBL writing time, we decided to adopt the ZEP process.

Figure 6-7 shows the cross-sectional SEMs of the etched waveguides using positive-tone (ZEP as mask, CF_4/SF_6 etching) and negative-tone (HSQ as mask, Cl_2 etching) processes.

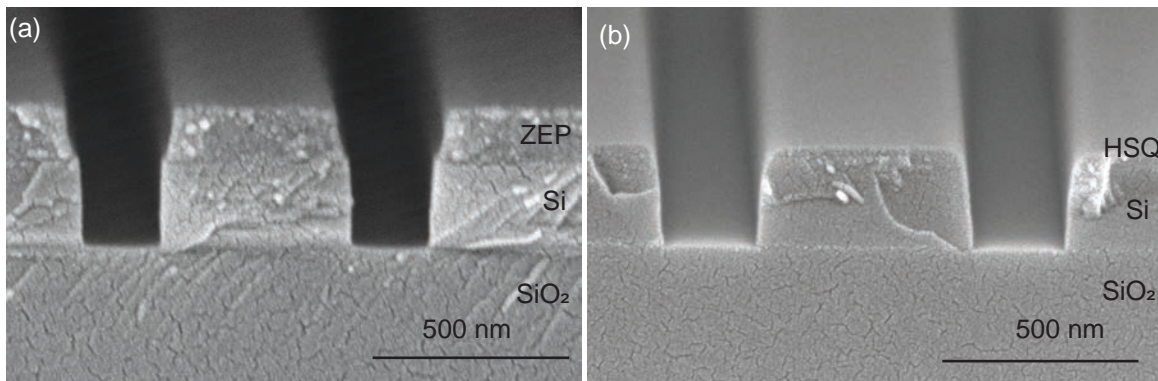


Figure 6-7: Cross-sectional SEMs of etched Si waveguides. (a) Using ZEP520A as mask, and etching with CF_4/SF_6 RIE. (b) Using HSQ as mask, and etching with Cl_2 RIE. The granular features on the surface were from sputtered Au/Pd, which was used to avoid charging during imaging.

Dielectric spacer and top ground.

The process for fabricating dielectric spacer and top ground was similar to that described in Chapter 5. FOX-16 was spin coated at 3 krpm for 1 min and baked at 250°C for 2 min. The intended area (covering both nanowire and waveguides) was exposed using EBL at 20 nA with an areal dose of $800 \mu\text{C}/\text{cm}^2$, and then developed in CD-26 for 70 s followed by DI rinse and N_2 blow-dry. The top ground (10 nm Ti/60 nm Au) was defined similarly to the bottom Au pads. It was aligned to the

bottom Au mark and extended to make contact to the bottom ground.

6.4 Preliminary measurement results

So far, we have not been able to couple light efficiently into the waveguides in the cryostat. Instead, we flood illuminated the entire chip with a 1550 nm pulsed laser (attenuated into single-photon level) and measured the detector response at 1 K. The measurement method was similar to that in Chapter 5.

Figure 6-8 shows the output pulses from the detector array. We triggered on one channel and accumulated the pulse traces from the other. We observed 65 distinct groups of pulses. The impedance-matching taper here was well designed, so no significant reflections were observed on the rising edge, and the pulse shapes were relatively uniform.

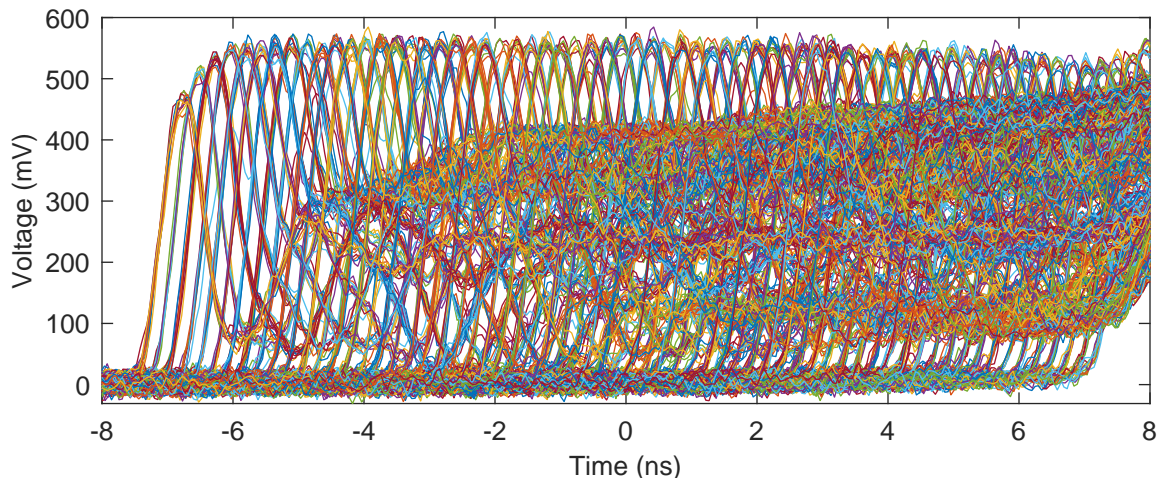


Figure 6-8: Output pulses from the 65-element detector array (flood illumination). We triggered at one channel and recorded pulse traces from the other on the oscilloscope. 65 groups of pulses were observed. Unlike the detector in Chapter 5, the impedance-matching taper here was well designed, and the rising edges did not show any steps due to microwave reflection.

Figure 6-9 shows histograms of the difference time ($t_{\text{diff}} = (t_1 - t_2)/2$) with increasing bias current (I_b). As I_b approached the switching current ($I_{\text{SW}} \approx 17.5 \mu\text{A}$), the counting rate from the 27th element started to increase rapidly, suggesting that this element was constricted.

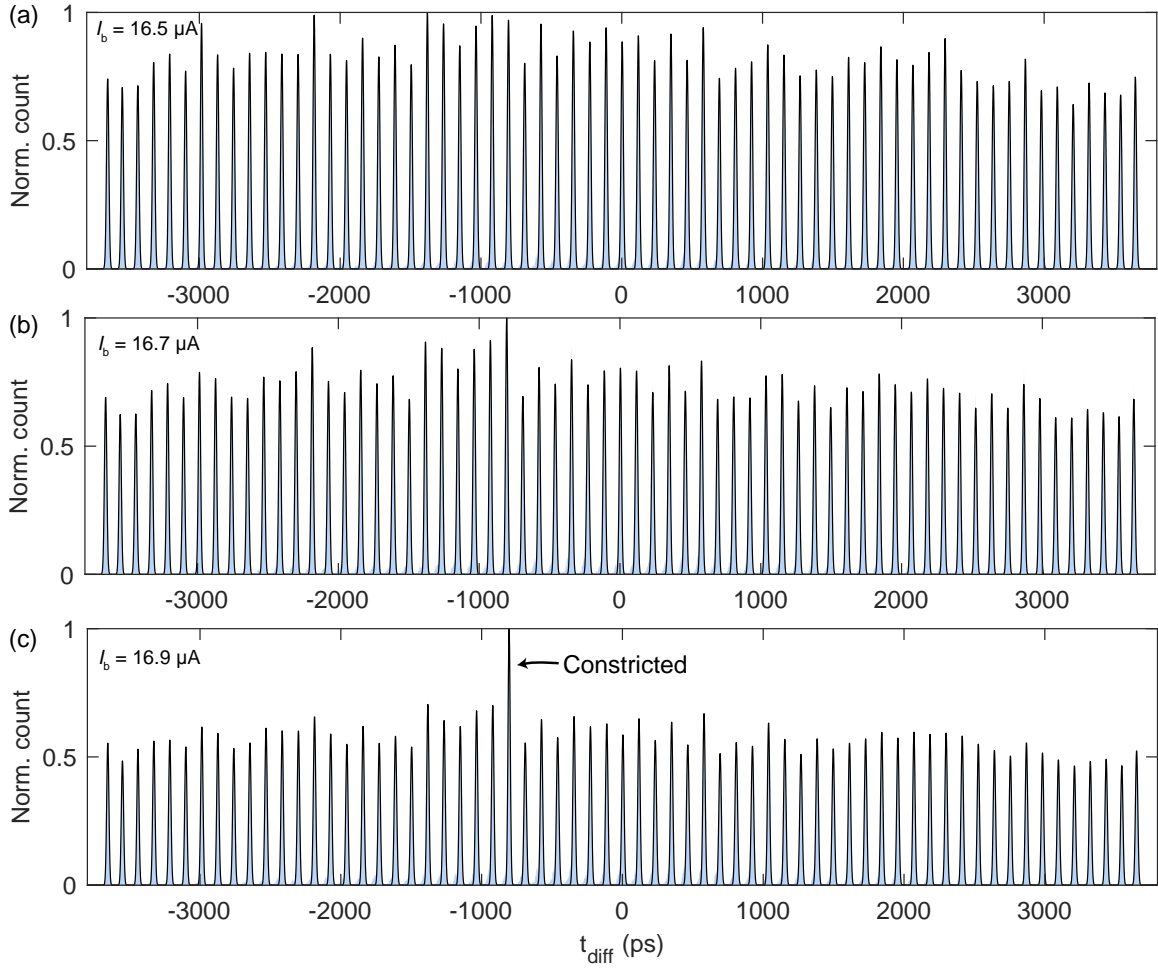


Figure 6-9: t_{diff} histogram under different bias current. The detector was flood illuminated with 1550 nm laser in the single-photon regime. When the bias current approached the switching current, counting events from the 27th element started to dominate, indicating that it had a smaller switching current (likely constricted) among others.

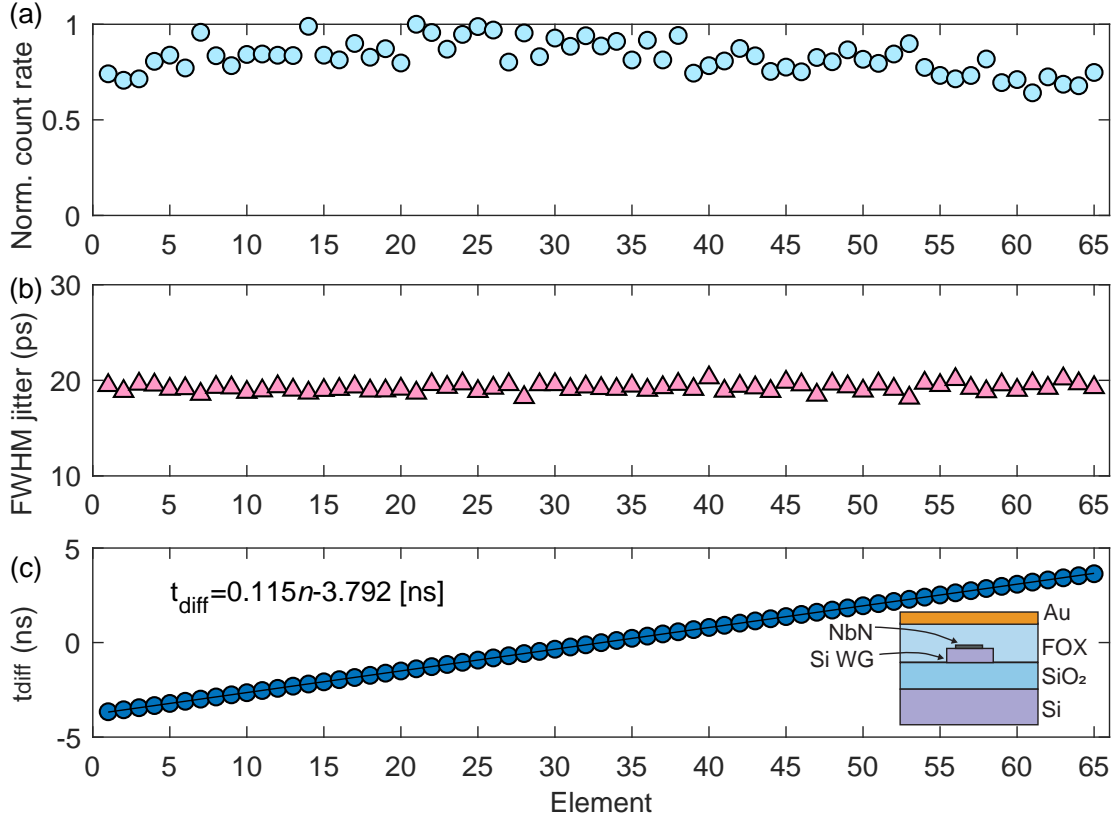


Figure 6-10: Heights, widths, and peak positions of the 65 Gaussians in the t_{diff} histogram in Fig. 6-9 ($I_b = 16.5 \mu\text{A}$). (a) The amplitudes had a standard deviation over mean of 10.4%. (b) The FWHM differential jitter (mainly electrical jitter) had a mean of 19.2 ps and standard deviation of 0.4 ps. (c) We linearly fitted the peak positions and obtained a slope of 115 ps delay per element. Given the 420 μm delay length, the speed of light in the microstrip was $0.0122c$.

We processed the t_{diff} histogram at $I_b = 16.5 \mu\text{A}$ and extracted the heights, widths, and peak positions of the 65 Gaussians. At this bias current, the counting rate (Gaussian height) from each element was relatively uniform, with a standard deviation over mean value of 10.4%. The FWHM of the Gaussians (mostly electrical jitter) had a mean of 19.2 ps and a standard deviation of 0.4 ps. We linearly fitted the peak position over element number (Fig. 6-10) and obtained a slope of 0.115 ns/element. Given that each delay line was 420 μm , the group velocity of the delay line was $0.0122c$, where c is the speed of light in vacuum.

We measured the photon count rate (PCR) and dark count rate (DCR) as functions of I_b (see Fig. 6-11). Under 1064 nm illumination, the PCR started to increase

rapidly at high bias current. It was likely because the 150-nm-wide delay lines were biased high enough ($\sim 60\%I_{sw}$) and started to count photons.

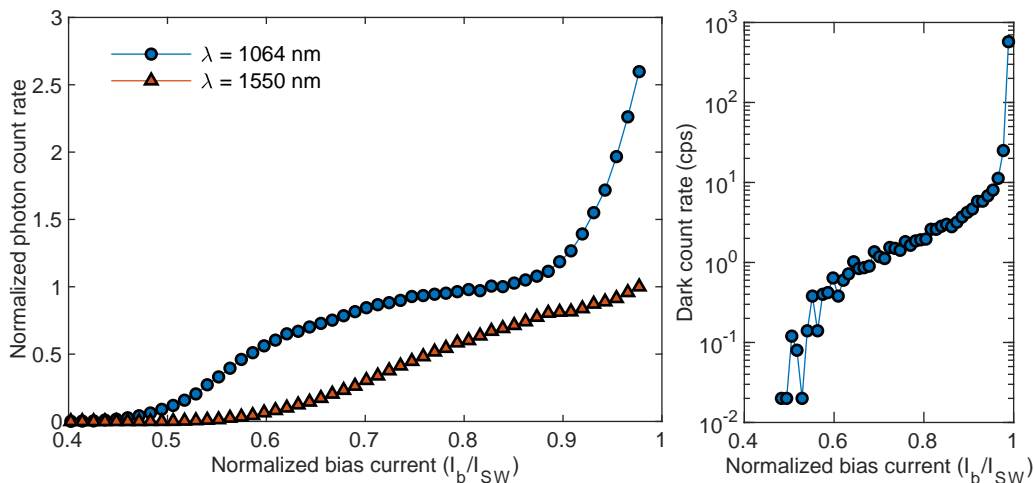


Figure 6-11: Normalized photon count rate (PCR) and dark count rate (DCR) of the 65-element array.. At 1064 nm illumination, the PCR increased steeply near I_{sw} , likely because the delay lines started to get critically biased and count photons.

In one of the chips, we fabricated some detectors using a positive-tone resist (gL2000). In these devices, the delay lines were grounded CPWs (see inset of Fig. 6-12). The t_{diff} histogram is shown in Figure 6-12. By fitting the slope of the Gaussian peak positions, we obtained a group velocity of $0.0088c$. Note that these delay lines were slightly wider than that in Fig. 6-10 (200 nm instead of 150 nm), but the added capacitance from the side grounds and the unpatterned Si layer overall resulted in a group velocity.

6.5 Conclusion

In summary, we have demonstrated a 65-element SNSPD array on SOI PIC. The detectors were integrated directly on single-mode Si waveguides and were multiplexed using microstrip delay lines with a measured group velocity of $0.0122c$. We described in detail the fabrication process for this hybrid-material, multi-dimension system. By flood illuminating the entire array, we were able to observe photon counts from all 65 detector elements. The array size is one of the largest that has been reported. With

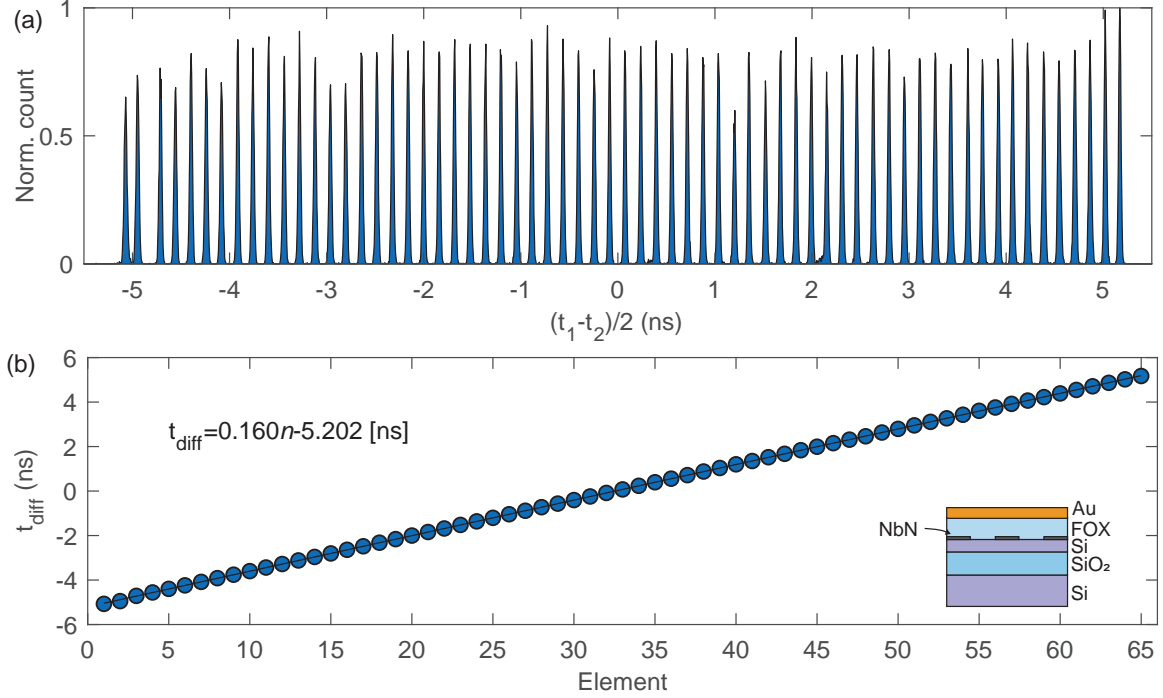


Figure 6-12: t_{diff} histogram for a 65-element array multiplexed through grounded-CPW without waveguide patterning. The center conductor width of the delay line was 200 nm, and the gap size of the CPW was 500 nm. The measured group velocity in this delay line was $0.0088c$. This value is smaller than that in Fig. 6-10 due to the increased line capacitance from the side grounds as well as the higher-index dielectric environment from the unpatterned Si layer. The trenches around the nanowire were patterned using gL2000 (positive-tone electron-beam resist).

future work on fiber-to-chip coupling at cryogenic temperature, this device will be capable of performing an on-chip quantum walk experiment over 65 spatial modes. The demonstrated detector architecture may contribute towards the development of a large-scale, fully-integrated quantum photonic processor.

Chapter 7

Summary and outlook

In this thesis, we used superconducting nanowire transmission lines to devise new single-photon detector architectures. Here we summarize the main results and discuss future directions.

Superconducting nanowire transmission lines

Superconducting nanowire transmission lines operate in the kinetic-inductive limit and have high impedance, slow phase velocity, and large nonlinearity. Their impedance can be controlled by changing the nanowire width, and matching from $k\Omega$ to $50\ \Omega$ is possible using an adiabatic taper.

We proposed a forward coupler based on coupled nanowires and demonstrated its tunability using a bias current. This coupler, together with slow-wave transmission lines, may be used to construct a photon-sensitive microwave interferometer.

A promising future direction is using nanowire transmission lines to make kinetic-inductance traveling-wave parametric amplifiers [42, 155]. The small depairing current (μA) of the nanowire ensures high nonlinearity, and the slow phase velocity reduces the guided wavelength. These two improvements may considerably shrink the device footprint, and direct integration with superconducting qubits may be possible in the future.

Superconducting tapered nanowire detectors (STaND)

In the STaND, the integrated impedance-matching taper provides the nanowire meander an effective load impedance at $k\Omega$ while connecting to the readout electronics at $50\ \Omega$. This architecture increases the detector output voltage, reduces the timing jitter, and enables photon number resolution.

There are a few immediate future steps to improve detector performance: (1) Integrate the detector in an optical cavity and use self-aligned fiber packaging to improve system detection efficiency [110, 109, 7]. (2) Replace the coplanar waveguide (CPW) taper to microstrip taper to reduce device footprint and reset time. The gold mirror in the optical cavity can serve as the ground plane. (3) Develop low-noise, high-speed, cryogenic comparator readout to achieve real-time photon-number discrimination and time tagging. (4) Use differential tapered readout to reduce geometric jitter in large area detectors [39].

Delay-line-multiplexed detector arrays

The two-terminal detector array multiplexed using slow-wave superconducting microstrips (“nanostrip” is probably more accurate here) can perform coincidence counting over a large number of spatial modes. In the presence of impedance mismatch, microwave reflections in the nanowire create unique fingerprints in the output pulse shapes and can be used to resolve photon number.

Pulse shape analysis is particularly interesting. In principle, if we can distinguish the pulse shapes for every detection case, we will no longer need the timing reference for multi-photon detection. In the 4-element array, we manually identified these fingerprints. For larger arrays, a machine learning algorithm could be helpful.

The 65-element array on silicon-on-insulator waveguides is among the largest integrated detector array. With the rapid advance in large-scale photonic integrated circuits [149] and promising progress on single-photon emitter integration [155], a fully integrated photonic processor may be possible.

We have seen slower and slower group velocities in nanowire transmission lines.

The 300-nm-wide CPW in the SNSPI had a group velocity of $0.02c$ [40]. The 300-nm-wide microstrip in Chapter 5 Fig. 5-6 had a group velocity of $0.016c$. $0.012c$ was seen in the 150-nm-wide microstrip in Chapter 5 Fig. 6-10. $0.0088c$ was observed in the grounded CPW in Chapter 6 Fig. 6-12. Very recently, $0.0073c$ was reported in an 80-nm-wide microstrip with alumina dielectric spacer [156]. These comparisons are by no means fair because measurement condition (e.g., different temperature and bias current) and superconducting film properties are all different, but the trend is interesting.

A potential future direction on the delay-line-multiplexed detector array is RF biasing. Different from resonant circuits [130, 24], with broadband impedance matching, we may send various microwave tones and waveforms into the wire, and these microwave signals can also be added on top of a DC background. This method may enable fast reset.

Bibliography

- [1] G. N. Gol'tsman, O. Okunev, G. Chulkova, A. Lipatov, A. Semenov, K. Smirnov, B. Voronov, A. Dzardanov, C. Williams, and Roman Sobolewski. Picosecond superconducting single-photon optical detector. *Appl. Phys. Lett.*, 79(6):705–707, 2001.
- [2] R.H. Hadfield. Single-photon detectors for optical quantum information applications. *Nat. Photonics*, 3(12):696–705, 2009.
- [3] Hua-Lei Yin, Teng-Yun Chen, Zong-Wen Yu, Hui Liu, Li-Xing You, Yi-Heng Zhou, Si-Jing Chen, Yingqiu Mao, Ming-Qi Huang, Wei-Jun Zhang, Hao Chen, Ming Jun Li, Daniel Nolan, Fei Zhou, Xiao Jiang, Zhen Wang, Qiang Zhang, Xiang-Bin Wang, and Jian-Wei Pan. Measurement-Device-Independent Quantum Key Distribution Over a 404 km Optical Fiber. *Phys. Rev. Lett.*, 117(19):190501, 2016.
- [4] Matthew E. Grein, Andrew J. Kerman, Eric A. Dauler, Matthew M. Willis, Barry Romkey, Richard J. Molnar, Bryan S. Robinson, Daniel V. Murphy, and Don M. Boroson. An optical receiver for the Lunar Laser Communication Demonstration based on photon-counting superconducting nanowires. In *Proc. SPIE*, volume 9492, page 949208, 2015.
- [5] Lynden K. Shalm, Evan Meyer-Scott, Bradley G. Christensen, Peter Bierhorst, Michael A. Wayne, Martin J. Stevens, Thomas Gerrits, Scott Glancy, Deny R. Hamel, Michael S. Allman, Kevin J. Coakley, Shellee D. Dyer, Carson Hodge, Adriana E. Lita, Varun B. Verma, Camilla Lambrocco, Edward Tortorici, Alan L. Migdall, Yanbao Zhang, Daniel R. Kumor, William H. Farr, Francesco Marsili, Matthew D. Shaw, Jeffrey A. Stern, Carlos Abellan, Waldimar Amaya, Valerio Pruneri, Thomas Jennewein, Morgan W. Mitchell, Paul G. Kwiat, Joshua C. Bienfang, Richard P. Mirin, Emanuel Knill, and Sae Woo Nam. Strong Loophole-Free Test of Local Realism. *Phys. Rev. Lett.*, 115:250402, 2015.
- [6] J K W Yang, A J Kerman, E A Dauler, V Anant, K M Rosfjord, and K K Berggren. Modeling the electrical and thermal response of superconducting nanowire single-photon detectors. *IEEE Trans. Appl. Supercond.*, 17(2):581–585, 2007.

- [7] F. Marsili, V. B. Verma, J. A. Stern, S. Harrington, a. E. Lita, T. Gerrits, I. Vayshenker, B. Baek, M. D. Shaw, R. P. Mirin, and S. W. Nam. Detecting Single Infrared Photons with 93% System Efficiency. *Nat. Photonics*, 7(3):210–214, 2013.
- [8] B. A. Korzh, Q-Y. Zhao, S. Frasca, J. P. Allmaras, T. M. Autry, E. A. Bersin, M. Colangelo, G. M. Crouch, A. E. Dane, T. Gerrits, F. Marsili, G. Moody, E. Ramirez, J. D. Rezac, M. J. Stevens, E. E. Wollman, D. Zhu, P. D. Hale, K. L. Silverman, R. P. Mirin, S. W. Nam, M. D. Shaw, and K. K. Berggren. Demonstrating sub-3 ps temporal resolution in a superconducting nanowire single-photon detector. *ArXiv:1804.06839*, 2018.
- [9] Hiroyuki Shibata, Kaoru Shimizu, Hiroki Takesue, and Yasuhiro Tokura. Ultimate low system dark-count rate for superconducting nanowire single-photon detector. *Opt. Lett.*, 40(14):3428–31, 2015.
- [10] Andreas Vetter, Simone Ferrari, Patrik Rath, Rasoul Alaee, Oliver Kahl, Vadim Kovalyuk, Silvia Diewald, Gregory N. Goltsman, Alexander Korneev, Carsten Rockstuhl, and Wolfram H. P. Pernice. Cavity-Enhanced and Ultrafast Superconducting Single-Photon Detectors. *Nano Lett.*, 16(11):7085–7092, 2016.
- [11] Francesco Marsili, Francesco Bellei, Faraz Najafi, Andrew E. Dane, Eric A. Dauler, Richard J. Molnar, and Karl K. Berggren. Efficient single photon detection from 500 nm to 5 μ m wavelength. *Nano Lett.*, 12(9):4799–4804, 2012.
- [12] E. E. Wollman, V. B. Verma, A. D. Beyer, R. M. Briggs, B. Korzh, J. P. Allmaras, F. Marsili, A. E. Lita, R. P. Mirin, S. W. Nam, and M. D. Shaw. UV superconducting nanowire single-photon detectors with high efficiency, low noise, and 4 K operating temperature. *Opt. Express*, 25(22):26792, 2017.
- [13] Kazuya Takemoto, Yoshihiro Nambu, Toshiyuki Miyazawa, Yoshiki Sakuma, Tsuyoshi Yamamoto, Shinichi Yorozu, and Yasuhiko Arakawa. Quantum key distribution over 120km using ultrahigh purity single-photon source and superconducting single-photon detectors. *Sci. Rep.*, 5:14383, 2015.
- [14] G. Reithmaier, M. Kaniber, F. Flassig, S. Lichtmannecker, K. Müller, A. Andrejew, J. Vučković, R. Gross, and J. J. Finley. On-Chip Generation, Routing, and Detection of Resonance Fluorescence. *Nano Lett.*, 15(8):5208–5213, 2015.
- [15] Eric A. Dauler, Martin J. Stevens, Burm Baek, Richard J. Molnar, Scott a. Hamilton, Richard P. Mirin, Sae Woo Nam, and Karl K. Berggren. Measuring intensity correlations with a two-element superconducting nanowire single-photon detector. *Phys. Rev. A*, 78:053826, 2008.
- [16] Hui Zhou, Yuhao He, Lixing You, Sijin Chen, Weijun Zhang, Junjie Wu, Zhen Wang, and Xiaoming Xie. Few-photon imaging at 1550 nm using a low-timing-jitter superconducting nanowire single-photon detector. *Opt. Express*, 23(11):14603, jun 2015.

- [17] M. D. Eisaman, J. Fan, A. Migdall, and S. V. Polyakov. Invited Review Article: Single-photon sources and detectors. *Rev. Sci. Instrum.*, 82:071101, 2011.
- [18] C. M. Natarajan, M. G. Tanner, and R. H. Hadfield. Superconducting nanowire single-photon detectors: physics and applications. *Supercond. Sci. Technol.*, 25(6):063001, 2012.
- [19] Simone Ferrari, Carsten Schuck, and Wolfram Pernice. Waveguide-integrated superconducting nanowire single-photon detectors. *Nanophotonics*, 7(11):1725–1758, 2018.
- [20] Francesco Mattioli, Zili Zhou, Alessandro Gaggero, Rosalinda Gaudio, Saeedeh Jahanmirinejad, Döndü Sahin, Francesco Marsili, Roberto Leoni, and Andrea Fiore. Photon-number-resolving superconducting nanowire detectors. *Supercond. Sci. Technol.*, 28(10):104001, 2015.
- [21] Eric A. Dauler, Matthew E. Grein, Andrew J. Kerman, Francesco Marsili, Shigehito Miki, Sae Woo Nam, Matthew D. Shaw, Hirotaka Terai, Varun B. Verma, and Taro Yamashita. Review of superconducting nanowire single-photon detector system design options and demonstrated performance. *Opt. Eng.*, 53(8):081907, 2014.
- [22] Adam N. McCaughan. Readout architectures for superconducting nanowire single photon detectors. *Supercond. Sci. Technol.*, 31:040501, 2018.
- [23] M. S. Allman, V. B. Verma, M. Stevens, T. Gerrits, R. D. Horansky, a. E. Lita, F. Marsili, a. Beyer, M. D. Shaw, D. Kumor, R. Mirin, and S. W. Nam. A near-infrared 64-pixel superconducting nanowire single photon detector array with integrated multiplexed readout. *Appl. Phys. Lett.*, 106(19):192601, 2015.
- [24] S. Doerner, A. Kuzmin, S. Wuensch, I. Charaev, F. Boes, T. Zwick, and M. Siegel. Frequency-multiplexed bias and readout of a 16-pixel superconducting nanowire single-photon detector array. *Appl. Phys. Lett.*, 111:032603, 2017.
- [25] M. Hofherr, M. Arndt, K. Il'in, D. Henrich, M. Siegel, J. Toussaint, T. May, and H. Meyer. Time-Tagged Multiplexing of Serially Biased Superconducting Nanowire Single-Photon Detectors. *IEEE Trans. Appl. Supercond.*, 23(3):2501205, 2013.
- [26] Shigeyuki Miyajima, Shigehito Miki, Masahiro Yabuno, Taro Yamashita, and Hirotaka Terai. Timing discriminator based on single-flux-quantum circuit toward high time-resolved photon detection. *Supercond. Sci. Technol.*, 30:12LT01, 2017.
- [27] Shigeyuki Miyajima, Masahiro Yabuno, Shigehito Miki, Taro Yamashita, and Hirotaka Terai. High-time-resolved 64-channel single-flux quantum-based address encoder integrated with a multi-pixel superconducting nanowire single-photon detector. *Opt. Express*, 26(22):29045, 2018.

- [28] Aaron J. Miller, Sae Woo Nam, John M. Martinis, and Alexander V. Sergienko. Demonstration of a low-noise near-infrared photon counter with multiphoton discrimination. *Appl. Phys. Lett.*, 83(4):791–793, 2003.
- [29] Adriana E Lita, Aaron J Miller, and Sae Woo Nam. Counting near-infrared single-photons with 95% efficiency. *Opt. Express*, 16(5):3032–3040, 2008.
- [30] Peter K Day, Henry G LeDuc, Benjamin A Mazin, Anastasios Vayonakis, and Jonas Zmuidzinas. A broadband superconducting detector suitable for use in large arrays. *Nature*, 425:817, 2003.
- [31] Eric A. Dauler, Andrew J. Kerman, Bryan S. Robinson, Joel K.W. Yang, Boris Voronov, Gregory Goltsman, Scott A. Hamilton, and Karl K. Berggren. Photon-number-resolution with sub-30-ps timing using multi-element superconducting nanowire single photon detectors. *J. Mod. Opt.*, 56(2-3):364–373, 2009.
- [32] Aleksander Divochiy, Francesco Marsili, David Bitauld, Alessandro Gaggero, Roberto Leoni, Francesco Mattioli, Alexander Korneev, Vitaliy Seleznev, Nataliya Kaurova, Olga Minaeva, Gregory G O L Tsman, Konstantinos G Lagoudakis, Andrea Fiore, Moushab Benkhaoul, and Francis Le. Superconducting nanowire photon- number-resolving detector at telecommunication wavelengths. *Nat. Photonics*, 2:302–306, 2008.
- [33] D. Sahin, A. Gaggero, Z. Zhou, S. Jahanmirinejad, F. Mattioli, R. Leoni, J. Beetz, M. Lermer, M. Kamp, S. Hofling, and A. Fiore. Waveguide photon-number-resolving detectors for quantum photonic integrated circuits. *Appl. Phys. Lett.*, 103:111116, 2013.
- [34] S. Jahanmirinejad, G. Frucci, F. Mattioli, D. Sahin, A. Gaggero, R. Leoni, and A. Fiore. Photon-number resolving detector based on a series array of superconducting nanowires. *Appl. Phys. Lett.*, 101:072602, 2012.
- [35] Clinton Cahall, Kathryn L. Nicolich, Nurul T. Islam, Gregory P. Lafyatis, Aaron J. Miller, Daniel J. Gauthier, and Jungsang Kim. Multi-photon detection using a conventional superconducting nanowire single-photon detector. *Optica*, 4(12):1534, 2017.
- [36] Junjie Wu, Lixing You, Sijing Chen, Hao Li, Yuhao He, Chaolin Lv, Zhen Wang, and Xiaoming Xie. Improving the timing jitter of a superconducting nanowire single-photon detection system. *Appl. Opt.*, 56(8):2195–2200, 2017.
- [37] B. Korzh, Q.-Y. Zhao, S. Frasca, D. Zhu, E. Ramirez, E. Bersin, M. Colangelo, A. E. Dane, A. D. Beyer, J. Allmaras, E. E. Wollman, K. K. Berggren, M. D. Shaw, and M. D. Shaw. WSi superconducting nanowire single photon detector with a temporal resolution below 5 ps. In *Conf. Lasers Electro-Optics*, page FW3F.3. OSA, 2018.

- [38] Daniel F Santavicca, Jesse K Adams, Lierd E Grant, Adam N Mccaughan, and Karl K Berggren. Microwave dynamics of high aspect ratio superconducting nanowires studied using self-resonance. *J. Appl. Phys.*, 119:234302, 2016.
- [39] Niccolò Calandri, Qing-Yuan Zhao, Di Zhu, Andrew Dane, and Karl K. Berggren. Superconducting nanowire detector jitter limited by detector geometry. *Appl. Phys. Lett.*, 109:152601, 2016.
- [40] Qing-Yuan Zhao, Di Zhu, Niccolò Calandri, Andrew E. Dane, Adam N. McCaughan, Francesco Bellei, Hao-Zhu Wang, Daniel F. Santavicca, and Karl K. Berggren. Single-photon imager based on a superconducting nanowire delay line. *Nat. Photonics*, 11(4):247–251, 2017.
- [41] Jonas Zmuidzinas. Superconducting Microresonators: Physics and Applications. *Annu. Rev. Condens. Matter Phys.*, 3(1):169–214, 2012.
- [42] Byeong Ho Eom, Peter K. Day, Henry G. LeDuc, and Jonas Zmuidzinas. A wideband, low-noise superconducting amplifier with high dynamic range. *Nat. Phys.*, 8(8):623–627, 2012.
- [43] Terry P. Orlando, Kevin a. Delin, and Christopher J. Lobb. *Foundations of Applied Superconductivity*. Addison-Wesley, 1991.
- [44] M. Staffaroni, J. Conway, S. Vedantam, J. Tang, and E. Yablonovitch. Circuit analysis in metal-optics. *Photonics Nanostructures - Fundam. Appl.*, 10(1):166–176, 2012.
- [45] Anand Kamlapure, Mintu Mondal, Madhavi Chand, Archana Mishra, John Jesudasan, Vivas Bagwe, L. Benfatto, Vikram Tripathi, and Pratap Raychaudhuri. Measurement of magnetic penetration depth and superconducting energy gap in very thin epitaxial NbN films. *Appl. Phys. Lett.*, 96:072509, 2010.
- [46] D. C. Mattis and J. Bardeen. Theory of the anomalous skin effect in normal and superconducting metals. *Phys. Rev.*, 111(2):412–417, 1958.
- [47] Alex D. Semenov, Gregory N. Gol'tsman, and Alexander A. Korneev. Quantum detection by current carrying superconducting film. *Phys. C Supercond. its Appl.*, 351(4):349–356, 2001.
- [48] John R. Clem and Karl K. Berggren. Geometry-dependent critical currents in superconducting nanocircuits. *Phys. Rev. B*, 84:174510, 2011.
- [49] S. Frasca, B. Korzh, M. Colangelo, D. Zhu, A. E. Lita, J. P. Allmaras, E. E. Wollman, V. B. Verma, A. E. Dane, E. Ramirez, A. D. Beyer, S. W. Nam, A. G. Kozorezov, M. D. Shaw, and K. K. Berggren. Determining the depairing current in superconducting nanowire single-photon detectors. *ArXiv:1904.08596*, 2019.

- [50] Anagnostis Tsiatmas, Vassili A. Fedotov, F. Javier García De Abajo, and Nikolay I. Zheludev. Low-loss terahertz superconducting plasmonics. *New J. Phys.*, 14:115006, 2012.
- [51] David M. Pozar. *Microwave Engineering*. John Wiley & Sons, Inc, 2005.
- [52] Anastasia Rusina, Maxim Durach, and Mark I. Stockman. Theory of spoof plasmons in real metals. *Appl. Phys. A*, 100(2):375–378, 2010.
- [53] Stefan A. Maier. *Plasmonics: Fundamentals and applications*. Springer, New York, NY, 2007.
- [54] James C. Swihart. Field Solution for a Thin-Film Superconducting Strip Transmission Line. *J. Appl. Phys.*, 32:461, 1961.
- [55] P. V. Mason and R. W. Gould. Slow-wave structures utilizing superconducting thin-film transmission lines. *J. Appl. Phys.*, 40(5):2039–2051, 1969.
- [56] John R. Clem. Inductances and attenuation constant for a thin-film superconducting coplanar waveguide resonator. *J. Appl. Phys.*, 113:013910, 2013.
- [57] C. Veyres and V. F. Hanna. Extension of the application of conformal mapping techniques to coplanar lines with finite dimensions. *Int. J. Electron.*, 48(1):47–56, 1980.
- [58] Garg Ramesh, Inder Bahl, and Maurizio Bozzi. *Microstrip Lines and Slotlines*. Artech House, third edition, 2013.
- [59] Ning Hua Zhu, Edwin Yue Bun Pun, and Jia Xu Li. Analytical formulas for calculating the effective dielectric constants of coplanar lines for OIC applications. *Microw. Opt. Technol. Lett.*, 9(4):229–232, 1995.
- [60] Giovanni Ghione and Michele Goano. Revisiting the partial-capacitance approach to the analysis of coplanar transmission lines on multilayered substrates. *IEEE Trans. Microw. Theory Tech.*, 51(9):2007–2014, 2003.
- [61] Giovanni Ghione, Guido Omegna, Marco Pirola, Sergio Bosso, Aldo Perasso, Michèle Goano, Gianluigi Madonna, and Davide Frassati. Microwave modeling and characterization of thick coplanar waveguides on oxide-coated lithium niobate substrates for electrooptical applications. *IEEE Trans. Microw. Theory Tech.*, 47(12):2287–2293, 1999.
- [62] B. Cabrera and M. E. Peskin. Cooper-pair mass. *Phys. Rev. B*, 39(10):6425–6430, 1989.
- [63] Todor M. Mishonov. Technique for measuring the Cooper-pair velocity, density, and mass using Doppler splitting of the plasmon resonance in low-dimensional superconductor microstructures. *Phys. Rev. B*, 50(6):4004, 1994.

- [64] Di Zhu, Michel Bosman, and Joel K W Yang. A circuit model for plasmonic resonators. *Opt. Express*, 22(8):9809–19, 2014.
- [65] A. Yariv. Coupled-mode theory for guided-wave optics. *IEEE J. Quantum Electron.*, 9(9):919, 1973.
- [66] S.S. Bedair. Characteristics of Some Asymmetrical Coupled Transmission Lines. *IEEE Trans. Microw. Theory Tech.*, 32(1):108–110, 1984.
- [67] P.K. Ikalainen and G.L. Matthaei. Wide-Band, Forward-Coupling Microstrip Hybrids with High Directivity. *IEEE Trans. Microw. Theory Tech.*, 35(8):719–725, 1987.
- [68] Robert P. Erickson. Variational theory of the tapered impedance transformer. *J. Appl. Phys.*, 123:074501, 2018.
- [69] L. R. Walker and N. Wax. Non-Uniform Transmission Lines and Reflection Coefficients. *J. Appl. Phys.*, 17(12):1043, 1946.
- [70] R. W. Klopfenstein. A Transmission Line Taper of Improved Design. *Proc. IRE*, 44(1):31–35, 1956.
- [71] Di Zhu, Marco Colangelo, Boris A. Korzh, Qing-Yuan Zhao, Simone Frasca, Andrew E. Dane, Angel E. Velasco, Andrew D. Beyer, Jason P. Allmaras, Edward Ramirez, William J. Strickland, Daniel F. Santavicca, Matthew D. Shaw, and Karl K. Berggren. Superconducting nanowire single-photon detector with integrated impedance-matching taper. *Appl. Phys. Lett.*, 114(4):042601, 2019.
- [72] A J Kerman, E A Dauler, and B S Robinson. Superconducting nanowire photon-counting detectors for optical communications. *Lincoln Lab. J.*, 16(1):217–224, 2006.
- [73] Joseph C. Bardin, Prasana Ravindran, Su-Wei Chang, Charif Mohamed, Raghavan Kumar, Jeffrey A. Stern, Matthew D. Shaw, Damon Russell, Francesco Marsili, Giovanni Resta, and William H. Farr. Cryogenic SiGe integrated circuits for superconducting nanowire single photon detector readout. In Mark A. Itzler and Joe C. Campbell, editors, *Proc. SPIE*, volume 9114, page 911404. International Society for Optics and Photonics, 2014.
- [74] Hamdi Mani and Philip Maukopf. A single-stage cryogenic LNA with low power consumption using a commercial SiGe HBT. In *2014 11th Int. Work. Low Temp. Electron.*, pages 17–20. IEEE, 2014.
- [75] Chao Wan, Zhou Jiang, Lin Kang, and Peiheng Wu. High Input Impedance Cryogenic RF Amplifier for Series Nanowire Detector. *IEEE Trans. Appl. Supercond.*, 27(4):1502605, 2017.

- [76] Clinton Cahall, Daniel J. Gauthier, and Jungsang Kim. Scalable cryogenic readout circuit for a superconducting nanowire single-photon detector system. *Rev. Sci. Instrum.*, 89(6):063117, 2018.
- [77] Adam N McCaughan and Karl K Berggren. A superconducting-nanowire three-terminal electrothermal device. *Nano Lett.*, 14(10):5748–53, 2014.
- [78] Hirotaka Terai, Shigehito Miki, Taro Yamashita, Kazumasa Makise, and Zhen Wang. Demonstration of single-flux-quantum readout operation for superconducting single-photon detectors. *Appl. Phys. Lett.*, 97(11):112510, 2010.
- [79] T Ortlepp, M Hofherr, L Fritzsich, S Engert, K Ilin, D Rall, H Toepfer, H-G Meyer, and M Siegel. Demonstration of digital readout circuit for superconducting nanowire single photon detector. *Opt. Express*, 19(19):18593–601, 2011.
- [80] M. Bell, A. Antipov, B. Karasik, A. Sergeev, V. Mitin, and A. Verevkin. Photon number-resolved detection with sequentially connected nanowires. *IEEE Trans. Appl. Supercond.*, 17(2):289–292, 2007.
- [81] J. Kitaygorsky, S. Dorenbos, E. Reiger, R. Schouten, V. Zwiller, and R. Sobolewski. HEMT-Based Readout Technique for Dark- and Photon-Count Studies in NbN Superconducting Single-Photon Detectors. *IEEE Trans. Appl. Supercond.*, 19(3):346–349, 2009.
- [82] Saeedeh Jahanmirinejad and Andrea Fiore. Proposal for a superconducting photon number resolving detector with large dynamic range. *Opt. Express*, 20:5017, 2012.
- [83] Andrew J. Kerman, Joel K. W. Yang, Richard J. Molnar, Eric A. Dauler, and Karl K. Berggren. Electrothermal feedback in superconducting nanowire single-photon detectors. *Phys. Rev. B*, 79(10):100509, 2009.
- [84] Andrew E. Dane, Adam N. McCaughan, Di Zhu, Qingyuan Zhao, Chung-Soo Kim, Niccolo Calandri, Akshay Agarwal, Francesco Bellei, and Karl K. Berggren. Bias sputtered NbN and superconducting nanowire devices. *Appl. Phys. Lett.*, 111(12):122601, 2017.
- [85] Karl K Berggren, Qing-Yuan Zhao, Nathnael Abebe, Minjie Chen, Prasana Ravindran, Adam McCaughan, and Joseph C Bardin. A superconducting nanowire can be modeled by using SPICE. *Supercond. Sci. Technol.*, 31(5):055010, 2018.
- [86] Qing-Yuan Zhao, Daniel F. Santavicca, Di Zhu, Brian Noble, and Karl K. Berggren. A distributed electrical model for superconducting nanowire single photon detectors. *Appl. Phys. Lett.*, 113:082601, 2018.
- [87] Q. Zhao, L. Zhang, T. Jia, L. Kang, W. Xu, J. Chen, and P. Wu. Intrinsic timing jitter of superconducting nanowire single-photon detectors. *Appl. Phys. B*, 104(3):673–678, 2011.

- [88] F. Najafi, F. Marsili, E. Dauler, R. J. Molnar, and K. K. Berggren. Timing performance of 30-nm-wide superconducting nanowire avalanche photodetectors. *Appl. Phys. Lett.*, 100:152602, 2012.
- [89] Di Zhu, Qing-Yuan Zhao, Hyeonrak Choi, Tsung-Ju Lu, Andrew E. Dane, Dirk Englund, and Karl K. Berggren. A scalable multi-photon coincidence detector based on superconducting nanowires. *Nat. Nanotechnol.*, 13:596–601, 2018.
- [90] E. Waks, K. Inoue, W.D. Oliver, E. Diamanti, and Y. Yamamoto. High-efficiency photon-number detection for quantum information processing. *IEEE J. Sel. Top. Quantum Electron.*, 9(6):1502–1511, 2003.
- [91] E. J. Gansen, M. A. Rowe, M. B. Greene, D. Rosenberg, T. E. Harvey, M. Y. Su, R. H. Hadfield, S. W. Nam, and R. P. Mirin. Photon-number-discriminating detection using a quantum-dot, optically gated, field-effect transistor. *Nat. Photonics*, 1(10):585–588, 2007.
- [92] Leaf A. Jiang, Eric A. Dauler, and Joshua T. Chang. Photon-number-resolving detector with 10 bits of resolution. *Phys. Rev. A*, 75:062325, 2007.
- [93] Pieter Kok, W. J. Munro, Kae Nemoto, T. C. Ralph, Jonathan P. Dowling, and G. J. Milburn. Linear optical quantum computing with photonic qubits. *Rev. Mod. Phys.*, 79(1):135–174, 2007.
- [94] Gilles Brassard, Norbert Lütkenhaus, Tal Mor, and Barry C. Sanders. Limitations on Practical Quantum Cryptography. *Phys. Rev. Lett.*, 8(6):1330, 2000.
- [95] Hoi Kwong Lo, Xiongfeng Ma, and Kai Chen. Decoy state quantum key distribution. *Phys. Rev. Lett.*, 94:230504, 2005.
- [96] Edo Waks, Eleni Diamanti, and Yoshihisa Yamamoto. Generation of photon number states. *New J. Phys.*, 8:4, 2006.
- [97] Mattias Jönsson and Gunnar Björk. Evaluating the performance of photon-number-resolving detectors. *Phys. Rev. A*, 99:043822, 2019.
- [98] M. J. Fitch, B. C. Jacobs, T. B. Pittman, and J. D. Franson. Photon-number resolution using time-multiplexed single-photon detectors. *Phys. Rev. A*, 68:043814, 2003.
- [99] Anthony J. Annunziata, Orlando Quaranta, Daniel F. Santavicca, Alessandro Casaburi, Luigi Frunzio, Mikkel Ejrnaes, Michael J. Rooks, Roberto Cristiano, Sergio Pagano, Aviad Frydman, and Daniel E. Prober. Reset dynamics and latching in niobium superconducting nanowire single-photon detectors. *J. Appl. Phys.*, 108:084507, 2010.
- [100] Kathryn L. Nicolich, Clinton Cahall, Nurul T. Islam, Gregory P. Lafyatis, Jungsang Kim, Aaron J. Miller, and Daniel J. Gauthier. Universal Model for the Turn-on Dynamics of Superconducting Nanowire Single-Photon Detectors. *ArXiv:1811.01067*, 2018.

- [101] Andrew J. Kerman, Eric A. Dauler, William E. Keicher, Joel K. W. Yang, Karl K. Berggren, G. Gol'tsman, and B. Voronov. Kinetic-inductance-limited reset time of superconducting nanowire photon counters. *Appl. Phys. Lett.*, 88:111116, 2006.
- [102] J. Huang, W. J. Zhang, L. X. You, X. Y. Liu, Q. Guo, Y. Wang, L. Zhang, X. Y. Yang, H. Li, Z. Wang, and X. M. Xie. Spiral superconducting nanowire single-photon detector with efficiency over 50 % at 1550nm wavelength. *Supercond. Sci. Technol.*, 30:074004, 2017.
- [103] Ilya Charaev, Alexei Semenov, Konstantin Ilin, and Michael Siegel. Magnetic-field enhancement of performance of superconducting nanowire single-photon detector. *IEEE Trans. Appl. Supercond.*, 29(5):2200605, 2019.
- [104] C. K. Hong, Z. Y. Ou, and L. Mandel. Measurement of Subpicosecond Time Intervals between Two Photons by Interference. *Phys. Rev. Lett.*, 59(18):2044, 1987.
- [105] Giovanni Di Giuseppe, Mete Atatüre, Matthew D. Shaw, Alexander V. Sergienko, Bahaa E.A. Saleh, Malvin C. Teich, Aaron J. Miller, Sae Woo Nam, and John Martinis. Direct observation of photon pairs at a single output port of a beam-splitter interferometer. *Phys. Rev. A*, 68:063817, 2003.
- [106] T. Gerrits, F. Marsili, V. B. Verma, L. K. Shalm, M. Shaw, R. P. Mirin, and S. W. Nam. Spectral correlation measurements at the Hong-Ou-Mandel interference dip. *Phys. Rev. A*, 91:013830, 2015.
- [107] Changchen Chen, Cao Bo, Murphy Yuezhen Niu, Feihu Xu, Zheshen Zhang, Jeffrey H. Shapiro, and Franco N. C. Wong. Efficient generation and characterization of spectrally factorable biphotons. *Opt. Express*, 25(7):7300, 2017.
- [108] Changchen Chen, Jane E. Heyes, Kyung-Han Hong, Murphy Yuezhen Niu, Adriana E. Lita, Thomas Gerrits, Sae Woo Nam, Jeffrey H. Shapiro, and Franco N. C. Wong. Indistinguishable single-mode photons from spectrally engineered biphotons. *Opt. Express*, 27(8):11626, 2019.
- [109] Kristine M. Rosfjord, Joel K. W. Yang, Eric A. Dauler, Andrew J. Kerman, Vikas Anant, Boris M. Voronov, Gregory N. Gol'tsman, and Karl K. Berggren. Nanowire single-photon detector with an integrated optical cavity and anti-reflection coating. *Opt. Express*, 14(2):527, 2006.
- [110] Aaron J. Miller, Adriana E. Lita, Brice Calkins, Igor Vayshenker, Steven M. Gruber, and Sae Woo Nam. Compact cryogenic self-aligning fiber-to-detector coupling with losses below one percent. *Opt. Express*, 19(10):9102, 2011.
- [111] C. Monroe and J. Kim. Scaling the Ion Trap Quantum Processor. *Science*, 339(6124):1164–1169, 2013.

- [112] Lilian Childress, Ronald Walsworth, and Mikhail Lukin. Atom-like crystal defects: From quantum computers to biological sensors. *Phys. Today*, 67(10):38–43, 2014.
- [113] Mihir Pant, Hyeonrak Choi, Saikat Guha, and Dirk Englund. Percolation based architecture for cluster state quantum computation using photon-mediated entanglement between atomic memories. *ArXiv:1704.07292*, 2017.
- [114] Kae Nemoto, Michael Trupke, Simon J. Devitt, Ashley M. Stephens, Burkhard Scharfenberger, Kathrin Buczak, Tobias Nöbauer, Mark S. Everitt, Jörg Schmiedmayer, and William J. Munro. Photonic Architecture for Scalable Quantum Information Processing in Diamond. *Phys. Rev. X*, 4(3):031022, 2014.
- [115] Alberto Peruzzo, Mirko Lobino, Jonathan C. F. Matthews, Nobuyuki Matsuda, Alberto Politi, Konstantinos Poulios, Xiao-Qi Zhou, Yoav Lahini, Nur Ismail, Kerstin Wörhoff, Yaron Bromberg, Yaron Silberberg, Mark G. Thompson, and Jeremy L. O’Brien. Quantum Walks of Correlated Photons. *Science*, 329:1500, 2010.
- [116] Justin B. Spring, Benjamin J. Metcalf, Peter C. Humphreys, W. Steven Kolthammer, Xian-Min Jin, Marco Barbieri, Animesh Datta, Nicholas Thomas-Peter, Nathan K. Langford, Dmytro Kundys, James C. Gates, Brian J. Smith, Peter G. R. Smith, and Ian A. Walmsley. Boson Sampling on a Photonic Chip. *Science*, 339:798, 2013.
- [117] Matthew A Broome, Alessandro Fedrizzi, Saleh Rahimi-Keshari, Justin Dove, Scott Aaronson, Timothy C Ralph, and Andrew G White. Photonic boson sampling in a tunable circuit. *Science*, 339(6121):794–8, 2013.
- [118] Max Tillmann, Borivoje Dakić, René Heilmann, Stefan Nolte, Alexander Szameit, and Philip Walther. Experimental boson sampling. *Nat. Photonics*, 7(7):540–544, 2013.
- [119] Alán Aspuru-Guzik and Philip Walther. Photonic quantum simulators. *Nat. Phys.*, 8(4):285–291, 2012.
- [120] E Knill, G J Milburn, R Laflamme, and G J Milburn. A scheme for efficient quantum computation with linear optics. *Nature*, 409(6816):46–52, 2001.
- [121] Faraz Najafi, Andrew Dane, Francesco Bellei, Qingyuan Zhao, Kristen A. Sunter, Adam N. McCaughan, and Karl K Berggren. Fabrication process yielding saturated nanowire single-photon detectors with 24-ps jitter. *IEEE J. Sel. Top. Quantum Electron.*, 21(2):3800507, 2015.
- [122] J. P. Sprengers, A. Gaggero, D. Sahin, S. Jahanmirinejad, G. Frucci, F. Mattioli, R. Leoni, J. Beetz, M. Lerner, M. Kamp, S. S. Hoffing, R. Sanjines, and A. Fiore. Waveguide superconducting single-photon detectors for integrated quantum photonic circuits. *Appl. Phys. Lett.*, 99:181110, 2011.

- [123] W.H.P. Pernice, C. Schuck, O. Minaeva, M. Li, G.N. Goltsman, a.V. Sergienko, and H.X. Tang. High-speed and high-efficiency travelling wave single-photon detectors embedded in nanophotonic circuits. *Nat. Commun.*, 3:1325, 2012.
- [124] C. Schuck, W. H P Pernice, and H. X. Tang. NbTiN superconducting nanowire detectors for visible and telecom wavelengths single photon counting on Si₃N₄ photonic circuits. *Appl. Phys. Lett.*, 102(5):051101, 2013.
- [125] Faraz Najafi, Jacob Mower, Nicholas C Harris, Francesco Bellei, Andrew Dane, Catherine Lee, Xiaolong Hu, Prashanta Kharel, Francesco Marsili, Solomon Assefa, Karl K Berggren, and Dirk Englund. On-chip detection of non-classical light by scalable integration of single-photon detectors. *Nat. Commun.*, 6:5873, 2015.
- [126] Patrik Rath, Oliver Kahl, Simone Ferrari, Fabian Sproll, Georgia Lewes-Malandrakis, Dietmar Brink, Konstantin Ilin, Michael Siegel, Christoph Nebel, and Wolfram Pernice. Superconducting single photon detectors integrated with diamond nanophotonic circuits. *Light Sci. Appl.*, 4:e338, 2015.
- [127] Matthew Shaw, Francesco Marsili, Andrew Beyer, Jeffrey Stern, Giovanni Resta, Prasana Ravindran, Su Wei Chang, Joseph Bardin, Ferze Patawaran, Varun Verma, Richard P. Mirin, Sae Woo Nam, and William Farr. Arrays of WSi Superconducting Nanowire Single Photon Detectors for Deep Space Optical Communications. In *CLEO 2015*, page JTh2A.68. OSA, 2015.
- [128] Eric A. Dauler, Bryan S. Robinson, Andrew J. Kerman, Vikas Anant, Richard J. Barron, Karl K. Berggren, David O. Caplan, John J. Carney, Scott A. Hamilton, Kristine M. Rosfjord, Mark L. Stevens, and Joel K. W. Yang. 1.25-Gbit/s photon-counting optical communications using a two-element superconducting nanowire single photon detector. *Proc. SPIE*, 6372:637212–637212–8, 2006.
- [129] Shigehito Miki, Hirotaka Terai, Taro Yamashita, Kazumasa Makise, Mikio Fujiwara, Masahide Sasaki, and Zhen Wang. Superconducting single photon detectors integrated with single flux quantum readout circuits in a cryocooler. *Appl. Phys. Lett.*, 99(11):111108, 2011.
- [130] Steffen Doerner, Artem Kuzmin, Stefan Wuensch, Ilya Charaev, and Michael Siegel. Operation of multipixel radio-frequency superconducting nanowire single-photon detector arrays. *IEEE Trans. Appl. Supercond.*, 27(4):2201005, 2017.
- [131] Qingyuan Zhao, Adam McCaughan, Francesco Bellei, Faraz Najafi, Domenico De Fazio, Andrew Dane, Yachin Ivry, and Karl K. Berggren. Superconducting-nanowire single-photon-detector linear array. *Appl. Phys. Lett.*, 103:142602, 2013.

- [132] M Ejrnaes, R Cristiano, O Quaranta, S Pagano, A Gaggero, F Mattioli, R Leoni, B Voronov, and G Gol'tsman. A cascade switching superconducting single photon detector. *Appl. Phys. Lett.*, 91:262509, 2007.
- [133] Di Zhu, Hyeonrak Choi, Tsung-Ju Lu, Qingyuan Zhao, Andrew Dane, Faraz Najafi, Dirk R Englund, and Karl Berggren. Superconducting Nanowire Single-Photon Detector on Aluminum Nitride. In *Conf. Lasers Electro-Optics*, OSA Technical Digest (online), page FTu4C.1, San Jose, California, 2016. Optical Society of America.
- [134] Di Zhu. *Superconducting nanowire single-photon detectors on aluminum nitride photonic integrated circuits*. Master's thesis, Massachusetts Institute of Technology, 2017.
- [135] A. B. Pippard. The surface impedance of superconductors and normal metals at high frequencies III. The relation between impedance and superconducting penetration depth. *Proc. R. Soc. London A*, 191(1026):399, 1947.
- [136] Andrew J. Kerman, Danna Rosenberg, Richard J. Molnar, and Eric A. Dauler. Readout of superconducting nanowire single-photon detectors at high count rates. *J. Appl. Phys.*, 113:144511, 2013.
- [137] Sijing Chen, Lixing You, Weijun Zhang, Xiaoyan Yang, Hao Li, Lu Zhang, Zhen Wang, and Xiaoming Xie. Dark counts of superconducting nanowire single-photon detector under illumination. *Opt. Express*, 23(8):10786, 2015.
- [138] Mariia Sidorova, Alexej Semenov, Heinz-Wilhelm Hübers, Ilya Charaev, Artem Kuzmin, Steffen Doerner, and Michael Siegel. Physical mechanisms of timing jitter in photon detection by current-carrying superconducting nanowires. *Phys. Rev. B*, 96(18):184504, 2017.
- [139] Wolfgang Becker. *Advanced Time-Correlated Single Photon Counting Techniques*. Springer-Verlag Berlin Heidelberg, 2005.
- [140] Francesco Marsili, Faraz Najafi, Charles Herder, and Karl K. Berggren. Electrothermal simulation of superconducting nanowire avalanche photodetectors. *Appl. Phys. Lett.*, 98:093507, 2011.
- [141] Robert M. Heath, Michael G. Tanner, Alessandro Casaburi, Mark G. Webster, Lara San Emeterio Alvarez, Weitao Jiang, Zoe H. Barber, Richard J. Warburton, and Robert H. Hadfield. Nano-optical observation of cascade switching in a parallel superconducting nanowire single photon detector. *Appl. Phys. Lett.*, 104(6):063503, 2014.
- [142] Xiaolong Hu, Charles W. Holzwarth, Daniele Masciarelli, Eric A. Dauler, and Karl K. Berggren. Efficiently coupling light to superconducting nanowire single-photon detectors. *IEEE Trans. Appl. Supercond.*, 19(3):336–340, 2009.

- [143] Mohsen K. Akhlaghi, Ellen Schelew, and Jeff F. Young. Waveguide integrated superconducting single-photon detectors implemented as near-perfect absorbers of coherent radiation. *Nat. Commun.*, 6:8233, 2015.
- [144] Oliver Kahl, Wolfram Pernice, Oliver Kahl, Simone Ferrari, Patrik Rath, Andreas Vetter, and Christoph Nebel. High efficiency, on-chip single-photon detection for diamond nanophotonic circuits. *J. Light. Technol.*, 34(2):249, 2015.
- [145] M G Tanner, L San Emeterio Alvarez, W Jiang, R J Warburton, Z H Barber, and R H Hadfield. A superconducting nanowire single photon detector on lithium niobate. *Nanotechnology*, 23(50):505201, 2012.
- [146] Jan Philipp Höpker, Moritz Bartnick, Evan Meyer-Scott, Frederik Thiele, Torsten Meier, Tim Bartley, Stephan Krapick, Nicola M. Montaut, Matteo Santandrea, Harold Herrmann, Sebastian Lengeling, Raimund Ricken, Viktor Quiring, Adriana E. Lita, Varun B. Verma, Thomas Gerrits, Sae Woo Nam, and Christine Silberhorn. Towards integrated superconducting detectors on lithium niobate waveguides. *Proc. SPIE*, 10358:1035809, 2017.
- [147] E. Smirnov, A. Golikov, P. Zolotov, V. Kovalyuk, M. Lobino, B. Voronov, A. Korneev, and G. Goltsman. Superconducting nanowire single-photon detector on lithium niobate. *J. Phys. Conf. Ser.*, 1124:051025, 2018.
- [148] Andrea Crespi, Roberto Osellame, Roberta Ramponi, Vittorio Giovannetti, Rosario Fazio, Linda Sansoni, Francesco De Nicola, Fabio Sciarrino, and Paolo Mataloni. Anderson localization of entangled photons in an integrated quantum walk. *Nat. Photonics*, 7(4):322–328, 2013.
- [149] Nicholas C. Harris, Darius Bunandar, Mihir Pant, Greg R. Steinbrecher, Jacob Mower, Mihika Prabhu, Tom Baehr-Jones, Michael Hochberg, and Dirk Englund. Large-scale quantum photonic circuits in silicon. *Nanophotonics*, 5(3):456–468, 2016.
- [150] Xiaogang Qiang, Xiaoqi Zhou, Jianwei Wang, Callum M. Wilkes, Thomas Loke, Sean O’Gara, Laurent Kling, Graham D. Marshall, Raffaele Santagati, Timothy C. Ralph, Jingbo B. Wang, Jeremy L. O’Brien, Mark G. Thompson, and Jonathan C. F. Matthews. Large-scale silicon quantum photonics implementing arbitrary two-qubit processing. *Nat. Photonics*, 12(9):534–539, 2018.
- [151] Oliver Kahl, Simone Ferrari, Vadim Kovalyuk, Andreas Vetter, Georgia Lewes-Malandrakis, Christoph Nebel, Alexander Korneev, Gregory Goltsman, and Wolfram Pernice. Spectrally multiplexed single-photon detection with hybrid superconducting nanophotonic circuits. *Optica*, 4(5):557, 2017.
- [152] Yaron Bromberg, Yoav Lahini, Roberto Morandotti, and Yaron Silberberg. Quantum and classical correlations in waveguide lattices. *Phys. Rev. Lett.*, 102:253904, 2009.

- [153] Andrew E. Dane, Adam N. McCaughan, Di Zhu, Qingyuan Zhao, Chung-Soo Kim, Niccolo Calandri, Akshay Agarwal, Francesco Bellei, and Karl K. Berggren. Bias sputtered NbN and superconducting nanowire devices. *Appl. Phys. Lett.*, 111:122601, 2017.
- [154] Joel K. W. Yang and Karl K. Berggren. Using high-contrast salty development of hydrogen silsesquioxane for sub-10-nm half-pitch lithography. *J. Vac. Sci. Technol. B Microelectron. Nanom. Struct.*, 25(6):2025, 2007.
- [155] C. Bockstiegel, J. Gao, M. R. Vissers, M. Sandberg, S. Chaudhuri, A. Sanders, L. R. Vale, K. D. Irwin, and D. P. Pappas. Development of a broadband NbTiN traveling wave parametric amplifier for MKID readout. *J. Low Temp. Phys.*, 176(3-4):476–482, 2014.
- [156] Risheng Cheng, Chang-Ling Zou, Xiang Guo, Sihao Wang, Xu Han, and Hong X. Tang. Broadband on-chip single-photon spectrometer. *ArXiv:1908.00824*, 2019.